1

Studies of the development of rare-earth silicates based on new solid state electrolytes and their application to concentration cell type gas sensors

（希土類－ケイ酸塩からなる新しい固体電解質の開発

と濃淡電池型ガスセンサへの応用に関する研究）

1997年3月

Susumu Nakayama

中　山　享

Contents

Chapter 1
General introduction

1-1. Outline and the present situation, solid electrolytes

The conduction of metals and semiconductors is due to the flow of electrons or holes, whereas the conduction of liquids such as a salt water and dilute sulfuric acid is due to the migration of ions. The existence of solid materials which conduct electricity by the migration of ions is also known. Such a solid ionic conductor is called a solid electrolyte. In general, solids exhibit low ionic conductivity. The ionic conductivities of solid electrolytes lie in the range of 10^{-1} to $10^{-4} S\cdot cm^{-1}$, which are close to those of salt water and dilute sulfuric acid. Although most ionic crystalline materials show relatively high ionic conductivities at their melting points, these materials are not generally classified as solid electrolytes. Materials which are termed the solid electrolytes are rarely found in nature. Most of these materials have been synthesized in the laboratory. The fact that ions move in solids has been known for a long time, the study of "solid state ionics" is however relatively recent, and early reports appeared in the first half of 1960.

A solid electrolyte has generally one conducting ion specie. To date, approximately fifteen conducting ion species are known. These are the mono- or divalent ions. Both cations and anions can play a role as a carrier. Examples of the former (cations) are silver(II), copper(II), alkali metal(I), and hydrogen (proton) ions, and those of the latter (anions) are oxide and fluoride ions.

1-1-1. Silver and copper ionic conductor

The representative silver ionic conductor is α-AgI. It shows a high ionic conductivity ($2\times10^{0} S\cdot cm^{-1}$ at 200℃) above 146℃ because it has an average structure above this temperature [1]. It is generally known that such a high temperature average structure is also realized near room temperature by partially substituting Ag^+ or I^- of AgI by other cations or anions. Based on this strategy, materials which show high conductivity at a relatively low temperature have been developed by a number of groups. $RbAg_4I_5$ ($3x10^{-3}S \cdot cm^{-1}$ at R.T.) is an example of a cation-substituted material and Ag_3SBr ($2x10^{-3}S \cdot cm^{-1}$ at R.T.) is an example of an anion-subtituted material [2,3]. Moreover, substitutions of both cation and anion at the same time is possible, e.g., $RbAg_4I_4CN$ ($1.8x10^{-3}S \cdot cm^{-1}$ at 25℃) [4,5]. It has also been reported that rapid quenching after the oxo ion containing materials are melted lead to the formation of vitreous structure resulting in the high conductivities, e.g., $3AgI \cdot Ag_2MoO_4$ ($2.1x10^{-2}S \cdot cm^{-1}$ at R.T.) [6]. Silver β-alumina ($AgAl_{11}O_{17}$, $6.7x10^{-3}S \cdot cm^{-1}$ at 25℃) and silver chalcogenide based $(Ag_2Se)_{0.925}(AgPO_4)_{0.075}$ ($1.3x10^{-1}S \cdot cm^{-1}$ at 25℃) are peculiar silver ionic conductors which do not contain AgI [7].

Most of the copper ionic conductors consist of copper halide and ammonium ions, which have limitations such as low conductivity and heat-resistance. Ionic conductors composed of only inorganic components, $Rb_4Cu_{16}Cl_{13}I_7$ and $RbCu_4Cl_3I_2$, are also known [8]. Much attention is being paid to the development of these types of ionic conductors because of their high conductivities, e.g., $Rb_4Cu_{13}I_7$ ($3.4x10^{-1}S \cdot cm^{-1}$ at 25℃).

1-1-2. Alkali metal ionic conductor

Typical carriers of alkali metal ionic conductors are lithium ion (Li^+), sodium ion (Na^+) and potassium ion (K^+).

- Lithium ionic conductor -

Because lithium is a light element, the lithium ionic conductor is useful as a solid electrolyte of the high energy density cell. For example, $LiI\text{-}Al_2O_3$ which has a conductivity of about $10^{-5}S \cdot cm^{-1}$ at R.T. has been utilized as the solid electrolyte of the small special cell [9]. The most interesting material is Li_3N which has a layer structure [10]. In the Li_3N, one N^{3-} is surrounded by six lateral Li^+ ions, 1 to 2% of which are missing. Because of these lattice defects, Li^+ ions can move easily in the lateral direction [11]. The conductivity in the lateral direction is about $10^{-3}S \cdot cm^{-1}$ at room temperature, which is one of the highest values reported thus far for lithium ionic conductors. However, there are some problems : (1) Li_3N is easily hydrolyzed by moisture, and then ammonia generates, and (2) the conductivity of polycrystalline Li_3N is low. The conductivities of P_2S_5-Li_2S-LiI glass, B_2S_3-Li_2S-LiI glass and Li_2XCl_4 (X=Mg, Mn or Fe) are comparable to that of Li_3N, but these are also unstable to moisture [12-14]. Many studies on lithium ionic conductors of the double oxide and oxo salt system have also been undertaken. As these types, LISICON (Lithium Super Ionic Conductor, $Li_{14}Zn(GeO_4)_4$) is well known. This has a three dimensional reticulate structure similar to that of NASICON (Sodium Super Ionic Conductor, $Na_3Zr_2Si_2PO_{12}$). The conductivity of LISICON is $1.2x10^{-1}S \cdot cm^{-1}$ at 300℃ but low at room temperature (about $10^{-6}S \cdot cm^{-1}$) [15]. The conductivity at 25 ℃ for $(Li_3PO_4)_{0.5}(Li_4SiO_4)_{0.5}$ is also low ($4x10^{-6}S \cdot cm^{-1}$) [16]. Recently, $Li_{1.3}M_{0.3}Ti_{1.7}(PO_4)_3$ (M=Al, Sc, Y or La) and $LiTi_2(PO_4)_3$-Li_3PO_4 which show conductivities of more than $10^{-4}S \cdot cm^{-1}$ have been developed [17,18]. $RE_{0.5}Li_{0.5}TiO_3$ (RE=La, Pr, Nd or Sm) having the perovskite type structure has also been examined [19]. (The conductivity of $La_{0.5}Li_{0.5}TiO_3$ is $1x10^{-3}S \cdot cm^{-1}$ at 30℃.)

- Sodium ionic conductor -

β-alumina is well known as a sodium ionic conductor. The materials of this group are expressed by the following chemical equation :

$$A_2O \cdot nB_2O_3 \qquad \begin{array}{l} A = Li, Na, K, Rb, Ag, Tl, --- \\ B = Al, Ga, Fe, --- \\ n = 5\text{-}11 \end{array}$$

Sodium β-alumina has a layer structure, in which sodium ions is located in the interlayer between spinel blocks formed by the Al-O bonds. It shows a high conductivity ($1.4x10^{-2}S \cdot cm^{-1}$ at 25℃ (single crystal)) because sodium ions can move along the layer [20,21]. Another group, β''-alumina, a representatives of which is $Na_2O \cdot 5.33Al_2O_3$ also exists. The conduction mechanism of β''-alumina is the same as that of β-alumina. Furthermore, the conductivity of β''-alumina is higher than that of β-alumina but its stability is low [22]. Incidentally, sodium ions in β-alumina can be substituted by other cations and some cation-substituted

β-alumina's exhibit high conductivities. Recently, NASICON has also attracted attention[23]. NASICON as well as LISICON is a type of ion exchanger. The corners of PO_4 tetrahedra and SiO_4 tetrahedra are shared with those of ZrO_6 octahedra to give the three dimensional reticulate structure. Sodium ions are located in the relatively large spaces (the so-called conduction channel) formed in these reticulate structures and hence can move freely to give high conductivity compared to that of β-alumina. The principal advantages of NASICON can be summarized as follows : (1) NASICON can be sintered at about 1200℃, whereas the sintering temperature of β-alumina is greater than 1600℃, (2) NASICON is stable in moist air and in water, and (3) NASICON based on the Zr-poor composition $Na_{2.94}Zr_{1.49}P_{0.80}Si_{2.20}O_{10.85}$ and prepared from alkoxide derived gels is stable even in molten sodium [24]. It is interesting to note that the conductivity of $Na_{1+X}Hf_2Si_XP_{3-X}O_{12}$ (X=1.4-2.8) prepared by the replacement Zr of NASICON by Hf is 1.5 times that of NASICON [25]. Also, $Na_5RESi_4O_{12}$ (RE=Sm, Gd, Tb, Dy, Y, Ho, Er, Tm, Yb, Lu or Sc) with a similar crystal structure to that of NASICON has been developed and its conductivity (10^{-2}-$10^{-1}S\cdot cm^{-1}$ at 300℃) is close to that of NASICON [26].

- Potassium ionic conductor -

Potassium ionic conductors which exhibit conductivities as high as those of lithium or sodium ionic conductors have not been developed yet. Although $K_XMg_{X/2}Ti_{8-X/2}O_{16}$ with a hollandite type structure (one dimensional tunnel structure) have been known for a long time, its conductivity is not so high (less than $10^{-2}S\cdot cm^{-1}$ at 300℃) [27]. $K_2O\cdot 6Fe_2O_3$ and $K_2O\cdot 5.2Fe_2O_3\cdot 0.8ZnO$ have a two dimensional structure similar to that of β-alumina and show relatively high conductivities [28,29]. However, $K_2O\cdot 6Fe_2O_3$ is a mixed conductor and the potassium ionic conductivity is only 1.5% of the total conductivity, while the electronic conductivity of $K_2O\cdot 5.2Fe_2O_3\cdot 0.8ZnO$ is neglible, although the conductivity is $1.8x10^{-2}S\cdot cm^{-1}$ at 300℃. $K_{1.9}Mg_{0.95}Si_{1.05}O_4$ ($3.6x10^{-2}S\cdot cm^{-1}$ at 300℃) having the three dimensional structure, and $K_{0.72}In_{0.72}Hf_{0.28}O_2$ ($1.0x10^{-2}S\cdot cm^{-1}$ at 300℃) and $K_{0.72}In_{0.72}Sn_{0.28}O_2$ ($2.2x10^{-2}S\cdot cm^{-1}$ at 300℃) with a layer structure are reported to show high conductivities [30,31]. Potassium β-alumina is also a potassium ionic conductor but its conductivity ($6.5 \times 10^{-5} S \cdot cm^{-1}$ at 25℃ (single crystal)) is significantly lower than that of sodium β-alumina and the activation energy for conduction is higher [32]. The difference in conductivity between potassium β-alumina and sodium β-alumina is thought to be due to the difference in ionic size : The interlayer thickness between the spinel blocks of β-alumina is more suited to sodium or silver ions (-0.1nm diameter) than to the large potassium ion.

1-1-3. Proton conductor

A proton differs from other ions in the sense of the absence of electron cloud. Although its mass is much greater than that of an electron, its size is very small. In addition, the proton can interact electrostatically and strongly with anions because of its high polarizability, and hence cannot move in the same way as other cations. Therefore, it is generally accepted that proton conduction in a solid occurs through hydrogen bonding. The conductivities of $H_3W_{12}PO_4 \cdot 29H_2O$ and $H_3Mo_{12}PO_4 \cdot 29H_2O$ are remarkably high ($2 \times 10^{-1} S \cdot cm^{-1}$ at 25℃ (single crystal)) when compared with those of conventional proton conductors [33]. Other examples are β-alumina partially substituted with H_3O^+ or NH^{4+} and $HUO_2PO_4 \cdot 4H_2O$, the conductivities of which lie in the range of 10^{-3} to $10^{-4} S \cdot cm^{-1}$ at room temprtature [34,35]. Materials with high proton conductivities are not well documented at high temperatures. Therefore, most proton conductors have been utilized in the temperature range from room temperature to 200℃. $SrCe_{0.95}Yb_{0.05}O_{3-X}$ has been reported to show proton conduction in spite of the absence protons [36]. The conduction of this material is, of course, based on hole conduction. However, when protons are introduced, they move instead of holes to demonstrate proton conduction. The high conductivity at 1000℃ ($1 \times 10^{-2} S \cdot cm^{-1}$) of $SrCe_{0.95}Yb_{0.05}O_{3-X}$ lends itself to applications in fuel cell technology, membranes for hydrogen separation and a hydrogen sensor in molten metal [37-39].

1-1-4. Halide ionic conductor

In the lead halide (PbX_2, X=F,Cl,Br) series, conductivity increases with decreasing ionic radius of the halide ion. PbF_2 is the most interesting halide ionic conductor because of its high conductivity. Therefore, much attention has been paid to the chemical sensor application using fluoride ionic conductors such as the fluorite type of CaF_2 and BaF_2, and the tysonite of LaF_3 and CeF_3 [40,41]. Moreover, studies have been also undertaken on the solid solution possessing vacancies or excess fluoride ions located among the crystal lattices by doping the different fluorides. PbF_2 dissolved KF, BiF_3 and AlF_3 has a conductivities in the range from 10^{-1} to $10^{-2}S \cdot cm^{-1}$ at 300℃ [42,43]. The conductivity of $PbSnF_4$ prepared by the addition of 50mol% SnF_2 to PbF_2 is about $10^{-1}S \cdot cm^{-1}$ at 100℃. This value is very high, so far as anionic conductors are concerned [44]. These materials have the fluorite type structure and the fluoride ionic conduction is considered to occur through vacancies, ions among lattice and clusters.

Also chloride and bromide ions action as a carrier as described above. Although the conductivity of $PbCl_2$ or $PbBr_2$ (10^{-3}-$10^{-4}S \cdot cm^{-1}$ at 300℃) is lower than that of the fluoride ionic conductor, $PbCl_2$ has been examined as the solid electrolyte for chloric cells and sensors [45].

1-1-5. Oxide ionic conductor

The solid solutions obtained by combining di- and trivalent metal oxides such as CaO, MgO and Y_2O_3 to ZrO_2, CeO_2, ThO_2 and HfO_2 are well known to show relatively high conductivities. These solid solutions have a fluorite type crystal structure, and it is possible to dissolve the high concentration of CaO (5-10mol%). Thus, the oxide ionic conduction occurs through the resulting O^{2-} vacancies. Solid solutions prepared by the dissolution of CaO, MgO and Y_2O_3 in ZrO_2 have been known from the beginning of this century and are called "stabilized zirconia". (The conductivity of $(ZrO_2)_{0.9}(Y_2O_3)_{0.1}$ is $2.0x10^{-2}S \cdot cm^{1-}$ at 800℃.) The mechanism of O^{2-} ionic conduction was proposed by Wagner in 1948 [46]. Various stabilizers have been examined in the effort to develop an oxide ionic conductor with high conductivity. It has been found that the highest conductivity is obtained for a solid solution stabilized by a rare earth oxide [47]. (The conductivity of $(ZrO_2)_{0.9}(Sc_2O_3)_{0.1}$ is $1.0x10^{-2}S \cdot cm^{-1}$ at 800℃.) Y_2O_3 stabilized zirconia and the MgO stabilized zirconia have already been used practically as oxygen sensors in automobile exhausts and in molten metals, respectively [48,49]. The conductivity of ceria solid solution is higher than that of stabilized zirconia but cerias is not stable in a reducing atmosphere, in that it exhibits properties of n-type semiconductor at low oxygen partial pressure [50]. (The conductivity of $(CeO_2)_{0.78}(GdO_{1.5})_{0.23}$ is $1.1\times10^{-1}S\cdot cm^{-1}$ at 800℃.) Thoria solid solution shows p-type semiconductivity at high oxygen partial pressure at room temperature [51]. The highest oxide ionic conductivity is obtained for Bi_2O_3 based electrolyte. Although Bi_2O_3 exhibits p-type semiconductor properties below 730℃, it shows high ionic conductivity above 730℃ due to the phase-transition from the cubic fluorite type structure of δ-type to the monoclinic structure of α-type. In order to obtain the high oxide ionic conductivity phase, δ-type phase, at lower temperature, Y_2O_3 has been dissolved in Bi_2O_3 [52]. However, Bi_2O_3 system is not stable in a reducing atmosphere, whereas it is stable in an oxidizing atmosphere. The conductivities of $(La_2O_3)_{0.95}(SrO)_{0.05}$ and $Zr_2RE_2O_7$ (RE=Nd or Gd) are close to that of Y_2O_3 stabilized zirconia [53.54]. It is known that the perovskite type oxides are good ionic conductors because of the oxide ion vacancies, though they show, more or less, the properties of a hole conductor. Recently, $La_{0.9}Sr_{0.1}Ga_{0.8}Mg_{0.2}O_3$ having a conductivity which is one order of magnitude greater than that of Y_2O_3 stabilized zirconia at an oxygen partial pressure of 1 to 10^{-20}atm was reported. electron or hole conduction has been almost neglected [55]. $BaTh_{0.9}Gd_{0.1}O_{2.92}$ which show conductivity of $8.7\times10^{-2}S\cdot cm^{-1}$ at 550℃ has also been developed [56].

1-2. Summary and the present status of CO_2 gas sensors based on solid electrolytes

Recently, materials (so-called gas sensor) which can quickly and simply determine the concentration of various gases have been extensively studied and developed. Some of these materials have already been utilized, for example, for gas leaks, and for humidity sensing in a microwave oven. Little attention has been paid to the CO_2 concentration in an atmosphere, whereas much attention has been paid to combustible gases, ill-smelling gases or poisonous gases. The concentration of CO_2 gas in the atmosphere is increasing because of the recent human activity, especially the consumption of extraordinarily large amounts of fossil fuel. Furthermore, indoor CO_2 gas is also increased by respiration and the use of oil-heater. Such increases in CO_2 gas concentration contributes to a greenhouse effect. Therefore, the appearance of cheap sensors which can simply detect CO_2 concentration and accurately is desired earnestly. The detection and the control of CO_2 concentrations is becoming important in various fields such as industrial processes, home electronics products, agricultural hothousees and biology.

Although the infrared absorption apparatus used for CO_2 analysis is most popular, there are some problems including CO_2 must be separated from other infrared-ray absorbing compounds and that the apparatus is expensive and of a large size. The smaller apparatus of the electrochemical or heat conduction methods have the disadvantage of lack of precision. Stability and gas selectivity are also often unsatisfactory. Moreover, an electrolyte solution is necessary for the electrochemical methods.

To overcome these disadvantages, the development of the electrochemical CO_2 gas sensors using solid electrolytes as a choice of gas-permeable films has been undertaken. Concentration cell type sensors using stabilized zirconia are well known and have been applied to the control of air/fuel ratio in automobile's engines and for the determination of O_2 concentration in molten metals. The principle of the concentration cell type CO_2 gas sensor, in which K_2CO_3 is used as a solid electrolyte, has been proposed by Gautheir et al. in 1977 [57] and various studies have been carried out since their reports. The principle of an electrochemical CO_2 gas sensor is as follows : the electromotive force is generated from the difference in gas concentration between two electrodes separated by the solid electrolyte. The gas concentration is related to the electromotive force by the Nernst equation. In this type of sensor, only one kind of ion moves through the solid electrolyte, resulting in high gas selectivity and high sensitivity. Additionally, it is possible to improve the stability in air and that the production cost is lowered by using the oxide ceramic as a matrix material. However, there are many problems : (1) high operation temperature, (2) complicated device structure, requiring a reference atmosphere, (3) long response time, (4) the influence of the water vapor, and (5) the lack of long-term stability. Therefore, a number of improvements in the detection of CO_2 gas have been attempted by selecting different solid electrolytes and solid electrode materials. Over the past ten years, electrochemical CO_2 gas sensors have been extensively studied and developed. When a solid electrolyte other than metal carbonates is used as a sensor material, a solid electrode material that can convert the changing CO_2 concentration in the detected gas into a change of activity of mobile ion in the solid electrolyte is required. However, for these CO_2 gas sensors, the change in the electromotive force is small even if the change of CO_2 concentration is large, and the response and the recovery time become remarkably long as the partial pressure of water vapor in the detected gas increases. Moreover, the electromotive force is also affected by the O_2 concentration in the detected gas. According to studies using various Na^+ ionic conductors and Na salts as a solid electrolyte and a solid electrode, respectively, the reduction of the electromotive force in humid atmosphere is caused by the formation of NaO_X on the detection electrode [58-60]. It has been reported that the response time is relatively fast regardless of the existence of water vapor and that a stable electromotive force independent of the partial pressure of water vapor is observed, when the $BaCO_3$-Na_2CO_3 system is used as the solid electrode [61]. Similar results are obtained using other kinds of Na^+ ionic conductors or by using $CaCO_3$-Na_2CO_3 and $SrCO_3$-Na_2CO_3 systems as the solid electrode. CO_2 gas sensors have also been investigated using ionic conductors other than Na^+ ionic conductor, for example, $LiTi_2(PO_4)_3$+$0.2Li_3PO_4$ as a Li^+ ionic conductor, $MgZr_4(PO_4)_6$ as a Mg^+ ionic conductor or LaF_3 as a F^- ionic conductor, the solid electrode material is Li_2CO_3 for all of these sensors [62-65]. In addition, improvements in counter electrodes have also been undertaken. Namely, one-end seal type devices have been reported, where $(ZrO_2)_{0.92}(Y_2O_3)_{0.08}$ or $(Bi_2O_3)_{0.75}(Y_2O_3)_{0.25}$ is prepared on the counter electrode of NASICON or $LiTi_2(PO_4)_3$+$0.2Li_3PO_4$, respectively. These devices have an electromotive force unaffected by O_2 concentration and show excellent CO_2 selectivity.

High CO_2 gas selectivity is also observed using layer-type devices, where $(ZrO_2)_{0.92}(Y_2O_3)_{0.08}$ is stacked on the counter electrode of NASICON+40wt%$NaAlSi_2O_6$ or $NaAlSi_2O_6$ by heat-treatment. Such devices have high strength and dense microstructure which are properties of stabilized zirconia [66-69].

However, reliable and economical CO_2 gas sensors with high sensitivity, good selectivity, rapid response time, good long-term stability and high accuracy are still not developed and are not put to practical use at the present stage.

1-3. Purpose and outline of this study

Recently, there has been considerable interest in dense ionic conductors with high conductivity which might be developed into solid state batteries and chemical sensors. In particular, many studies have been undertaken on materials containing oxo groups such as SiO_4, PO_4, GeO_4 and ZrO_2 because these materials make it possible to prepare alkali-metal ionic conductors with high conductivity as mentioned in section 1-1. It has also been reported that many ionic conductors containing rare-earths (RE) having large ionic radii show high conductivity. In this study, a series of new rare-earth silicates (solid electrolyte) where three-dimensional network structure is built up by the interconnected REO_6 octahedra and SiO_4 tetrahedra, were prepared and their properties investigated. Moreover, the application of these solid electrolytes to concentration cell type CO_2 gas sensors was examined. This thesis is made up by the following six chapters.

This chapter, chapter 1, has described the outline and the present situation of solid electrolytes and CO_2 gas sensors based on the properties of these solid electrolytes. Chapter 2 deals with crystal structures, microstructures and electrical properties of the alkali-metal rare-earth silicates (represented by M_2O-RE_2O_3-$2SiO_2$) prepared by sintering of $M_2CO_3 \cdot RE_2O_3 \cdot 2SiO_2$ (M=Li,Na,K,Rb,Cs RE=La,Nd,Sm,Gd,Dy,Y,Ho,Er,Yb) mixture. In chapter 3, crystal structures, microstructures and electrical properties of K_2O-Sm_2O_3-$nSiO_2$ are investigated with the aim of improving its water-resistance of K_2O-Sm_2O_3-$2SiO_2$ which shows the highest conductivity and the lowest activation energy, where n varies from 1 to 14. Chapter 4 describes crystal structures, microstructures and electrical properties of the rare-earth silicates, $RE_{10}Si_6O_{27}$ (RE=La,Nd,Sm,Gd,Dy,Y,Ho,Er,Yb). In chapter 5, concentration cell type CO_2 gas sensors, fabricated using K_2O-Sm_2O_3-$6SiO_2$, Li_2O-RE_2O_3-$2SiO_2$ (RE=La,Nd,Sm) and Li_2O-Sm_2O_3-$2SiO_2$+$(ZrO_2)_{0.92}(Yb_2O_3)_{0.08}$ (layer type ionic conductor) as solid electrolytes, and their response characteristics are examined. Chapter 6 summarizes conclusions drawn from this study.

List of publications for the present work

1. Electrical conductivity of $Na_3Zr_2Si_2PO_{12}$-doped sodium aluminosilicate glass
   Y.Sadaoka, Y.Sakai, M.Matsuguchi and S.Nakayama,
   J. Mater. Sci., 24, 1299-1304(1989).
2. Microstructures and Electrical Properties for $LiXSiO_4$
   (X=Al,La,Nd,Sm,Gd,Dy,Y,Ho,Er,Yb) 《Japanese》
   S.Nakayama and M.Sakamoto,
   J.Ceram.Soc.Japan, 100, 867-871(1992).
3. Humidity Sensor Using Porous Ceramics $xLi_2O \cdot Al_2O_3 \cdot 2SiO_2$ 《Japanese》
   S.Nakayama, H.Kuroshima, Y.Sadaoka and Y.Sakai,
   J.Ceram.Soc.Japan, 100, 968-971(1992).
4. Ionic Conductivity of Ceramics prepared by Sintering of
   M_2O-Ln_2O_3-$2SiO_2$ Mixtures (M=Li,Na,K,Rb,Cs Ln=La,Nd,
   Sm,Gd,Dy,Y,Ho,Er,Yb)
   S.Nakayama and Y.Sadaoka,
   J.Mater.Chem., 3, 1251-1257(1993).
5. CO_2 Gas Sensor Using Lithium Ion Conductors 《Japanese》
   S.Kuwata, S.Sudoh, A.Oonishi, M.Kodama, Y.Takahashi, H.Ugawa,
   S.Nakayama and Y.Sadaoka,
   Memories of Niihama National College of Technology, 30, 54-58(1994).
6. Preparation of an $Na_2Zr_2Si_2PO_{12}$-Sodium Aluminosilicate Composite
   and its Application as a Solid-state Electrochemical CO_2 Gas Sensor
   S.Nakayama and Y.Sadaoka,
   J.Mater.Chem., 4, 663-668(1994).
7. Ionic Conductivity of Potassium Samarium Silicates and
   Its Application as an Electrochemical CO_2 Gas Sensor
   S.Nakayama, M.Wake, Y.Sadaoka and Y.Sakai,
   Denki Kagaku, 63, 319-322(1995).

8. Preparation of Vitreous Sodium Aluminosilicate and Its Application as a Solid-State Electrochemical CO_2 Gas Sensor
H.Supriyatno, A.Dubbe, M.Matsuguchi, Y.Sadaoka, Y.Sakai and S.Nakayama,
Denki Kagaku, 63, 325-328(1995).

9. Ionic Conductivity of $Ln_{10}(SiO_4)_6O_3$ (Ln=La,Nd,Sm,Gd and Dy)
S.Nakayama, H.Aono and Y.Sadaoka,
Chem.Lett., **1995**, 431-442.

10. Prepared of K_2O-Sm_2O_3-$nSiO_2$-based solid-state electrolyte and its application to CO_2 electrochemical Sensor
Y.Sadaoka, S.Nakayama, Y.Sakai and M.Wake,
Sensor and Actuators B, **24-25**, 282-286(1995).

11. Morphology and Ionic Conductivity of Potassium-Samarium-Silicates, K_2O-Sm_2O_3-$nSiO_2$ (n=1～14)
S.Nakayama and Y.Sadaoka,
Electrochimica Acta, 40, 2541-2546(1995).

12. Ionic Conductivity of Rare Earth-Silicates, $Lnx(SiO_4)_6O_Y$ (Ln=La,Nd,Sm,Gd,Dy,Y,Ho,Er and Yb)
S.Nakayama, T.Kageyama, H.Aono and Y.Sadaoka,
J.Mater.Chem. 5, 1801-1805(1995).

13. Solid Electrolyte Oxygen Sensor Using $Nd_{10}Si_6O_{27}$ 《Japanese》
S.Kuwata, S.Komoda, A.Miyazaki, M.Kodama, S.Nakayama and Y.Sadaoka,
Memories of Niihama National College of Technology, 32, 108-112(1996).

14. Solid State CO_2 Gas Sensor Using Alkali Metalic Ion Conductors 《Japanese》
S.Kuwata, Y.Shiozaki, M.Mizuseki, M.Yamasaki, A.Miyazaki,
S.Nakayama and Y.Sadaoka,
Memories of Niihama National College of Technology, 33, 111-116(1997).

15. CO_2 gas sensor using a potassium ionic conductor K_2O-Sm_2O_3-$6SiO_2$
S.Nakayama, S.Kuwata, M.Sato, M.Sakamoto and Y.Sadaoka,
J.Ceram.Soc.Japan, 105, 255-257(1997).

List of other publications

1. Fixation of Zr and Hf(IV) Complex Anion with Co(III) Complex Cation (1)

   — $[Co(NH_3)_6]_4[(Zr,Hf)(C_2O_4)_4]_3 \cdot 12H_2O$ —

   T.Ishimori, M.Sakamoto and S.Nakayama,

   Memoirs of the Faculty of Engineering, Ehime University, 10(3), 467-472(1984).

2. Fixation of Zr and Hf(IV) Complex Anion with Co(III) Complex Cation (2)

   — Gravimetric Determination of Zr/Hf Ratio Using

   $[Co(NH_3)_6]_4[(Zr,Hf)(C_2O_4)_4]_3 \cdot 12H_2O$ —

   T.Ishimori, M.Sakamoto and S.Nakayama,

   Memoirs of the Faculty of Engineering, Ehime University, 10(4), 463-468(1985).

3. Fixation of Zr and Hf(IV) Complex Anion with Co(III) Complex Cation (3)

   — $[Co(NH_3)_{6-n}(H_2O)_n]_4[(Zr,Hf)(C_2O_4)_4]_3 \cdot mH_2O$ —

   T.Ishimori, M.Sakamoto and S.Nakayama,

   Memoirs of the Faculty of Engineering, Ehime University, 11(1), 361-367(1986).

4. Fixation of Zr and Hf(IV) Complex Anion with Co(III) Complex Cation (4)

   — $[CoX(NH_3)_5]_2[(Zr,Hf)(C_2O_4)_4] \cdot mH_2O$ ($X=NO_3,NO_2$ and NCS) —

   T.Ishimori, M.Sakamoto and S.Nakayama,

   Memoirs of the Faculty of Engineering, Ehime University, 11(1), 369-375(1986).

5. Humidity sensor using KH_2PO_4-doped porous ferroelectrics

   Y.Sadaoka, Y.Sakai, H.Aono, S.Nakayama and H.Kuroshima,

   J. Mater. Sci. Lett., 5, 923-924(1986).

6. Humidity sensors using KH_2PO_4-doped porous $(Pb,La)(Zr,Ti)O_3$

   Y.Sadaoka, Y.Sakai, M.Matsuguchi, H.Aono, S.Nakayama and H.Kuroshima,

   J. Mater. Sci., 22, 3685-3692(1987).

7. Ceramics Humidity Sensor / SPK-H series

   H.Kuroshima and S.Nakayama,

   Ceramics Humidity Sensor / SPK-H series

   Shinagawa Technical Report, 33 ,205-208(1990).

8. Humidity and temperature dependence of the electrical properties of porous ceramic PLZT 《Japanese》
S.Nakayama, H.Kuroshima and Y.Sadaoka,
New Ceramics, **1991(5)**, 73-77.

9. Preparation of Perovskite-Type Oxide, $LaCrO_3$, by Thermal Decomposition of La $[Cr(CH_2(COO)_2)_3]\cdot 6H_2O$ 《Japanese》
S.Nakayama and M.Sakamoto,
J. Ceram. Soc. Japan, **100**, 342-345(1992).

10. Si_3N_4-TiN Porous Ceramics (Part 1)
— Microstructure and Electrical -properties in a Humid Atmosphere — 《Japanese》
S.Nakayama and H.Kuroshima,
J. Ceram. Soc. Japan, **100**, 758-762(1992).

11. Preparation and Properties of Perovskite-Type Oxides from Three-Dimensional Heterometal Assemblies, $\{Ln[Cr(ox)_3]\cdot 10H_2O\}X$ (Ln=La,Pr or Nd)
M.Sakamoto, K.Matsuki, R.Ohsumi, Y.Nakayama, Y.Sadaoka, S.Nakayama, N.Matsumoto and H.Okawa,
J. Ceram. Soc. Japan, **100**, 1211-1215(1992).

12. Preparation of Perovskite-type $LaFeO_3$ by Thermal Decomposition of Heteronuclear Complex, $\{La[Fe(CN)_6]\cdot 5H_2O\}x$
S.Nakayama, M.Sakamoto, K.Matsuki, Y.Okimura, R.Ohsumi, Y.Nakayama and Y.Sadaoka,
Chem. Lett., **1992**, 2145-2148.

13. Properties of Transparent Ceramic $Pb_{0.91}La_{0.09}Zr_{0.64}Ti_{0.34}O_3$ and Its Application of Window Material of Infrared Spectrophotometer 《Japanese》
S.Nakayama, M.Sakamoto, Y.Sadaoka and N.Ayuzawa,
Nippon Kagaku Kaishi, **1993**, 665-667.

14. Oxidation Behavior of RE- α -Sialon Cramics (RE=Nd,Sm,Gd,Dy, Y,Ho,Er,Yb) 《Japanese》
S.Nakayama, A.Shiranita, N.Ayuzawa and M.Sakamoto,
J. Ceram. Soc. Japan, **101**, 1184-1186(1993).

15. Microstructure and Humidity Sensitivity of Sintered $Zr(XPO_4)_2 \cdot nH_2O$(X=Li,Na,K,Rb,Cs)
S.Nakayama and Y.Sadaoka,
Shinagawa Technical Report, **37**, 99-104(1994).

16. Yittia-stabilized zirconia (Part 1)
– Thermal stability of B_2O_3-Al_2O_3-SiO_2 added Y-PSZ –
S.Nakayama, T.Ichimori, T.Mino and M.Sakamoto,
Shinagawa Technical Report, **38**, 43-48(1995).

Chapter 2

Ionic conductivity of ceramics prepared by sintering of $M_2CO_3 \cdot RE_2O_3 \cdot 2SiO_2$(M=Li,Na,K,Rb,Cs RE=La,Nd,Sm,Gd,Dy,Y,Ho,Er,Yb) mixtures

2-1. Introduction

Recently, there has been considerable interest in dense ionic conductors with high conductivities [17,70-72], because of their suitability for solid state batteries and/or chemical sensors [61,73,74]. In studies of sodium silicate glasses and glass ceramics containing cation modifiers such as Y^{3+} and Sn^{4+}, it has been confirmed that conductivity and activation energy are influenced by the cation modifier [75-77]. Choice of mobile cation, densification method and crystal structure play an important role in the development of batteries and/or chemical sensors.

β-eucryptite, $Li_2O \cdot Al_2O_3 \cdot 2SiO_2$, is known as a Li ionic conductor ($1 \times 10^{-6} S \cdot cm^{-1}$ at 300℃) possessing a conducting pathway in the direction along the minor axis of the hexagonal structure, where a three-dimensional network structure is built up by interconnected AlO_4 and SiO_4 tetrahedras. A number of research groups have discussed its structure and ion conduction mechanisms [78-81]. The present author has already developed humidity sensors using the porous ceramic $xLi_2O \cdot Al_2O_3 \cdot 2SiO_2$ [82]. It has been found from the chemical and electrical points of view that $Li_2O \cdot Al_2O_3 \cdot 2SiO_2$ is the most stable, whereas materials of $x \geqq 3$ react with CO_2 in air during the cooling process after sintering to form Li_2CO_3. Materials of $x \geqq 2$ lack the long-term stability needed for the humidity sensor. Furthermore, $Li_2O \cdot Al_2O_3 \cdot 2SiO_2$ has a fairly high resistance to water ; for example, when 10g of the sample sintered at 1300℃ is placed in 100ml of water at room temperature for 24h, only 22ppm of Li^+ ion is eluted. It is also reported that $(Li_2O)_{40.2}(Y_2O_3)_{5.7}(SiO_2)_{54.1}$ has a high conductivity ($3 \times 10^{-3} S \cdot cm^{-1}$ at 300℃) [83].

In order to develop well compacted alkali-metal ion solid electrolytes with high conductivities, alkali-metal (M) rare-earth (RE) silicates were prepared using a series of rare-earth elements instead of aluminum in $Li_2O \cdot Al_2O_3 \cdot 2SiO_2$, and their crystal structures, microstructures and electrical properties were investigated.

2-2. Experimental and analysis of electrical properties

2-2-1. Preparation of samples

M_2CO_3 (reagent-grade, M=Li,Na,K,Rb,Cs), RE_2O_3 (at least 99.9% purity, RE=La,Nd,Sm,Gd,Dy,Y,Ho,Er,Yb) and reagent-grade SiO_2 were used as starting materials. The starting materials were mixed in ethanol using a planet type ball-mill (using zirconia ball and plastic pot), dried and calcined in air for 2h in the temperature range 800 to 1000° C. In this case, it was difficult to prepare homogeneous samples because of intense aggultination during mixing when the rare-earths with ionic radii less than Dy are used for the Rb sreies. Similar results were obtained when the rare-earths with ionic radii less than Gd are used for the Cs series. The resultant powders were ball-milled into fine powders. After drying, discs were prepared under a pressure of 100MPa and sintered in air for 10h for the K series. The sintering period was 2h for the other series. The sintering temperatures are given in Table 2-1. During the sintering process, discs were supported by a spinal setter and sintered at temperatures, below which the reactions with the setter are initiated. The glass transition temperatures, Tg, of the calcined powders of the Li series were measured using a differential thermal analysis technique. The endothermic peak was observed at 1060, 1070, 1210, 1130 or 1233℃ for the Nd, Sm, Y, Ho or Er samples, respectively. The Tg's were 50-80℃ higher than the sintering temperatures shown in Table 2-1.

The alkali-metal rare-earth silicates prepared by sintering of $M_2CO_3 \cdot RE_2O_3 \cdot 2SiO_2$ mixtures are hereafter represented by M_2O-RE_2O_3-$2SiO_2$.

Table 2-1 Crystal parameters, phase and sintering temperature

	lattice constant				sintering
	a/nm	b/nm	c/nm	phase*	temp. / °C
$Li_2O-La_2O_3-2SiO_2$	0.9693		0.7154	H	1000
$Li_2O-Nd_2O_3-2SiO_2$	0.9541		0.6996	H	1000
$Li_2O-Sm_2O_3-2SiO_2$	0.9470		0.6916	H	1000
$Li_2O-Gd_2O_3-2SiO_2$	0.9416		0.6848	H	1000
$Li_2O-Dy_2O_3-2SiO_2$	0.9360		0.6769	H	1000
$Li_2O-Y_2O_3-2SiO_2$	0.4960	1.0698	0.6320	O	1100
$Li_2O-Ho_2O_3-2SiO_2$	0.4962	1.0696	0.6339	O	1050
$Li_2O-Er_2O_3-2SiO_2$	0.4958	1.0698	0.6315	O	1200
$Li_2O-Yb_2O_3-2SiO_2$	0.4926	1.0633	0.6249	O	1300
$Na_2O-La_2O_3-2SiO_2$	0.5476	0.9443	0.7144	O	1250
$Na_2O-Nd_2O_3-2SiO_2$	0.5395	0.9331	0.7019	O	1250
$Na_2O-Sm_2O_3-2SiO_2$	0.5361	0.9267	0.6964	O	1250
$Na_2O-Gd_2O_3-2SiO_2$	0.5333	0.9206	0.6926	O	1250
$Na_2O-Dy_2O_3-2SiO_2$	0.5290	0.9136	0.6879	O	1300
$Na_2O-Y_2O_3-2SiO_2$	0.5273	0.9105	0.6856	O	1350
$Na_2O-Ho_2O_3-2SiO_2$	0.5274	0.9107	0.6857	O+U	1350
$Na_2O-Er_2O_3-2SiO_2$				U	1350
$K_2O-La_2O_3-2SiO_2$	0.9708		0.7244	H	1350
$K_2O-Nd_2O_3-2SiO_2$	0.9562		0.7089	H	1350
$K_2O-Sm_2O_3-2SiO_2$	0.9484		0.7002	H	1350
$K_2O-Gd_2O_3-2SiO_2$	0.9434		0.6934	H	1350
$K_2O-Dy_2O_3-2SiO_2$	0.9371		0.6851	H	1350
$K_2O-Y_2O_3-2SiO_2$				U	1350
$K_2O-Ho_2O_3-2SiO_2$				U	1350
$K_2O-Er_2O_3-2SiO_2$				U	1350
$Rb_2O-La_2O_3-2SiO_2$	0.9716		0.7259	H	1300
$Rb_2O-Nd_2O_3-2SiO_2$	0.9561		0.7091	H	1300
$Rb_2O-Sm_2O_3-2SiO_2$	0.9480		0.6999	H	1300
$Rb_2O-Gd_2O_3-2SiO_2$				U	1350
$Cs_2O-La_2O_3-2SiO_2$	0.9607		0.7236	H	1400
$Cs_2O-Nd_2O_3-2SiO_2$	0.9556		0.7076	H	1400
$Cs_2O-Sm_2O_3-2SiO_2$	0.9473		0.6933	H	1400

* H : hexagonal, O : orthorhombic, U : unknown mixture.

2-2-2. Measurements

The elemental analyses were confirmed by X-ray fluorescence (Rigaku, 3080E) and atomic absorption spectrophotometry (Hitachi, Z-8100). The crystal structures were determined at room temperature by powder X-ray diffraction (Rigaku, RAD-rA). The microstructures were determined by scanning electron microscopy (Nihon-Densi, JSM6400). The prepared discs were 8mm in diameter and 2mm in thickness after sintering. After coating both sides of the disc with Pt paste, it was baked at 950℃. The electrical measurement device and the equipment are shown in Fig.2-1.

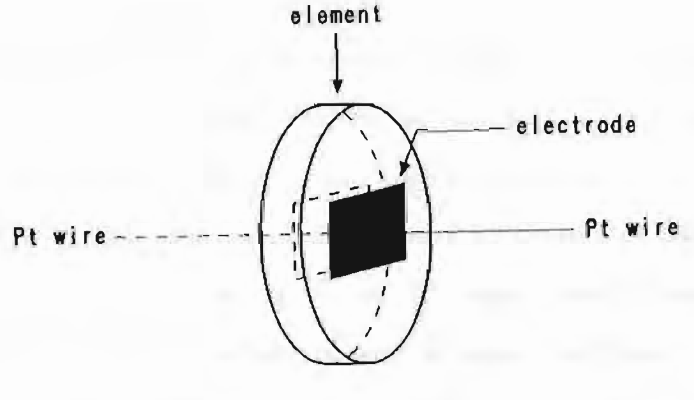

Fig. 2-1(a) Schematic view of the electrical property measurement device.

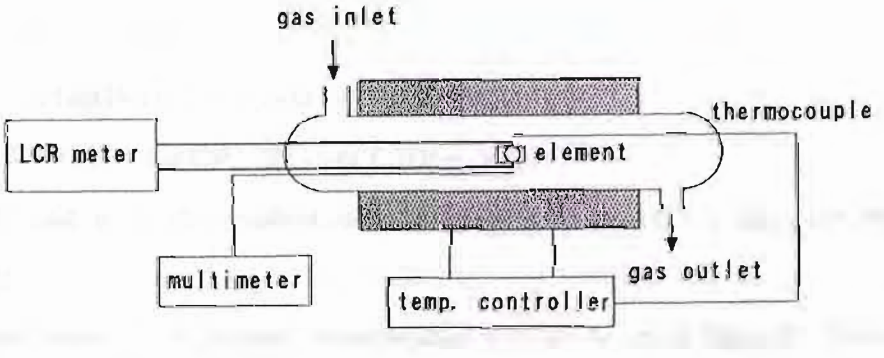

Fig. 2-1(b) Schematic view of the electrical property measurement equipment.

The electrical properties were measured using a multifrequency LCR meter (Yokogawa Hewlett-Packard, 4192A) in the frequency range of 100Hz to 10MHz and temperature range from 100 to 800℃. The device was heated to 300℃ in order to eliminate adsorbed water prior to each measurement.

2-2-3. Analysis of electrical properties for solid electrolyte
- Complex impedance analysis - [84]

When an electrical current is applied to a material, the response voltage is indicative of its electrical properties. The measuring methods of electrical properties include a direct current method and an alternating current method at a fixed frequency. However, little information is obtained by these methods and the data is often unreliable. In order to overcome these limitations, complex impedance analysis which consists of a Cole-Cole plot method and an equivalent circuit analysis method has been applied. This method is based on the measurement of the frequency dependence of the impedance and gives information on bulk conduction, grain boundary conduction and interface conduction.

The impedance (Z) can be expressed by the vector sum of the real component (Z') and the imaginary component (Z") and is described as follows :

$$Z = Z' + jZ''$$
$$= G/(G^2+(\omega C)^2 + j(-\omega C/(G^2+(\omega C)^2) \quad (2\text{-}1)$$
$$Z' = G/(G^2+(\omega C)^2, \quad Z'' = -\omega C/(G^2+(\omega C)^2 \quad (2\text{-}2)$$

where G, C and ω is the conductance, the capacitance and the angular frequency, respectively.

A typical example of a complex impedance plot is shown in Fig.2-2. In the lower temperature region, a semicircle which passes through the origin and the spur are observed (Fig.2-2(a)). The spur is probably caused by the electrolyte-electrode behaviour. It is suggested that the equivalent circuit may be simplified to the parallel one which consists of the resistance component, Rp, and the capacitance component, Cp. On the other hand, in the higher temperature region only the spur is observed as shown in Fig.2-2(b). This is also the case in the higher conductivity materials. This is because Cp becomes negligibly small as Rp decreases. As a result, the following simplified equivalent circuit is adequate author's purpose. Its property is intermediate between the two equivalent circuits : one is the equivalent circuit where Rp is connected in series with the double layer capacity of electrolyte-electrode boundary, Cd, and another is the circuit where Rp is connected in series with the Warburg impedance, W.

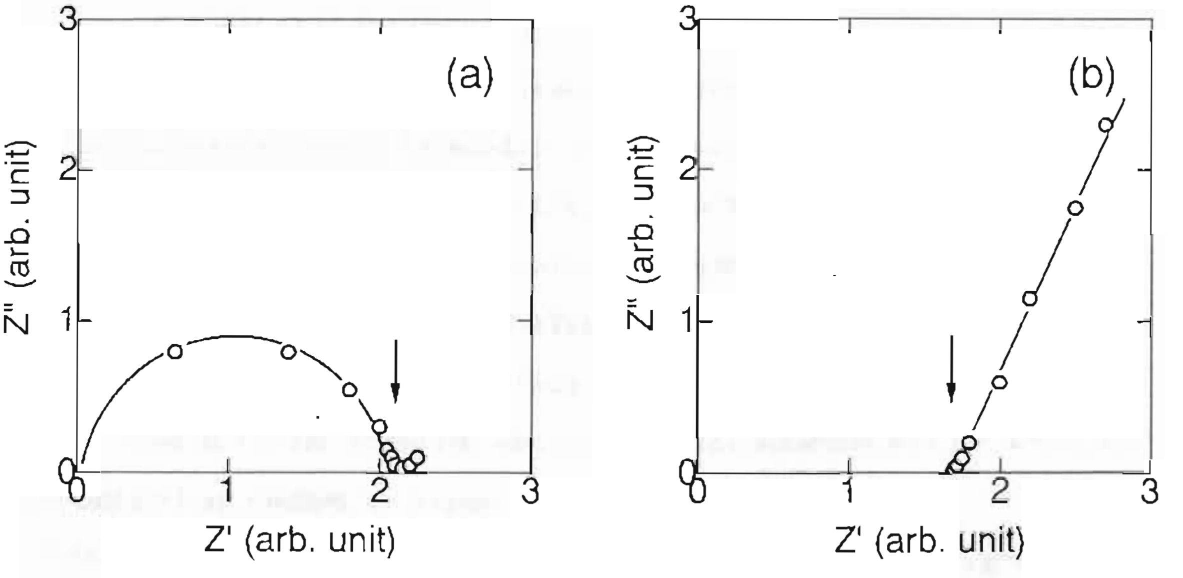

Fig. 2-2 Complex impedance plots :
(a) lower temperature region,
(b) higher temperature region.

In Fig.2-2(a), the resistance component, Rp, is determined by the extrapolation of the semicircle to the real axis. In Fig.2-2(b), Rp is determined from the point of intersection of the real axis and the spur. Then, the resistance value (R) is expressed by equation (2-3) :

$$R = \rho \cdot d/S \qquad (2\text{-}3)$$

where ρ, S and d are the resistivity, the electrode area and the electrode spacing, respectively. The relationship between the conductivity (σ) and the resistivity (ρ) is shown by equations (2-4) and (2-5). The conductivity (ρ) can be calculated by assuming Rp=R.

$$\sigma = 1/\rho \tag{2-4}$$

$$= 1/R \cdot d/S \tag{2-5}$$

- **Electrical conductivity** -

Generally, the magnitude of ionic conductivity for a solid electrolyte can be well understood by random walk theory [85,86]. This theory assumes that the mobile ions move independently of each other. The ionic conductivity (G) is expressed as follows :

$$G \cdot T = N \cdot e^2 \cdot a^2 \cdot C(1-C) \cdot \gamma \cdot k^{-1} \cdot \omega_0 \cdot \exp(-F/kT) \tag{2-6}$$

where T is the absolute temperature, k is the Boltzmann's constant, N is the number of sites available for occupation by mobile ions, C is a partial occupation factor of mobile ions, ω_0 is the basic frequency of mobile ions, e is the electronic charge, a is the average jumping distance, γ is a correlation coefficient and F is the activation energy for ionic conduction. Moreover, exp(-F/kT) is shown by equation (2-7) :

$$\exp(-F/kT) = \exp(S/k) \cdot \exp(-H/kT) \tag{2-7}$$

where S and H are the activation entropy for ionic conduction and the activation enthalpy for ionic conduction, respectively.

The temperature dependence of conductivity of the solid electrolyte is governed by the activation energy for migration of the carrier, Fm, and the activation energy for the carrier creation, Fc.

$$Fm = Hm - T \cdot Sm \tag{2-8}$$

$$Fc = Hc - T \cdot Sc \tag{2-9}$$

Accordingly, equation (2-6) may be rewritten :

$$G \cdot T = N \cdot e^2 \cdot a^2 \cdot C(1-C) \cdot \gamma \cdot k^{-1} \cdot \omega_0 \cdot \exp(-(Fm+Fc)/kT) \tag{2-10}$$

In the case of $G' = N \cdot e^2 \cdot a^2 \cdot C(1-C) \cdot \gamma \cdot k^{-1} \cdot \omega_0$, equation (2-10) may be simplified.

$$G \cdot T = G' \cdot \exp((Sm+Sc/2)/kT) \cdot (-(Hm+Hc/2)/kT) \tag{2-11}$$

G' and the entropy term are incorporated in the pre-exponential factor (G_0). The above equation may be further simplified to the form of the Arrhenius equation.

$$G \cdot T = G_0 \cdot \exp(-E/kT) \tag{2-12}$$

where E is the activation energy. E and G_0 are dependent on the temperature.

2-3. Results and discussion

2-3-1. Elemental analysis

The alkali-metal rare-earth silicate samples (M_2O-RE_2O_3-$2SiO_2$) were prepared from a mixture of $M_2CO_3 \cdot RE_2O_3 \cdot 2SiO_2$ (M=Li,Na,K,Rb,Cs RE=La,Nd,Sm,Gd,Dy, Y,Ho,Er,Yb) at relatively high temperatures of 1000 to 1400℃ as shown in Table 2-1. As the composition change (especially alkali-metal) may occur during sintering, elemental analyses were carried out using a X-ray fluorescence technique except for the samples containing lithium. Here, the quantitative analyses were carried out for the sample K_2O-La_2O_3-$2SiO_2$. For the other samples containing Na, K, Rb or Cs, the X-ray fluorescent intensity ratios (I(M)/I(RE), I(M)/I(Si), I(RE)/I(Si)) were calculated. Lithium content was determined using an atomic absorption technique after the dissolution in HF. These results are summarized in Tables 2-2 and 2-3.

In the Li series, 2-15% decreases in the Li content were observed after sintering. The composition of K_2O-La_2O_3-$2SiO_2$ was $(K_2O)_{0.661}(La_2O_3)_{1.000}(2SiO_2)_{0.915}$ and the decrease in the K and Si contents was about 30 and 10%, respectively. In the Na, K, Rb and Cs series, the alkali-metal and Si contents significantly decreased, though the absolute content of each element was not clear. The decrease of alkali-metal content were in the order of the Na $<$ K $=$ Rb $<$ Cs series. This order may be due to the difference in sintering temperature. The decrease of alkali-metal and Si contents may be due to the vaporization or the reaction of alkali-metal silicates with the setter used in this work.

Table 2-2 Atomic absorption data

	Li/wt%	
	calcd	found
Li_2O-La_2O_3-$2SiO_2$	2.92	2.86
Li_2O-Nd_2O_3-$2SiO_2$	2.85	2.43
Li_2O-Sm_2O_3-$2SiO_2$	2.78	2.65
Li_2O-Gd_2O_3-$2SiO_2$	2.71	2.43

Table 2-3 X-ray fluorescence data of M_2O-RE_2O_3-$2SiO_2$

		I(M)/I(RE)	I(M)/I(Si)	I(RE)/I(Si)
Na_2O-Sm_2O_3-$2SiO_2$	(B)	0.095	0.161	1.689
〃	(A)	0.099	0.329	3.330
K_2O-La_2O_3-$2SiO_2$	(B)	3.914	2.291	0.585
〃	(A)	2.096	2.096	0.720
K_2O-Nd_2O_3-$2SiO_2$	(B)	1.867	2.314	1.239
〃	(A)	1.118	1.733	1.551
K_2O-Sm_2O_3-$2SiO_2$	(B)	1.222	2.003	1.666
〃	(A)	0.786	2.142	2.724
Rb_2O-Sm_2O_3-$2SiO_2$	(B)	3.494	7.203	2.062
〃	(A)	1.435	4.527	3.154
Cs_2O-Sm_2O_3-$2SiO_2$	(B)	0.327	0.535	1.636
〃	(A)	0.056	0.148	2.655

(B) : starting mixture, (A) : sintered sample.

2-3-2. Crystal structure

Table 2-4 summarizes the XRD results for M_2O-La_2O_3-$2SiO_2$ (M=Li,K,Rb,Cs). In the range $10^\circ \leqq 2\theta \leqq 50^\circ$, most of the observed peaks can be assigned as indicated in Table 2-4. Some undefined peaks are also observed but the relative intensities ($100I/I_0$) of those peaks are <5. For the Li series, a hexagonal phase was confirmed for RE=La, Nd, Sm, Gd and Dy and an othorhombic phase for RE=Y, Ho, Er and Yb. The observed XRD patterns for RE=La, Nd, Sm, Gd and Dy, are very similar to that of $LiLa_9(SiO_4)_6O_2$ (JCPDS no.32-567, hexagonal, $P6_3/m(176)$, a=0.9692nm, c=0.7167nm) and $LiLaSiO_4$ (JCPDS no.20-630, a=0.969nm, c=0.715nm) with a hexagonal structure. The lattice constants of the hexagonal phase were estimated with the aid of the $LiLa_9(SiO_4)_6O_2$ result and those of orthorhombic phase with the aid of the $LiYSiO_4$ result (JCPDS no.20-643, orthorhombic, a=0.496nm, b=1.068nm, c=0.629nm). For the Na series, an orthorhombic phase was confirmed for RE=La, Nd, Sm, Gd, Dy, Y and Ho. However, for RE=Dy, Y and Ho, the XRD pattern was very complex, implying the coexistence of a number of different phases. The lattice constants of the orthorhombic phase were estimated assuming a orthorhombic phase which is observed $NaLaSiO_4$ (JCPDS no.20-1116, orthorhombic, Pnma(62), a=0.546nm, b=0.940nm, c=0.709nm). The XRD patterns of K_2O-RE_2O_3-$2SiO_2$ (RE=La,Nd,Sm,Gd,Dy) and M_2O-RE_2O_3-$2SiO_2$ (M=Rb,Cs RE=La,Nd,Sm) are very similar to those of $LiLa_9(SiO_4)_6O_2$. The lattice constants of those were estimated by assuming a hexagonal phase. The XRD results of Na_2O-Er_2O_3-$2SiO_2$, K_2O-RE_2O_3-$2SiO_2$ (RE=Y,Ho,Er) and Rb_2O-Gd_2O_3-$2SiO_2$ were very complex, probably due to a mixture of other compounds. The estimated lattice constants are summarized in Table 2-1.

Table 2-4 XRD patterns of M_2O-La_2O_3-$2SiO_2$ (M=Li, K, Rb, Cs)

h k l*	Li d/nm	Li I/I_0 x100	K d/nm	K I/I_0 x100	Rb d/nm	Rb I/I_0 x100	Cs d/nm	Cs I/I_0 x100
1 1 0	.4696	5	.4852	3	.4858	4	.4839	3
2 0 0	.4195	25	.4204	20	.4205	21	.4191	20
1 1 1	.4011	21	.4031	17	.4033	17	.4019	17
0 0 2	.3573	20	.3620	14	.3623	13	.3609	15
1 0 2	.3285	32	.3323	27	.3326	31	.3315	30
2 1 0	.3168	29	.3176	25	.3178	27	.3169	27
2 1 1	.2897	100	.2905	100	.2907	100	.2899	100
1 1 2	.2875	47						
3 0 0	.2795	24	.2801	23	.2803	24	.2795	23
3 0 1	.2710	5	.2742	3	.2744	4	.2736	3
3 1 0	.2327	8	.2329	6	.2332	6	.2326	6
2 2 1	.2293	2	.2296	3	.2301	4	.2295	3
3 1 1								
1 1 3	.2138	11	.2159	8	.2163	9	.2156	9
4 0 0	.2096	7	.2099	4	.2101	6	.2096	4
2 2 2	.2004	16	.2014	18	.2017	20	.2012	17
3 1 2	.1950	11	.1959	12	.1961	12	.1956	11
3 2 0	.1926	3			.1924	23	.1918	24
2 1 3	.1904	25	.1920	24				
3 2 1	.1858	14	.1862	12	.1864	12	.1860	12
4 1 0	.1830	14	.1833	14	.1836	14	.1831	15
4 0 2	.1808	18	.1815	17	.1817	18	.1813	17

* JCPDS file no. 32-567, $LiLa_9(SiO_4)_6O_2$, hexagonal, $P6_3/m$(176), a=0.9692nm, c=0.7167nm.

In each alkali-metal series, the lattice constants, a and c, of M_2O-RE_2O_3-$2SiO_2$

bearing hexagonal structure increase monotonically with an increase in the ionic radius of RE as shown in Fig.2-3. Furthermore, in the hexagonal group, the highest values of a- and c-lattice constants are observed for K_2O-RE_2O_3-$2SiO_2$ as shown in Fig.2-4.

The hexagonal phase formed in M_2O-RE_2O_3-$2SiO_2$ (M=Li,K for RE=La,Nd,Sm,Gd,Dy ; M=Rb,Cs for RE=La,Nd,Sm) is considered to have an apatite structure with the composition $M_xRE_{10\text{-}x}(SiO_4)_6O_{3\text{-}x}$ (X=1-3) [87-89]. As described in section 2-3-1, both the alkali-metal and Si contents of the sintered samples are lower than those of the starting mixtures ($K_2O \cdot La_2O_3 \cdot 2SiO_2$). The composition is $(K_2O)_{0.661}(La_2O_3)_{1.000}(2SiO_2)_{0.915}$ ($K_{1.334}La_{6.052}(SiO_4)_6O_m$) which is close to the apatite composition. However, taking into consideration that the maximum value of X is 3 for the apatite structure, the remaining alkali-metal and Si must exist as another phase in the sintered sample. The XRD peaks due to the RE_2O_3, SiO_2 and alkali-metal silicates were scarcely observed, suggesting that the apatite structure of $M_xRE_{10\text{-}x}(SiO_4)_6O_{3\text{-}x}$ (X=1-3) is a major phase. (Moreover, the molar ratio of Sm and Si for the bulk (probably major phase) in M_2O-Sm_2O_3-$2SiO_2$ (M=Li,K,Rb,Cs) measured

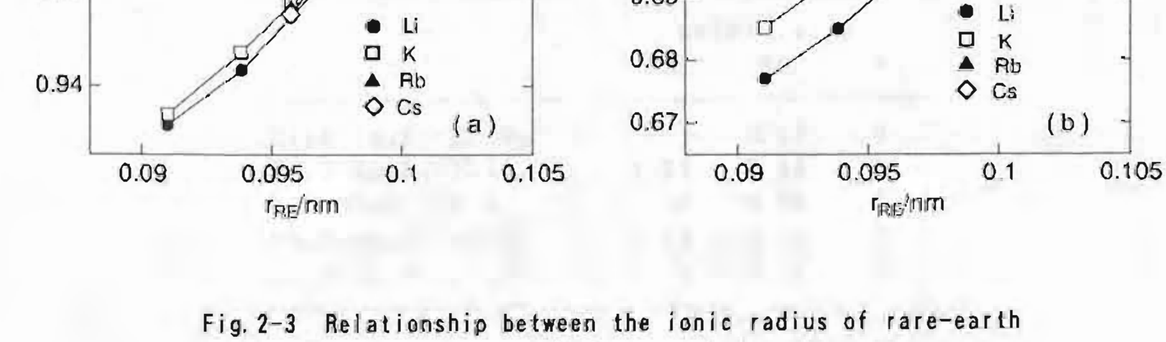

Fig. 2-3 Relationship between the ionic radius of rare-earth and the lattice constants in hexagonal M_2O-RE_2O_3-$2SiO_2$: (a) a-axis, (b) c-axis.

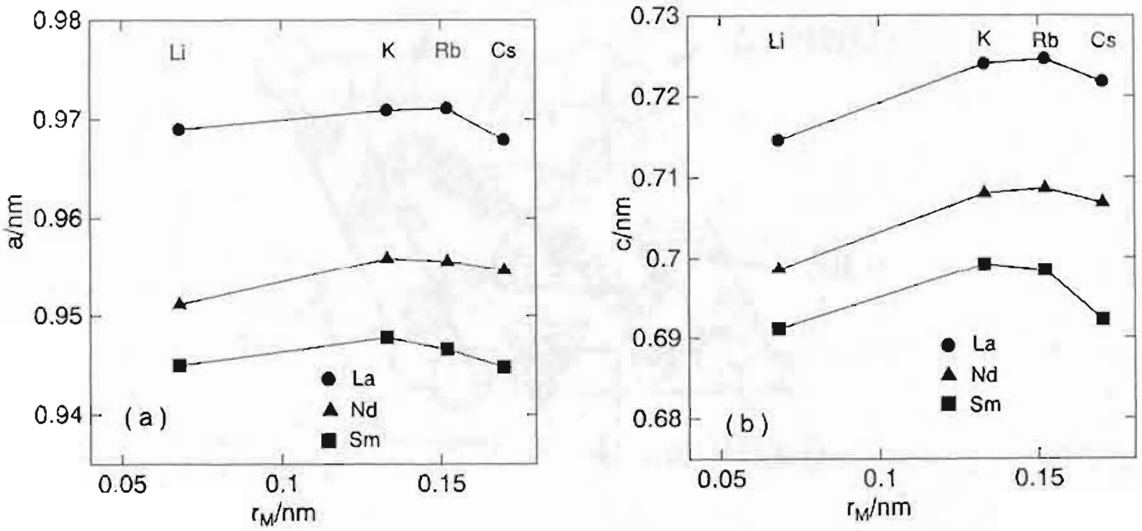

Fig. 2-4 Relationship between the ionic radius of alkali-metal and the lattice constants in hexagonal M_2O-RE_2O_3-$2SiO_2$: (a) a-axis, (b) c-axis.

by EPMA agreed with that of the apatite composition as summarized in Table 2-5.) The glass phases such as alkali-metal silicates and unassignable crystalline phase are present as minor components.

The hexagonal apatite structure proposed to the major phase of Li_2O-RE_2O_3-$2SiO_2$ by M.Sato et al. are shown in Fig.2-5 [89].

Table 2-5 Electron probe microanalysis data of bulk (major phase) in M_2O-Sm_2O_3-$2SiO_2$

	molar ratio		
	M	Sm	Si
Li_2O-Sm_2O_3-$2SiO_2$	-	8.50	6
Na_2O-Sm_2O_3-$2SiO_2$	1.31	0.94	1
K_2O-Sm_2O_3-$2SiO_2$	1.28	8.22	6
Rb_2O-Sm_2O_3-$2SiO_2$	0.38	8.34	6
Cs_2O-Sm_2O_3-$2SiO_2$	0.19	8.24	6

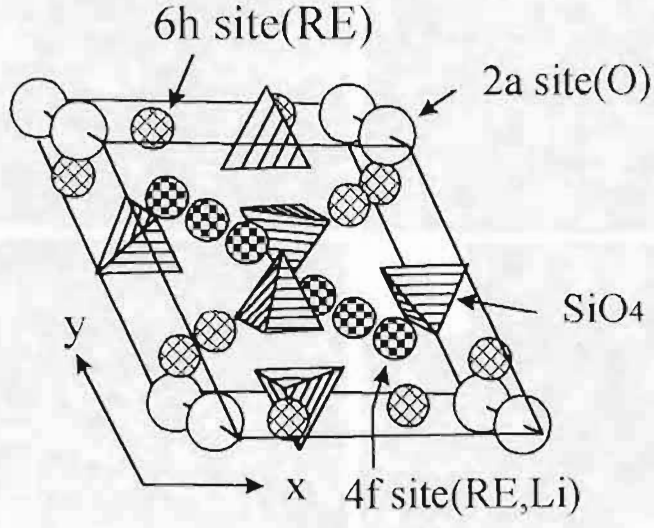

Fig. 2-5 Hexagonal apatite structure proposed to the major phase of Li_2O-RE_2O_3-$2SiO_2$ [89].

2-3-3. Microstructure

Figure 2-6 shows the fracture surface microstructures of the sintered alkali-metal rare-earth silicates. In the Li series, sintering was well progressed for the Nd and Sm samples. The porosity and the particle diameter for the Gd and Dy samples are greater than those for the Nd and Sm samples. The fracture surface of the Y, Ho and Yb samples was very different from that for the La, Nd, Sm, Gd and Dy samples. These differences can be assigned to the crystal structure as summarized in Table 2-1. In the Na series for RE=La, Nd, Sm and Gd, the each microstructure is very similar and sintering is well progressed. Porous structures are observed for the Dy, Y, Ho and Er samples. In the K series, plate-like crystals were observed for the La, Nd and Sm samples. By decreasing ionic radius of rare-earth, the number of plate-like crystals decreased and needle-like crystals formed as a major component, especially in the case of the Dy sample. The microstructures of Y, Ho and Er samples consisted of round particles with a high degree of interconnection. In the Rb series, needle-like crystals having a small aspect ratio and porous structures were observed. The aspect ratio increased with decreasing ionic radius of rare-earth. In the Cs series, well defined plate-like crystals were formed. The crystals formed a layered structure, and interfusion and sintering were not observed.

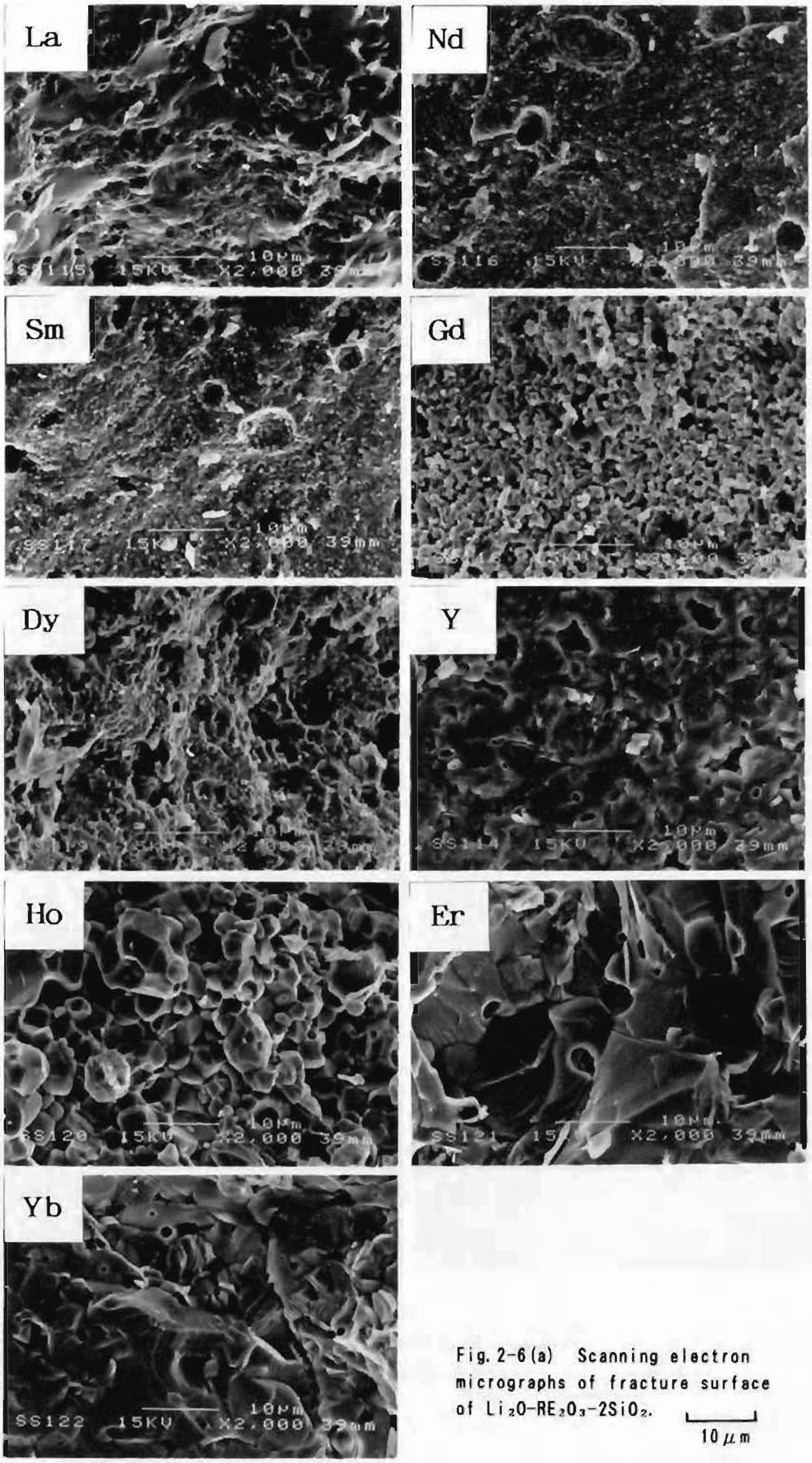

Fig. 2-6 (a) Scanning electron micrographs of fracture surface of Li_2O-RE_2O_3-$2SiO_2$.

10 μm

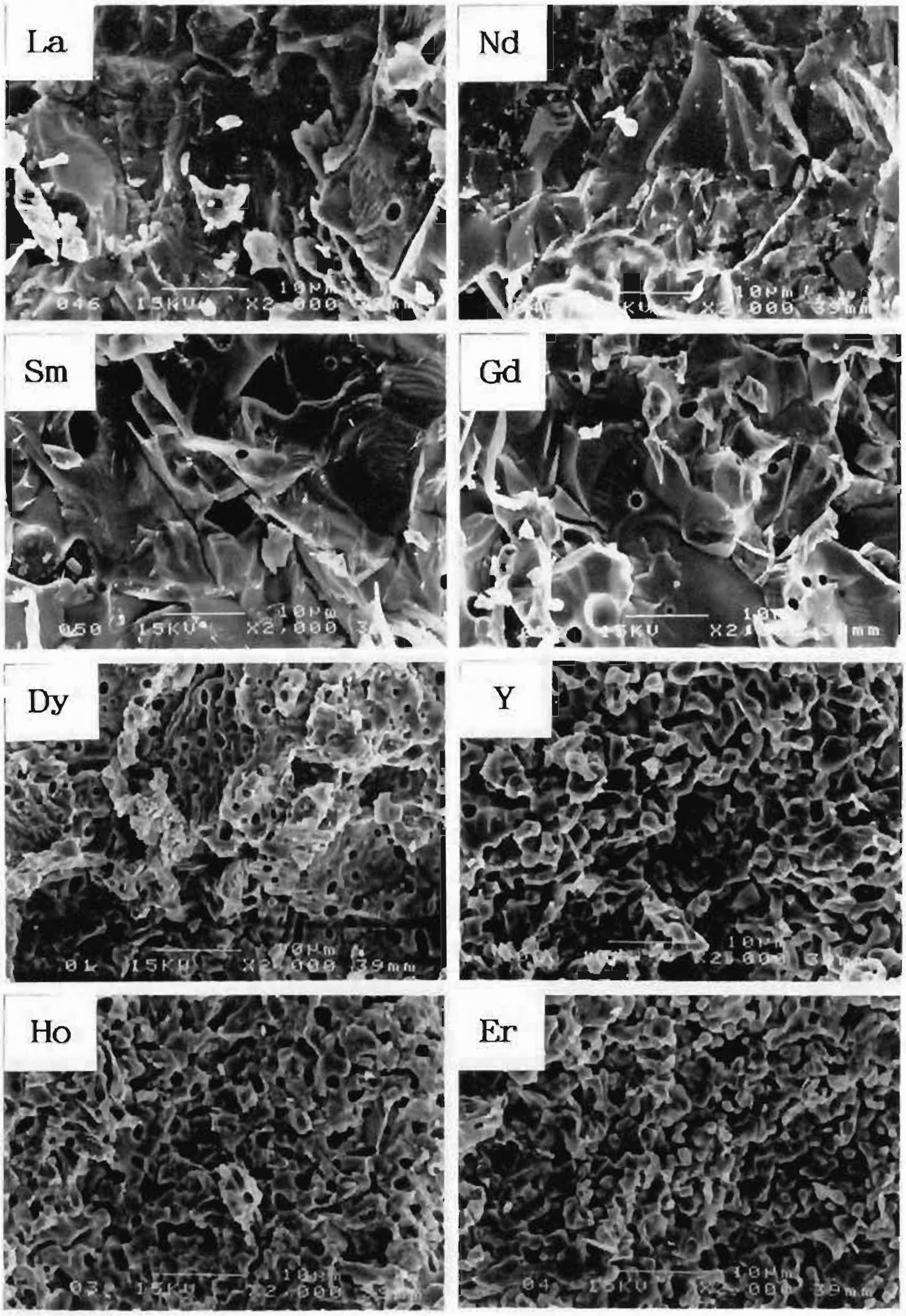

Fig. 2-6(b) Scanning electron micrographs of fracture surface of $Na_2O-RE_2O_3-2SiO_2$.

10 μm

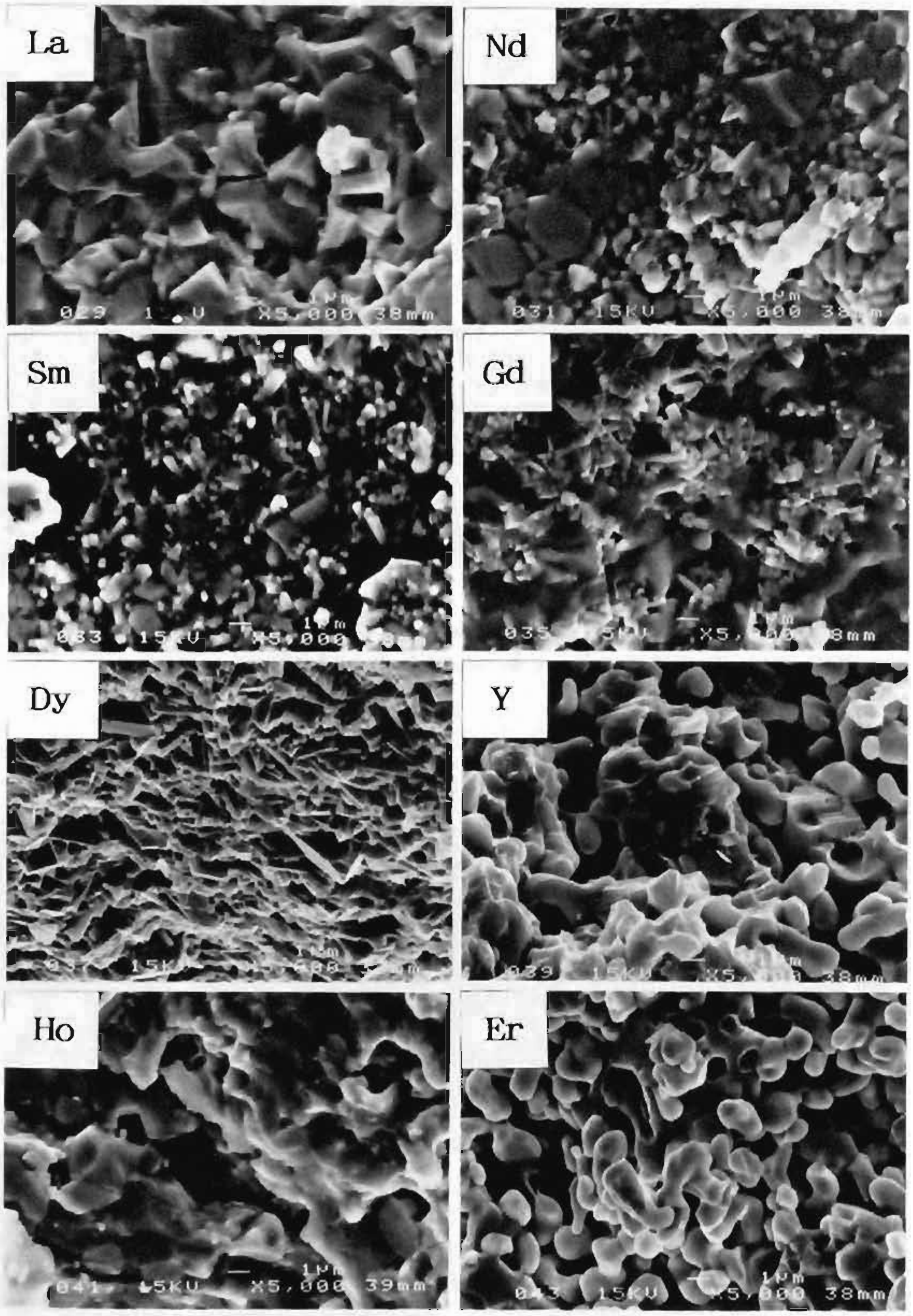

Fig. 2-6(c) Scanning electron micrographs of fracture surface of K_2O-RE_2O_3-$2SiO_2$.

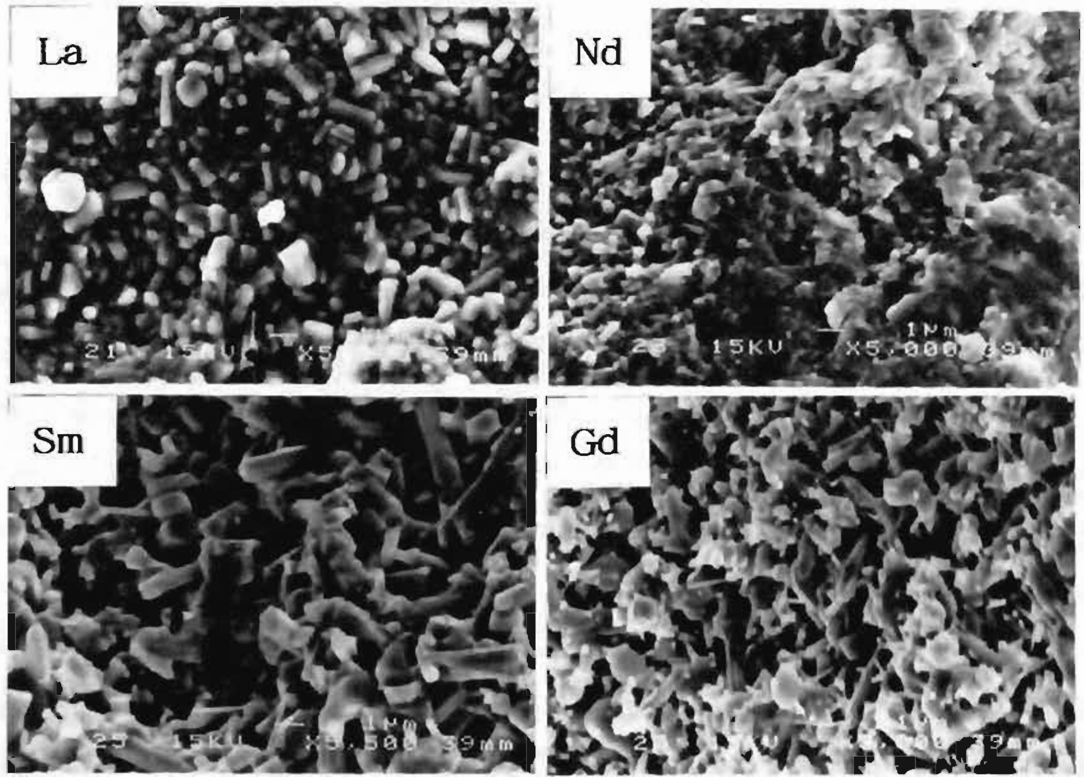

Fig. 2-6 (d) Scanning electron micrographs of fracture surface of Rb_2O-RE_2O_3-$2SiO_2$.

5 μm

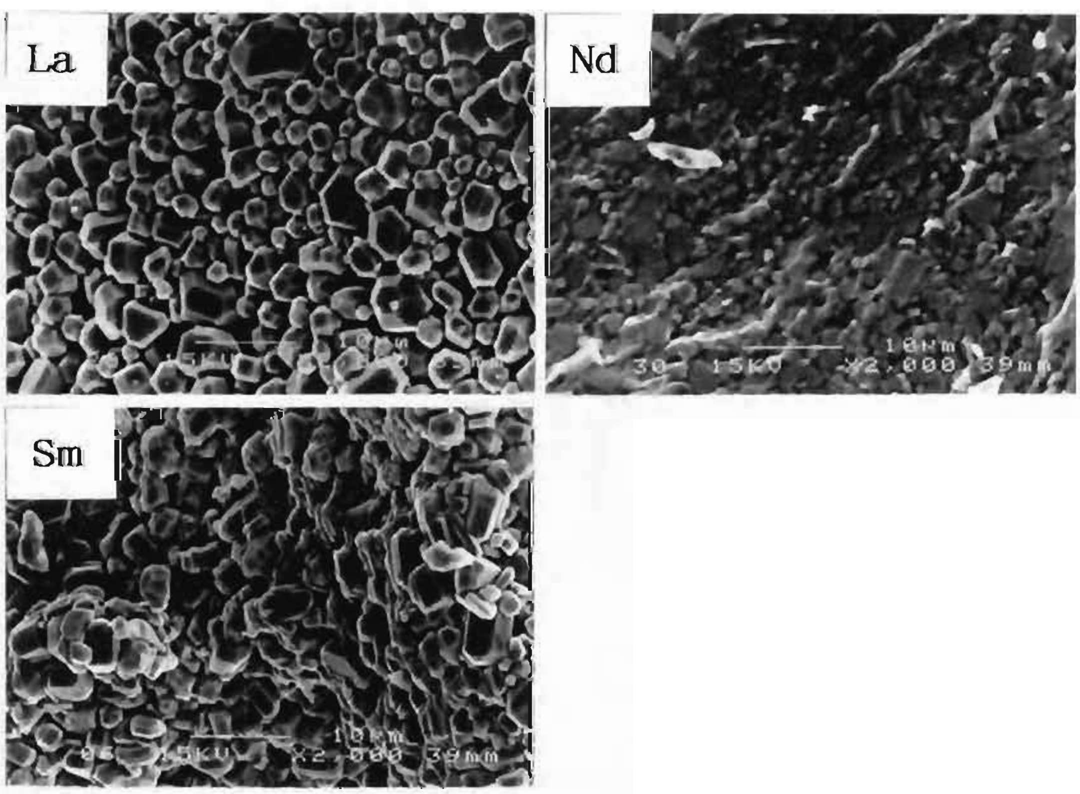

Fig. 2-6 (e) Scanning electron micrographs of fracture surface of Cs_2O-RE_2O_3-$2SiO_2$.

10 μm

2-3-4. Electrical properties

To determine the conductivity component, complex plane impedance analysis was used. In the lower temperatures, the low-frequency plots were represented by a spur and the high-frequency plots by a semicircle which passed through the origin ; in some cases a second semicircle was observed as shown Fig.2-7. The semicircle in the higher frequency region corresponds probably to the bulk component, whereas the second semicircle in the lower frequency region corresponds to the grain boundary component. When the temperature was increased, the semicircle diminished and only a spur probably caused by the electrolyte-electrode behaviour was observed for all samples. From these results, the total conductivity was determined by extrapolation to zero reactance of the complex impedance plot. The total conductivity data (the sum of the bulk and grain boundary) were parameterized by the Arrhenius equation (2-12).

The current responses for a potenial change from +1 to -1V of Pt | M_2O-RE_2O_3-$2SiO_2$ | Pt were examined. No rapid decline in current was observed after the polar change and then the current approached to zero for a very long time. These results indicate that ions are primarily responsible for the electrical conduction.

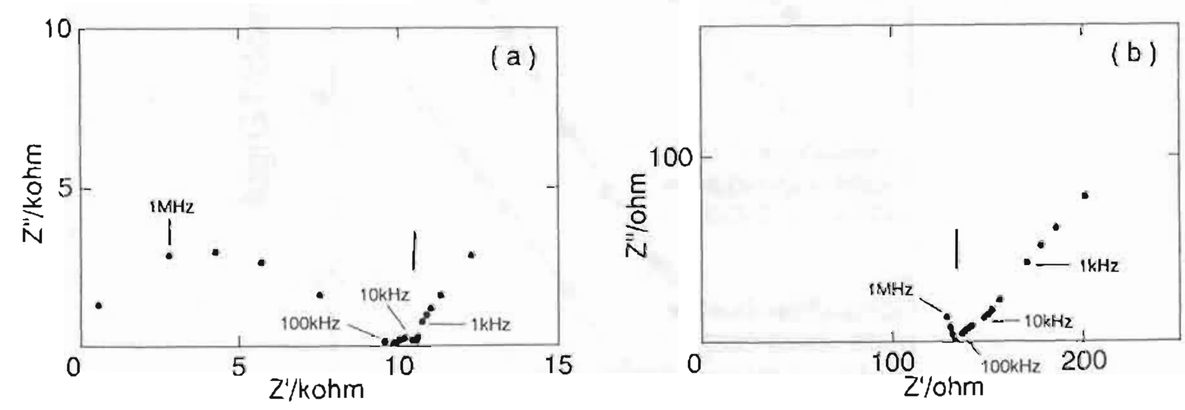

Fig. 2-7 Complex impedance plots of K_2O-La_2O_3-$2SiO_2$:
(a) at 120°C, (b) at 300°C.

Figure 2-8 shows Arrhenius plots. The electrical characteristics are summarized in Table 2-6. Since the hexagonal samples, especially K_2O-RE_2O_3-$2SiO_2$, show relatively high conductivities and low activation energies, their electrical properties were investigated next. The electrical properties of the hexagonal samples may be mainly dependent on the bulk component from the following reason. The conductivity due to the bulk (probably major phase) is smaller compared with that due to the grain boundary. Therefore, it is presumed that the ionic conduction in the bulk is the rate-determined step since the bulk is connected in series with the grain boundary. Inflection points appeared in the slopes of Arrhenius plots for K_2O-RE_2O_3-$2SiO_2$ and Rb_2O-RE_2O_3-$2SiO_2$. Since the high temperature XRD pattern of the major phase in K_2O-Sm_2O_3-$2SiO_2$ did not change below 1200℃, the appearance of inflection point is not attributable to a phase transformation. It is reported that such inflection points

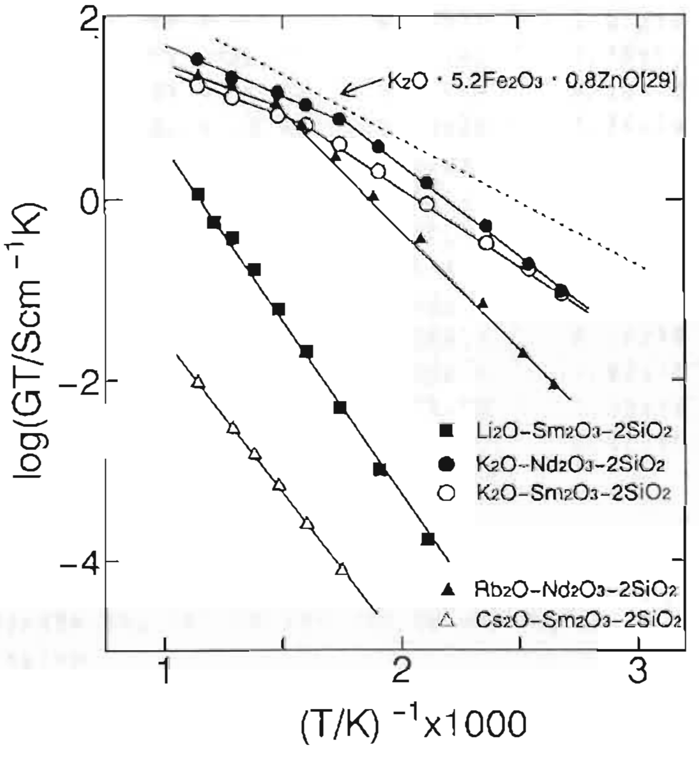

Fig. 2-8 Arrhenius plots.

Table 2-6 Electrical parameters

	activation energy /kJ·mol^{-1}	conductivity/S·cm^{-1} 300°C	400°C	500°C
Li_2O-La_2O_3-$2SiO_2$	75.7	6.06×10^{-6}	6.41×10^{-5}	2.98×10^{-4}
Li_2O-Nd_2O_3-$2SiO_2$	86.6	4.15×10^{-6}	7.06×10^{-5}	5.29×10^{-4}
Li_2O-Sm_2O_3-$2SiO_2$	78.4	8.93×10^{-6}	9.42×10^{-5}	4.92×10^{-4}
Li_2O-Gd_2O_3-$2SiO_2$	97.7	2.81×10^{-7}	4.45×10^{-6}	3.98×10^{-5}
Li_2O-Dy_2O_3-$2SiO_2$	117.8	4.97×10^{-7}	1.57×10^{-5}	2.07×10^{-4}
Li_2O-Y_2O_3-$2SiO_2$	95.9	-	2.75×10^{-7}	2.21×10^{-6}
Li_2O-Ho_2O_3-$2SiO_2$	122.3	-	1.48×10^{-6}	2.17×10^{-5}
Li_2O-Er_2O_3-$2SiO_2$	104.5	-	-	1.47×10^{-6}
Li_2O-Yb_2O_3-$2SiO_2$	100.0	-	-	7.94×10^{-7}
Na_2O-La_2O_3-$2SiO_2$	68.9	1.98×10^{-6}	1.55×10^{-5}	1.17×10^{-4}
Na_2O-Nd_2O_3-$2SiO_2$	69.5	3.01×10^{-6}	2.09×10^{-5}	1.25×10^{-4}
Na_2O-Sm_2O_3-$2SiO_2$	69.0	3.01×10^{-6}	2.39×10^{-5}	1.10×10^{-4}
Na_2O-Gd_2O_3-$2SiO_2$	72.7	9.71×10^{-7}	7.14×10^{-6}	3.47×10^{-5}
Na_2O-Dy_2O_3-$2SiO_2$	91.1	-	-	2.15×10^{-6}
Na_2O-Y_2O_3-$2SiO_2$	123.0	-	-	8.77×10^{-7}
Na_2O-Ho_2O_3-$2SiO_2$	93.0	-	3.25×10^{-7}	2.99×10^{-6}
Na_2O-Er_2O_3-$2SiO_2$	95.3	4.74×10^{-7}	2.07×10^{-6}	1.56×10^{-5}
K_2O-La_2O_3-$2SiO_2$	48.1 (26.7)	2.35×10^{-3}	7.25×10^{-3}	1.18×10^{-2}
K_2O-Nd_2O_3-$2SiO_2$	38.4 (20.2)	1.31×10^{-2}	2.16×10^{-2}	2.78×10^{-2}
K_2O-Sm_2O_3-$2SiO_2$	32.8 (18.0)	7.14×10^{-3}	1.24×10^{-2}	1.71×10^{-2}
K_2O-Gd_2O_3-$2SiO_2$	34.3 (20.6)	4.05×10^{-4}	9.71×10^{-4}	1.40×10^{-5}
K_2O-Dy_2O_3-$2SiO_2$	54.6 (42.5)	5.88×10^{-5}	2.94×10^{-4}	6.13×10^{-4}
K_2O-Y_2O_3-$2SiO_2$	53.7 (34.4)	1.19×10^{-5}	2.71×10^{-5}	5.81×10^{-5}
K_2O-Ho_2O_3-$2SiO_2$	54.5 (33.6)	7.04×10^{-5}	1.89×10^{-4}	3.09×10^{-4}
K_2O-Er_2O_3-$2SiO_2$	42.9 (29.7)	5.38×10^{-5}	1.02×10^{-4}	1.66×10^{-4}
Rb_2O-La_2O_3-$2SiO_2$	84.1 (28.6)	4.22×10^{-3}	9.96×10^{-3}	1.40×10^{-2}
Rb_2O-Nd_2O_3-$2SiO_2$	51.4 (22.7)	5.02×10^{-3}	1.62×10^{-2}	2.29×10^{-2}
Rb_2O-Sm_2O_3-$2SiO_2$	55.7 (33.0)	4.79×10^{-4}	1.95×10^{-3}	3.99×10^{-3}
Rb_2O-Gd_2O_3-$2SiO_2$	50.8	2.05×10^{-4}	6.40×10^{-4}	2.19×10^{-3}
Cs_2O-La_2O_3-$2SiO_2$	77.7	-	-	7.09×10^{-6}
Cs_2O-Nd_2O_3-$2SiO_2$	60.2	-	-	5.01×10^{-6}
Cs_2O-Sm_2O_3-$2SiO_2$	66.2	1.35×10^{-7}	1.01×10^{-6}	3.82×10^{-6}

Parentheses denote the activation energy estimated in a higher temperature region.

appear when different components (phases) are connected by a series equivalent circuit each other [90].

The relationship between the activation energy and the ionic radius of the rare-earth are shown in Fig.2-9. For the hexagonal Li series, the activation energy increases monotonically with decreasing ionic radius of rare-earth from La to Dy. For the hexagonal K series, the lowest activation energy was for K_2O-Sm_2O_3-$2SiO_2$ and increased with increasing ionic radius of rare-earth from Sm to La and with decreasing radius from Sm to Dy. For the hexagonal Rb series, the lower activation energies were for Rb_2O-RE_2O_3-$2SiO_2$ (RE=Nd,Sm,Gd), excepting Rb_2O-La_2O_3-$2SiO_2$. For the hexagonal Cs series, the lowest activation energy was for Cs_2O-Nd_2O_3-$2SiO_2$. In the hexagonal group, the lowest activation energy is observed for K_2O-RE_2O_3-$2SiO_2$.

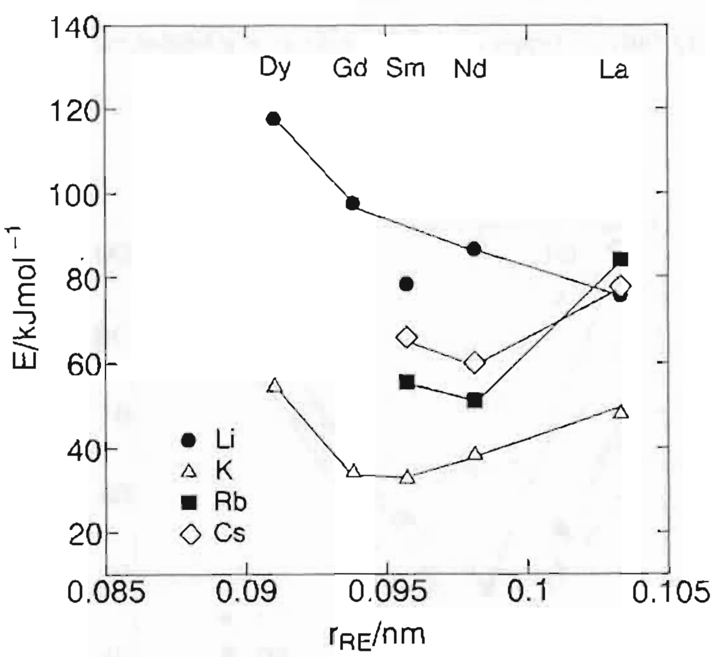

Fig. 2-9 Relationship between the ionic radius of rare-earth and the activation energy in hexagonal M_2O-RE_2O_3-$2SiO_2$.

In the hexagonal Li series, the activation energy decreased with the ionic size of rare-earth. In the hexagonal K series, as the ionic size was increased from Dy to Sm the activation energy decreased, while from Sm to La the activation energy increased.

The increase in the activation energy from Sm to La may be explained by the potassium ionic size becoming smaller than the optimum size for ionic motion. In particular, for K_2O-La_2O_3-$2SiO_2$, the a-lattice constant is considerably larger than the extrapolated values for K_2O-RE_2O_3-$2SiO_2$ (RE=Nd,Sm,Gd,Dy). For K_2O-RE_2O_3-$2SiO_2$ (RE=La,Nd,Sm,Gd,Dy), the activation energy is lower than those of M_2O-RE_2O_3-$2SiO_2$ (M=Li,Rb,Cs) as shown in Fig.2-10. In the hexagonal group, the a- and c-lattice constant for K_2O-RE_2O_3-$2SiO_2$ are larger than those for Li_2O-RE_2O_3-$2SiO_2$ and Cs_2O-RE_2O_3-$2SiO_2$ (Figs.2-3 and 2-4). These results suggest that the lowest activation energy confirmed for K_2O-RE_2O_3-$2SiO_2$ is attributed to the abnormal expansion of the a- and c-axes. The highest conductivity ($1.31 \times 10^{-2} S \cdot cm^{-1}$ at 300℃) was observed for K_2O-Nd_2O_3-$2SiO_2$ and this is almost equal to that ($1.8 \times 10^{-2} S \cdot cm^{-1}$ at 300℃) for $K_2O \cdot 5.2Fe_2O_3 \cdot 0.8ZnO$ [29].

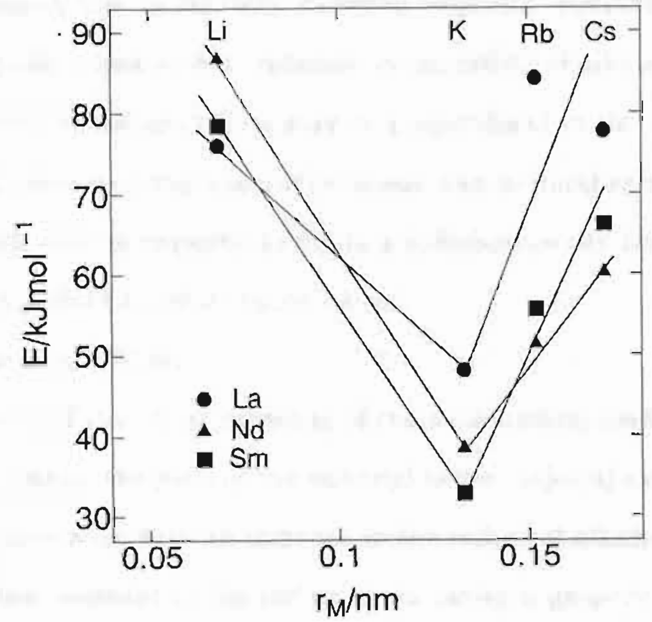

Fig. 2-10 Relationship between the ionic radius of alkali-metal and the activation energy in hexagonal M_2O-RE_2O_3-$2SiO_2$.

The ionic conductivity is apparently determined by the electrostatic interaction between the negatively charged framework (oxygen) and the mobile cations, as well as steric effects caused by the size ratio of cations and the narrowest points in the channel system. According to Anderson and Stuart's model for ionic conductivity in silica glasses, the activation energy of ionic conduction is the sum of the electrostatic energy change and the energy required to move or jump the ion from one site to another [91,92].

The electrostatic energy term in the activation energy of conduction is evaluated as the energy difference between the two configurations and the electrostatic contribution to the activation energy is represented by a relationship of the form :

$$E_B = A \cdot e^2 \cdot [(r_i + r_o)^{-1} - R^{-1}] \qquad (2\text{-}13)$$

where A is a function of the relative premittivity, r_i and r_o are the radius of the alkali-metal ion and the oxygen ion, respectively, and R is the distance between the ions when the alkali-metal ion is halfway between adjacent equilibrium sites. The electrostatic energy decreases with an increase in the radius of alkali-metal and with a decrease in the lattice constants which may be proportional to the distance, R. The energy required to move or jump the ion from one site to another may be estimated from the total elastic energy required to dilate a spherical cavity from radius r_d to r ; for an ellipsoid cavity, the energy is expressed as

$$E_S = C r_d \cdot (r - r_d)^2 \cdot E(c/a) \qquad (2\text{-}14)$$

where C is a function of the shear modulus of the surrounding medium and E(c/a) is a factor which depends on the ratio of the minor(c) to the major(a) axis of the ellipsoid. The elastic energy increases with an increase in the radius of alkali-metal and with a decrease in the lattice constant as the radius of the cavity is proportional to the lattice constant. According to Anderson and Stuart's model, it is qualitatively apparent that in a alkali-metal series with the same phase, the lowering of activation energy with increasing ionic size of rare-earth is caused by lowering of the total elastic energy ; in addition, the increase in the activation energy with increasing ionic radius of rare-earth observed for K, Rb and Cs series is attributable to the increase in the distance, R.

2-4. Summary

A series of new solid electrolytes, M_2O-RE_2O_3-$2SiO_2$ (M=Li,Na,K,Rb,Cs RE=La,Nd,Sm,Gd,Dy,Y,Ho,Er,Yb), were prepared from a mixture of $M_2CO_3 \cdot RE_2O_3 \cdot 2SiO_2$. Their crystal structures, microstructures and electrical properties have all been investigated. The results are summarized as follows :

(1) For M_2O-RE_2O_3-$2SiO_2$ (M=Li,K RE=La,Nd,Sm,Gd,Dy and M=Rb,Cs RE=La,Nd, Sm), the same hexagonal XRD pattern was confirmed. The major phase of these hexagonal samples is an apatite structure of the composition, $M_xRE_{10-x}(SiO_4)_6O_{3-x}$ (X=1-3). Glass phases and small amount of unidentified crystalline phases were also found as minor components.

(2) In each alkali-metal series, the a- and c-lattice constants of M_2O-RE_2O_3-$2SiO_2$ bearing hexagonal structure increased monotonically with an increase in the ionic radius of RE. The highest values of lattice constants, a and c, were observed for K_2O-RE_2O_3-$2SiO_2$.

(3) The hexagonal samples, especially K_2O-RE_2O_3-$2SiO_2$, showed relatively high conductivities and low activation energies. In the K_2O-RE_2O_3-$2SiO_2$, the activation energy decreased from Dy to Sm and increased from Sm to La with increasing ionic radius of rare-earth. The lowest activation and the highest conductivity at 300℃ was observed for K_2O-Sm_2O_3-$2SiO_2$ ($32.8 kJ \cdot mol^{-1}$) and K_2O-Nd_2O_3-$2SiO_2$ ($1.31 \times 10^{-2} S \cdot cm^{-1}$), respectively. This conductivity is comparable to that of $K_2O \cdot 5.2Fe_2O_3 \cdot 0.8ZnO$.

Chapter 3

Morphology and ionic conductivity of potassium-samarium-silicates, K_2O-Sm_2O_3-$nSiO_2$ (n=1-14)

3-1. Introduction

In chapter 2, the electrical properties of some alkali-metal rare-earth silicates, M_2O-RE_2O_3-$2SiO_2$ (M=Li,Na,K,Rb,Cs RE=La,Nd,Sm,Gd,Dy,Y,Ho,Er,Yb), were investigated and a compact alkali-metal ion solid electrolyte with high conductivity was developed. M_2O-RE_2O_3-$2SiO_2$ (M=Li,K,Rb,Cs RE=La,Nd,Sm,Gd,Dy) which consist of the major phase with the hexagonal apatite structure was found to be the most suitable alkali-metal ion solid electrolyte with the high conductivity and the low activation energy. K_2O-Nd_2O_3-$2SiO_2$ showed the highest ionic conductivity and K_2O-Sm_2O_3-$2SiO_2$ had the lowest activation energy. However, both these materials have the disadvantage that they are not stable upon exposure of water or moisture.

In this chapter, the relationship between the electrical properties and water-resistance and the silica (SiO_2) content in K_2O-Sm_2O_3-$nSiO_2$ (n=1-14) has been investigated.

3-2. Experimental

3-2-1. Samples

Discs of potassium rare-earth silicates, K_2O-RE_2O_3-$nSiO_2$ (RE=La,Nd,Sm, Gd,Dy n=1-14), obtained by sintering of $K_2CO_3 \cdot RE_2O_3 \cdot nSiO_2$ mixtures were prepared according to the procedure described in section 2-2-1. K_2O-Sm_2O_3-$2SiO_2$ was sintered at 1350℃ for 10h. Other samples were sintered for 3h at the temperatures given in Table 3-1. Part of the prepared disc was pulverized with ethanol by a planet type ball-mill. The resultant powders were treated with water and ultrasonic irradiation and then dried, discs were again prepared at 100MPa and sintered in air for 3h at the temperatures given in Table 3-1. Hereafter, water-treated samples are abbreviated as K_2O-RE_2O_3-$nSiO_2$(W).

Table 3-1 Crystal parameters and sintering temperature

	lattice constant a/nm	lattice constant c/nm	sintering temp. / °C
K_2O-Sm_2O_3-$1SiO_2$			1600
K_2O-Sm_2O_3-$2SiO_2$	0.9484	0.7002	1350
K_2O-Sm_2O_3-$2SiO_2$(W)	0.9511	0.6997	1150
K_2O-Sm_2O_3-$3SiO_2$	0.9511	0.7012	1200
K_2O-Sm_2O_3-$4SiO_2$	0.9512	0.7006	1050
K_2O-Sm_2O_3-$4SiO_2$(W)	0.9506	0.7000	1050
K_2O-Sm_2O_3-$6SiO_2$	0.9511	0.6998	950
K_2O-Sm_2O_3-$6SiO_2$(W)	0.9511	0.6994	950
K_2O-Sm_2O_3-$7SiO_2$	0.9511	0.6996	950
K_2O-Sm_2O_3-$8SiO_2$	0.9509	0.6998	950
K_2O-Sm_2O_3-$8SiO_2$(W)	0.9530	0.6983	950
K_2O-Sm_2O_3-$10SiO_2$	0.9509	0.6990	950
K_2O-Sm_2O_3-$10SiO_2$(W)	0.9508	0.6986	950
K_2O-Sm_2O_3-$12SiO_2$	0.9509	0.6983	1000
K_2O-Sm_2O_3-$14SiO_2$	0.9505	0.6985	1000
K_2O-La_2O_3-$2SiO_2$	0.9708	0.7244	1350
K_2O-La_2O_3-$2SiO_2$(W)	0.9709	0.7240	1150
K_2O-Nd_2O_3-$2SiO_2$	0.9562	0.7089	1350
K_2O-Nd_2O_3-$2SiO_2$(W)	0.9568	0.7085	1150
K_2O-Gd_2O_3-$2SiO_2$	0.9434	0.6934	1350
K_2O-Gd_2O_3-$2SiO_2$(W)	0.9453	0.6941	1150
K_2O-Dy_2O_3-$2SiO_2$	0.9371	0.6851	1350
K_2O-La_2O_3-$6SiO_2$	0.9608	0.7272	950
K_2O-La_2O_3-$6SiO_2$(W)	0.9604	0.7253	950
K_2O-Nd_2O_3-$6SiO_2$	0.9596	0.7098	950
K_2O-Nd_2O_3-$6SiO_2$(W)	0.9588	0.7088	950
K_2O-Gd_2O_3-$6SiO_2$	0.9479	0.6920	950
K_2O-Gd_2O_3-$6SiO_2$(W)	0.9460	0.6916	950
K_2O-Dy_2O_3-$6SiO_2$	0.9413	0.6829	950
K_2O-Dy_2O_3-$6SiO_2$(W)	0.9406	0.6825	950

(W) : sintered sample using powder treated with water.

3-2-2. Measurements

The microstructures were examined using a scanning electron microscopy (Hitachi, X-560). The other measurements were carried out by the methods described in section 2-2-2.

3-3. Results and discussion

3-3-1. Crystal structure

The XRD patterns of K_2O-Sm_2O_3-$nSiO_2$ (n=2-14) were very similar to that of hexagonal $LiLa_9(SiO_4)_6O_2$ (JCPDS file no.32-657), the lattice constants were however slightly different. The halo of XRD pattern becomes more intense, conversely the intensities of the XRD peaks reduces, as the SiO_2 content increases. This is due to an increase in the proportion of the glass phase. The XRD patters of K_2O-RE_2O_3-$6SiO_2$ (RE=La,Nd,Gd,Dy) were very similar to those of K_2O-Sm_2O_3-$nSiO_2$ (n=2-14). The K_2O-Sm_2O_3-$nSiO_2$ (n=2-14) and K_2O-RE_2O_3-$6SiO_2$ (RE=La,Nd,Gd,Dy) consist of the major phase with the hexagonal apatite structure and the glass phases as alkali-metal silicates and unassignable crystalline phase are present as minor components. The estimated lattice constants are summarized in Table 3-1. For K_2O-Sm_2O_3-SiO_2, the XRD results could not be assigned to the hexagonal phase. In the K_2O-RE_2O_3-$6SiO_2$ (RE=La,Nd,Sm,Gd,Dy) series, the lattice constants, a and c, increase monotonically with an increase in the ionic radius of rare-earth. The XRD patterns of water-treated samples were similar to those of samples before water-treatment. The lattice constants are summarized in Table 3-1. Both a- and c-parameters are not significantly affected by water-treatment. Furthermore, the lattice constants of K_2O-RE_2O_3-$2SiO_2$(W) and K_2O-RE_2O_3-$6SiO_2$(W) monotonically increase with increasing ionic radius of rare-earth.

3-3-2. X-ray fluorescence analysis

Elemental analysis of potassium (K), rare-earth (RE) and silicon (Si) was determined before and after water-treatment by the X-ray fluorescence method. The intensity ratios of I(K)/I(RE), I(K)/I(Si) and I(RE)/I(Si) before and after treatment with water are summarized in Table 3-2. The ratios of I(K)/I(RE) and I(K)/I(Si) decrease after water-treatment, the elution of potassium by water was lower for samples containing higher SiO_2 for K_2O-Sm_2O_3-nSiO_2 (n=2-10), and the I(RE)/I(Si) value remained either constant or increased slightly. The elution of potassium by water was particularly suppressed in n≧6. For K_2O-RE_2O_3-6SiO_2 (RE=La,Nd,Sm,Gd,Dy), the elution of potassium by water decreases with decreasing ionic radius of rare-earth.

Table 3-2 X-ray fluorescence data of K_2O-RE_2O_3-nSiO_2

	I(K)/I(RE)	I(K)/I(Si)	I(RE)/I(Si)
K_2O-Sm_2O_3-2SiO_2	1.010	2.637	2.611
K_2O-Sm_2O_3-2SiO_2(W)	0.228	0.675	2.967
K_2O-Sm_2O_3-4SiO_2	1.066	1.348	1.264
K_2O-Sm_2O_3-4SiO_2(W)	0.634	0.923	1.456
K_2O-Sm_2O_3-6SiO_2	1.023	0.840	0.821
K_2O-Sm_2O_3-6SiO_2(W)	0.873	0.789	0.903
K_2O-Sm_2O_3-8SiO_2	0.974	0.620	0.637
K_2O-Sm_2O_3-8SiO_2(W)	0.868	0.565	0.651
K_2O-Sm_2O_3-10SiO_2	0.942	0.471	0.500
K_2O-Sm_2O_3-10SiO_2(W)	0.838	0.427	0.510
K_2O-La_2O_3-2SiO_2	2.936	2.060	0.702
K_2O-La_2O_3-2SiO_2(W)	0.868	0.714	0.804
K_2O-Nd_2O_3-2SiO_2	1.313	2.114	1.610
K_2O-Nd_2O_3-2SiO_2(W)	0.396	0.695	1.757
K_2O-Gd_2O_3-2SiO_2	0.610	2.291	3.745
K_2O-Gd_2O_3-2SiO_2(W)	0.267	1.081	4.065
K_2O-La_2O_3-6SiO_2	3.529	0.819	0.232
K_2O-La_2O_3-6SiO_2(W)	2.712	0.666	0.245
K_2O-Nd_2O_3-6SiO_2	1.648	0.832	0.505
K_2O-Nd_2O_3-6SiO_2(W)	1.359	0.724	0.533
K_2O-Gd_2O_3-6SiO_2	0.675	0.821	1.217
K_2O-Gd_2O_3-6SiO_2(W)	0.591	0.731	1.238
K_2O-Dy_2O_3-6SiO_2	0.460	0.797	1.733
K_2O-Dy_2O_3-6SiO_2(W)	0.410	0.719	1.754

(W) : sintered sample using powder treated with water.

3-3-3. Microstructure

Figure 3-1 shows the microstructures on the fracture surface of K_2O-Sm_2O_3-$nSiO_2$ (n=1-14), the water treated K_2O-Sm_2O_3-$nSiO_2$ and K_2O-RE_2O_3-$6SiO_2$ (RE=La,Nd,Gd,Dy). Interfusion was well progressed and the crystal particles were hardly detected, except in the case of n=2. The morphology of K_2O-Sm_2O_3-SiO_2 was distinctly different from that of the others. For samples with a high SiO_2 content (n>4), well defined fine particles were not observed, and densification was well progressed. It is clear that crystalline phases are dispersed within glass-like phases and that dense glass ceramic composites are formed. The morphology of K_2O-RE_2O_3-$6SiO_2$ (RE=La,Nd,Gd,Dy) was similar to that of K_2O-Sm_2O_3-$6SiO_2$. For the K_2O-Sm_2O_3-$nSiO_2$ with n>2 series, the fracture surface of the water treated ceramics is smoother than that of the untreated samples, and the grain boundary is unclear. The microstructure on the fracture surface of the water-treated K_2O-Sm_2O_3-$2SiO_2$ is fairly different from that of the untreated sample. Such microstructural change may be attributed to the lowering of potassium ion by water-treatment.

3-3-4. Electrical properties

In order to determine the conductivity component, complex-plane impedance analysis was performed. In the lower temperature region, the result for samples of $n \geqq 4$ was represented by a slightly depressed semicircle in the higher frequency region and had a spur in the lower frequency region as shown in Fig.3-2. The semicircle corresponds probably to the grain boundary component. When the temperature was increased, the semicircle diminished and only a spur, probably due to the electrolyte-electrode behavior, was observed. The intercept with the Z'-axis gives the total resistance of the electrolyte. A depressed semicircle appearing in the high frequency region in the complex impedance plot can be adequately expressed by equation (3-1) :

$$Z(\omega) = Z_0 / (1 + (j\,\omega/\omega_0)^{1-\alpha} \tag{3-1}$$

where $Z(\omega)$ is the complex impedance at angular frequency ω, Z_0 is the real-axis

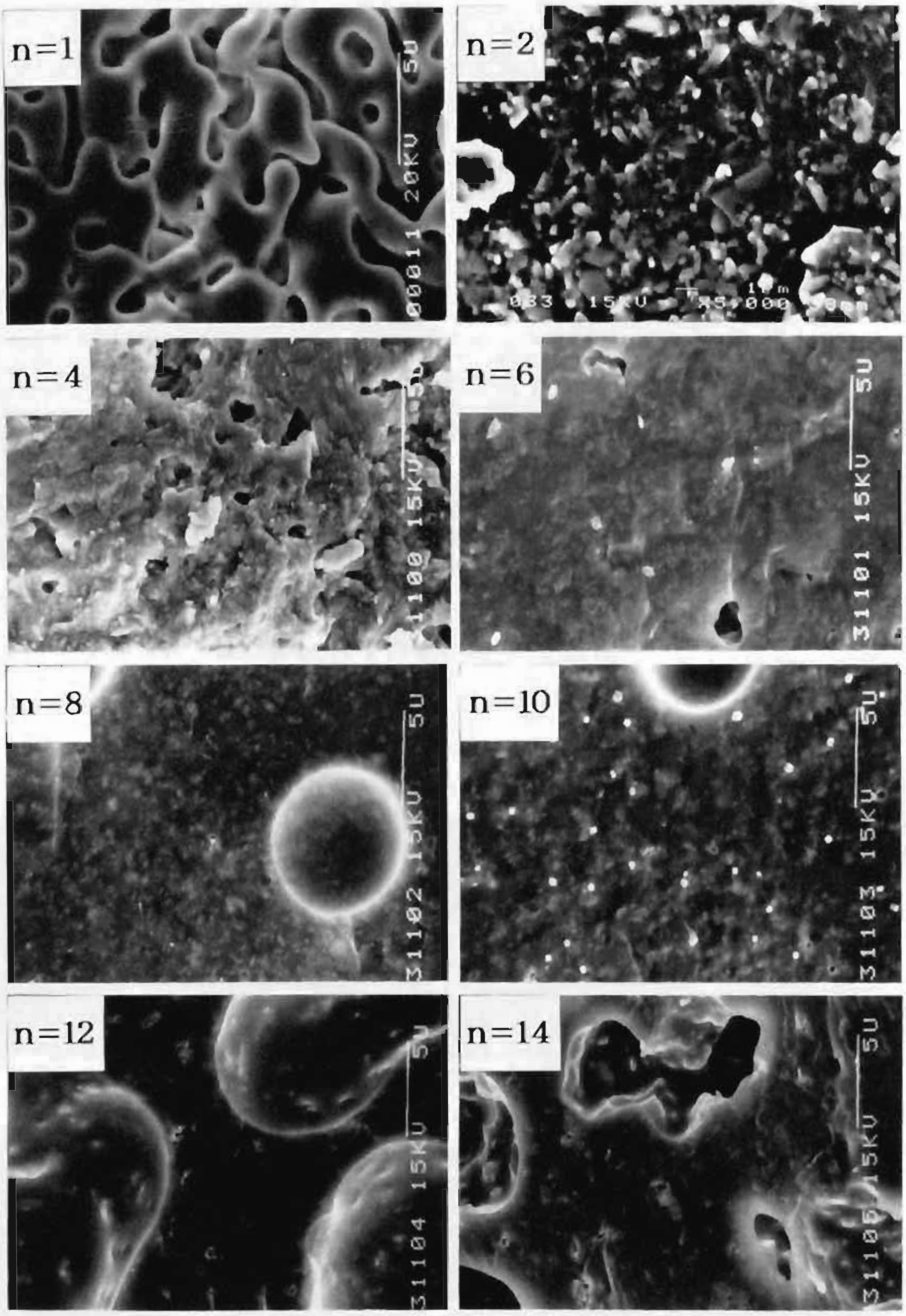

Fig. 3-1(a) Scanning electron micrographs of fracture surface of K_2O-Sm_2O_3-$nSiO_2$.

5 μm

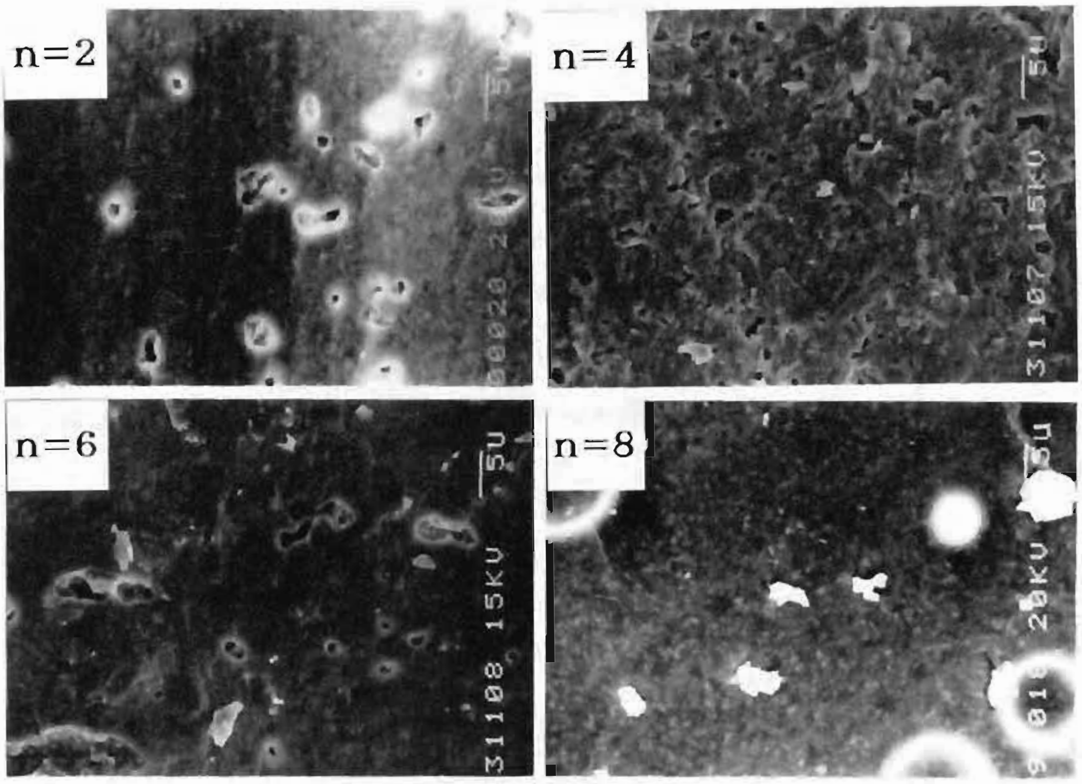

Fig. 3-1(b) Scanning electron micrographs of fracture surface of K_2O-Sm_2O_3-$nSiO_2$(W) after treatment with water.

10 μm

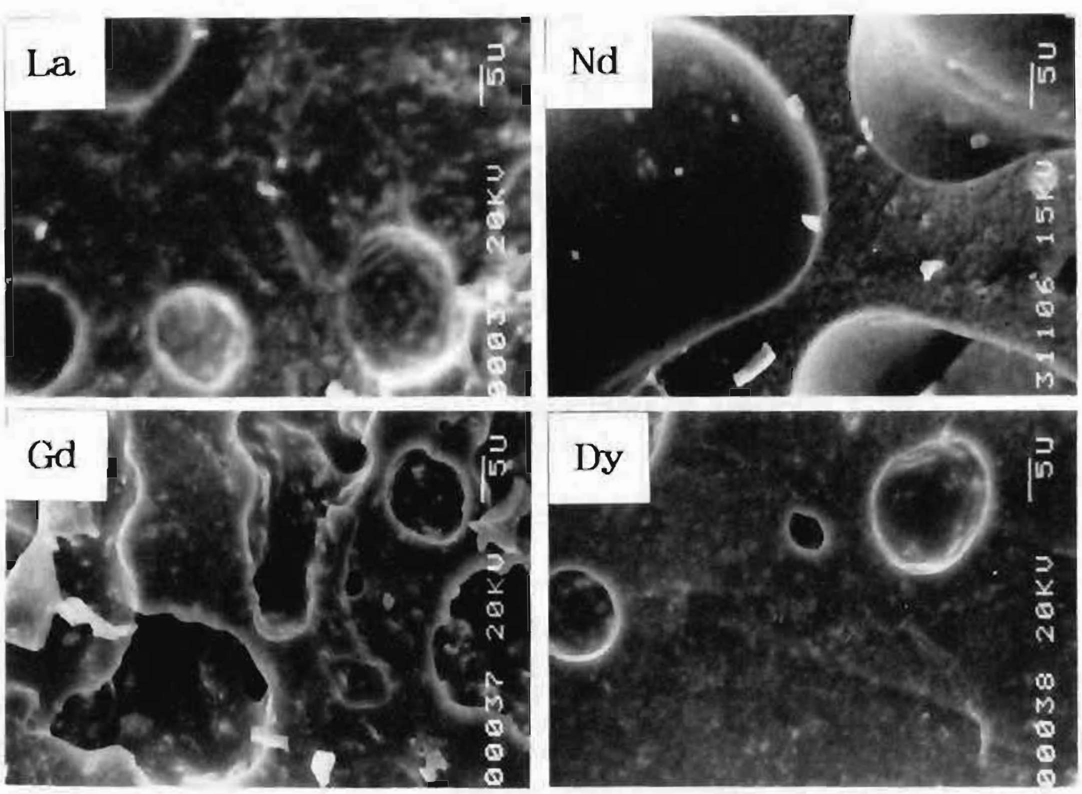

Fig. 3-1(c) Scanning electron micrographs of fracture surface of K_2O-RE_2O_3-$6SiO_2$.

10 μm

intercept in the low frequency, ω_0 is the relaxation angular frequency at the maximum height of the semicircle, α is the depression parameter ($\theta = \pi\alpha/2$) and $j=(-1)^{1/2}$. The equivalent circuit corresponding to the impedance spectrum consists of a frequency dependent capacitor $Cp(\omega)$ and a frequency independent resistor Rp. These parameters are described by the following equations :

$$Z_0 = Rp \tag{3-2}$$

$$Cp(\omega) = C_0 \cdot (j\,\omega/\omega_0)^{-\alpha} \tag{3-3}$$

$$Rp \cdot C_0 \cdot \omega_0 = 1 \tag{3-4}$$

The limiting case, $\theta=0$, represents an equivalent circuit consisting of lumped RC components with zero depression angle.

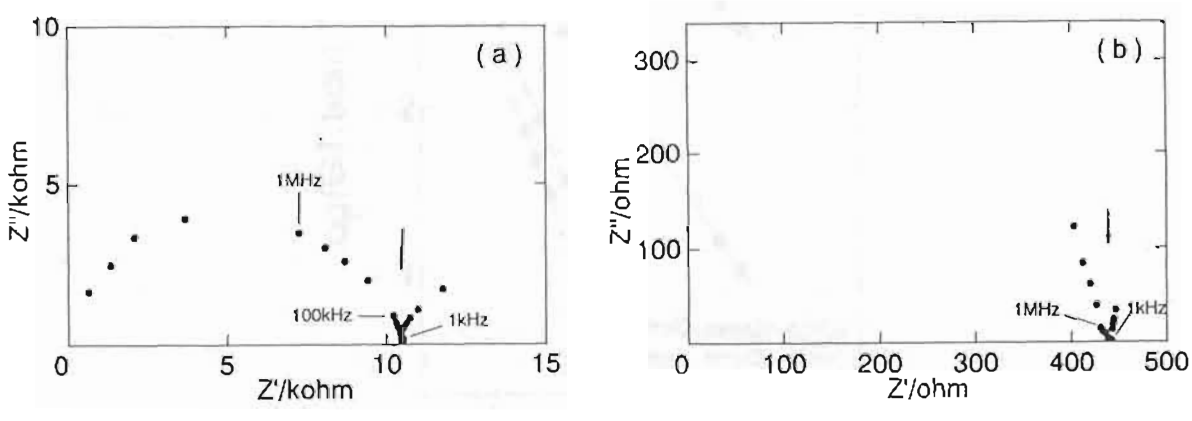

Fig. 3-2 Complex impedance plots of K_2O-Sm_2O_3-$4SiO_2$: (a) at 300°C, (b) at 600°C.

It has been confirmed, for samples of $n \geqq 4$, that the depression angle decreases with an increase in the resistance (the resistance increases with the SiO_2 content except for n=1) and that the ω_0 value increases with increasing temperature. Graphically estimated resistances from the complex plane impedance results were parameterized by the Arrhenius equation,

$$G \cdot T = G_0 \cdot \exp(-E/kT) \tag{2-12}$$

Arrhenius plots are shown in Fig.3-3. The electrical parameters are summarized in Table 3-3. For K_2O-RE_2O_3-$nSiO_2$ (RE=La,Nd,Sm,Gd,Dy n=1-14), the complex impedance analyses suggested that the electrical properties may be mainly dependent on the bulk component (probably the major phase) when n is 2 or 3, whereas those may be mainly dependent on the grain boundary component (probably the glass phase) when n is $\geqq 4$.

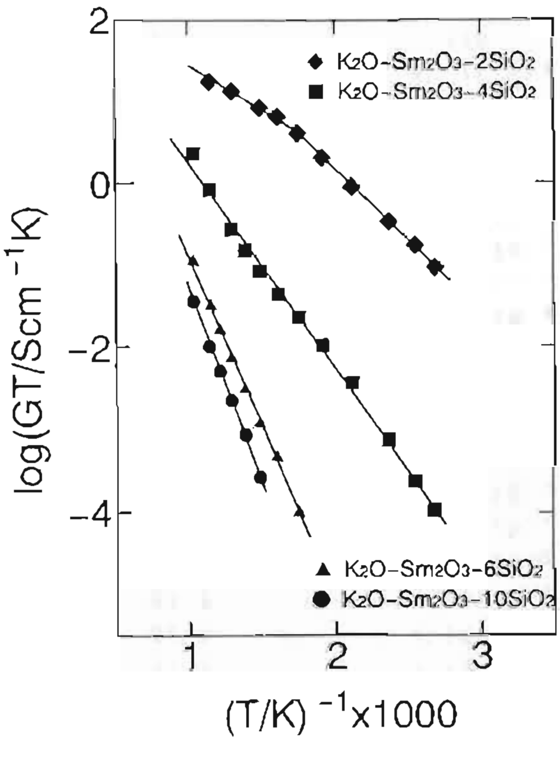

Fig. 3-3 Arrhenius plots.

The highest conductivity and lowest activation energy were observed for K_2O-Sm_2O_3-$2SiO_2$, and the conductivity decreases with increasing SiO_2 content. K_2O-Sm_2O_3-SiO_2 shows low conductivity behavior. For K_2O-Sm_2O_3-$nSiO_2$ (n=2-4), the conductivity decreased and the activation energy increased after water-treatment, while for the samples with higher SiO_2 content (n>4), the electrical properties were only slightly influenced by water-treatment. The lesser elution of potassium is confirmed with increasing SiO_2 content as mentioned in section 3-3-2. The relationship between the electrical parameters, E and G_0, and I(K)/I(Si) is shown

Table 3-3 Electrical parameters

	activation energy /kJ•mol^{-1}	conductivity/S•cm^{-1} 500°C	600°C
$K_2O-Sm_2O_3-1SiO_2$	161	$<10^{-8}$	$<10^{-8}$
$K_2O-Sm_2O_3-2SiO_2$	32.8 (18.0)	1.71×10^{-2}	2.00×10^{-2}
$K_2O-Sm_2O_3-2SiO_2$ (W)	70.1	1.80×10^{-6}	5.81×10^{-5}
$K_2O-Sm_2O_3-3SiO_2$	39.9 (20.9)	3.95×10^{-2}	5.07×10^{-2}
$K_2O-Sm_2O_3-4SiO_2$	50.6 (42.9)	3.52×10^{-4}	9.46×10^{-4}
$K_2O-Sm_2O_3-4SiO_2$ (W)	77.8	8.72×10^{-6}	3.10×10^{-5}
$K_2O-Sm_2O_3-6SiO_2$	79.7	9.28×10^{-6}	3.61×10^{-5}
$K_2O-Sm_2O_3-6SiO_2$ (W)	84.0	7.71×10^{-6}	3.10×10^{-5}
$K_2O-Sm_2O_3-7SiO_2$	86.1	8.20×10^{-6}	3.17×10^{-5}
$K_2O-Sm_2O_3-8SiO_2$	87.4	3.96×10^{-6}	1.64×10^{-5}
$K_2O-Sm_2O_3-8SiO_2$ (W)	85.5	3.09×10^{-6}	1.30×10^{-5}
$K_2O-Sm_2O_3-10SiO_2$	89.5	2.80×10^{-6}	1.16×10^{-5}
$K_2O-Sm_2O_3-10SiO_2$ (W)	88.7	2.27×10^{-6}	9.74×10^{-6}
$K_2O-Sm_2O_3-12SiO_2$	104.9	1.02×10^{-6}	4.90×10^{-6}
$K_2O-Sm_2O_3-14SiO_2$	94.9	6.57×10^{-7}	2.99×10^{-6}
$K_2O-La_2O_3-6SiO_2$	82.6	7.74×10^{-6}	2.82×10^{-5}
$K_2O-La_2O_3-6SiO_2$ (W)	80.3	8.21×10^{-6}	3.03×10^{-5}
$K_2O-Nd_2O_3-6SiO_2$	80.0	4.12×10^{-6}	1.49×10^{-5}
$K_2O-Nd_2O_3-6SiO_2$ (W)	82.6	5.66×10^{-6}	2.23×10^{-5}
$K_2O-Gd_2O_3-6SiO_2$	81.3	4.02×10^{-6}	1.55×10^{-5}
$K_2O-Gd_2O_3-6SiO_2$ (W)	81.3	4.74×10^{-6}	1.89×10^{-5}
$K_2O-Dy_2O_3-6SiO_2$	82.2	8.82×10^{-6}	3.42×10^{-5}
$K_2O-Dy_2O_3-6SiO_2$ (W)	83.0	7.07×10^{-6}	2.77×10^{-5}

(W) : sintered sample using powder treated with water,
Parentheses denote the activation energy estimated in a higher temperature region.

in Fig.3-4. It appears that the activation energy and the pre-exponential factor are well correlated to the concentration of potassium, though the scatter in the data is significant.

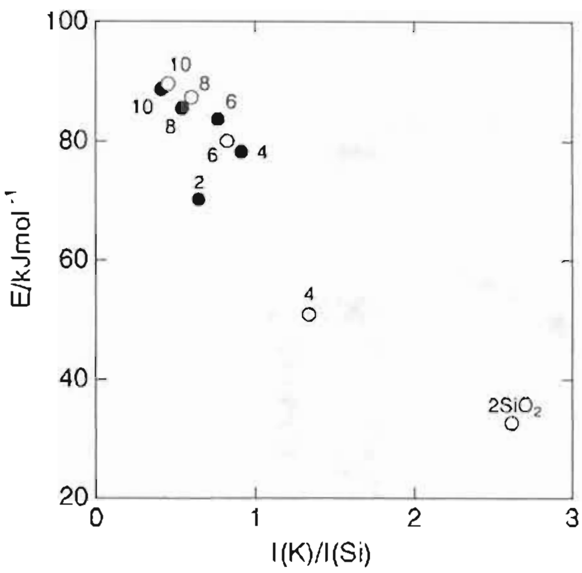

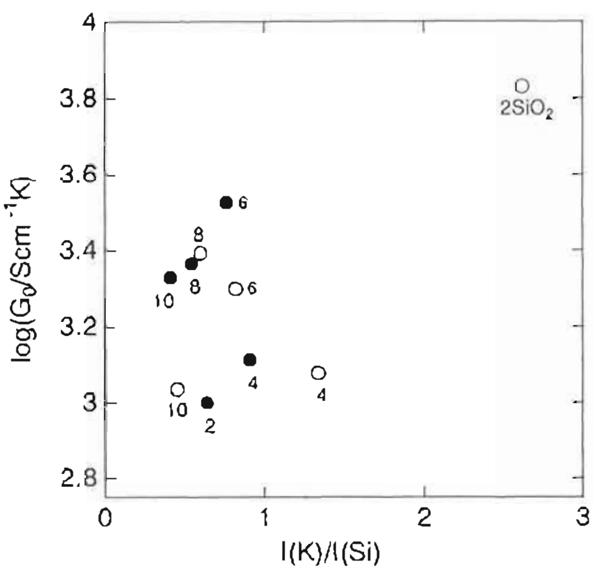

Fig. 3-4 Relationship between the electrical parameters and I(K)/I(Si) : (○) prepared samples, (●) sintered samples using powders treated with water, n value in K_2O-Sm_2O_3-nSiO_2 is shown in the figure.

Based on the Anderson and Stuart's model explained in section 2-3-5, Hakim and Uhlmann have estimated the activation energy of ionic conduction in alkali-metal silicate glasses [92]. Calculated activation energies as a function of alkali-metal concentration, assuming the jump distance is the average inter-ionic separation in the glass, are given in Fig.3-5. The estimated activation energies of the K_2O-Sm_2O_3-nSiO_2 (n=2-14) are also shown in the figure. For the K_2O-Sm_2O_3-nSiO_2, the potassium contents shown in the figure are those in the starting mixtures. When the potassium content is less than approximately 10mol%, the activation energy of K_2O-Sm_2O_3-nSiO_2 (n>6) agrees reasonably with the results obtained by Hakim and Uhlmann for potassium-metal silicate glasses (K_2O-SiO_2 prepared by melting at 1550℃ in air). It appears that the increase of the activation energy by water-treatment is attributable to the decrease in potassium content. To confirm this interpretation, the correlation between the activation energy and X-ray fluorescence results, I(K)/I(Si), was examined.

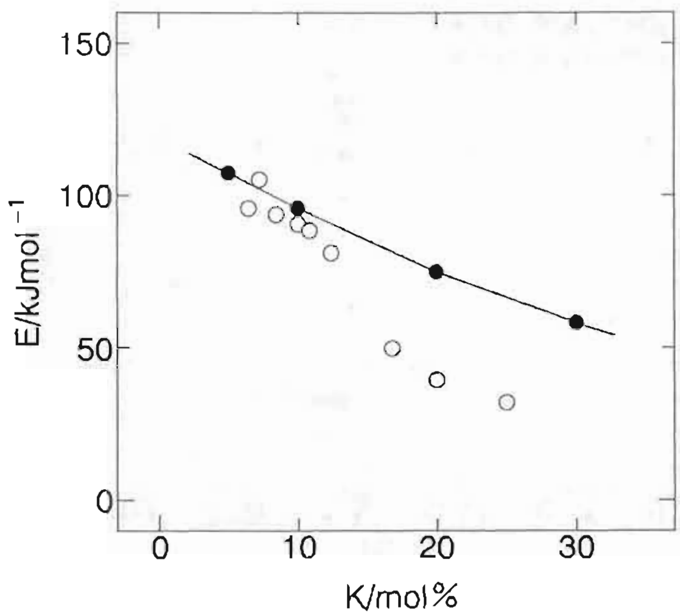

Fig. 3-5 Relationship between the activation energy and the potassium content : (○) K_2O-Sm_2O_3-$nSiO_2$, (●) potassium silicate glasses reported by Hakim and Uhlmann [92].

It was confirmed that the activation energy changes due to the water-treatment correlated well with the X-ray fluorescence results. From these results, it is concluded that activation energy changes due to composition can be interpreted in terms of Anderson and Stuart's model for glass. The activation energy increases with increasing potassium content and/or potassium site separation in the glass phase for samples having a potassium content of less than about 10mol%.

As shown in Fig.3-6, the activation energy of K_2O-RE_2O_3-$2SiO_2$ (RE=La,Nd,Sm, Gd,Dy) decreases with increasing ionic radius of rare-earth from Dy to Sm, and increases with increasing radius from Sm to La. The highest conductivity and lowest activation energy were confirmed when samarium was used for K_2O-RE_2O_3-$2SiO_2$.

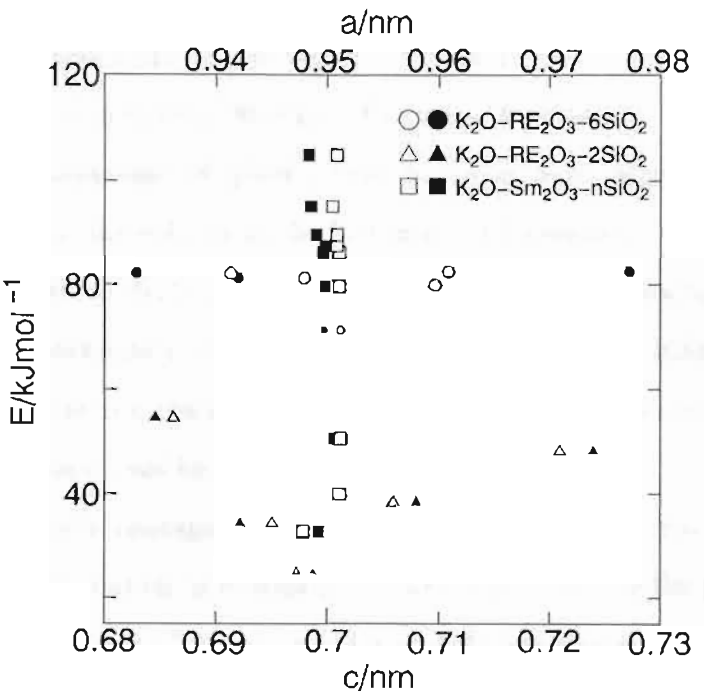

Fig. 3-6 Relationship between the activation energy and the lattice parameters : (open symbols) E vs. a-lattice constant, (closed symbols) E vs. c-lattice constant.

A similar dependence was also confirmed for K_2O-RE_2O_3-$6SiO_2$ (RE=La,Nd,Sm,Gd,Dy). The effects of the ionic radius of rare-earth on the activation energy decrease with increasing SiO_2 content.

3-4. Summary

New solid electrolytes, K_2O-RE_2O_3-$nSiO_2$ (RE=La,Nd,Sm,Gd,Dy n=1-14), have been prepared, and their water-resistance investigated by the determination of crystal structures and microstructures and by the measurements of electrical properties after water-treatment. Results obtained are summarized as follows :

(1) The major phase was the hexagonal apatite structure both before and after water-treatment excepting n=1. There was not a large difference between the lattice constants (a and c) of the samples before and after water-treatment. The halo of XRD pattern due to the formation of glass phase becomes more significant and the intensities of the XRD peaks reduces as the SiO_2 content increases.

(2) The amount of potassium eluted by water decreased with increasing SiO_2 content and then was approximately constant at $n \geqq 6$. In the K_2O-RE_2O_3-$6SiO_2$ (RE=La,Nd,Sm,Gd,Dy) series, the decrease in the ionic radius of rare-earth decreased the amount of potassium eluted by water.

(3) For the high SiO_2 containing (n>4) sample, the crystal grains were not recognizable, suggesting that these crystal grains are surrounded by the glass phase to give a dense ceramic composite. When samples of n>2 were treated with water, these microstructure became increasingly smooth and the grain boundary became unclear.

(4) The conductivity decreased with increasing SiO_2 content except in the case of n=1. For n=2 and 4, the conductivity markedly decreased on water-treatment and the activation energy increased. Conversely, the electrical properties of the samples of n>4 were little influenced by water-treatment.

Chapter 4

Ionic conductivity of the rare-earth silicate, $RE_{10}Si_6O_{27}$ (RE=La,Nd,Sm,Gd,Dy,Y,Ho,Er,Yb)

4-1. Introduction

One of the most important ceramic electrolytes is stabilized zirconia, which is well known as an oxygen conducting electrolyte. Such dense stabilized zirconia is very useful and has already been commercialized as an oxygen sensor to control the air/fuel ratio in automobile engine's and to measure oxygen concentration in molten metals [48,49]. In chapters 2 and 3, it was concluded that the alkali-metal rare-earth silicates, $M_2O{\cdot}RE_2O_3{\cdot}2SiO_2$ (M=Li,K for RE=La,Nd,Sm,Gd,Dy and M=Rb,Cs for RE=La,Nd,Sm) are the excellent alkali-metal conductors and those bear a hexagonal apatite structure as the major phase. The composition of apatite structure can be expressed as $M_XRE_{10\text{-}X}(SiO_4)_6O_{3\text{-}X}$ (X=1-3). In the case of M=Li, it has been proposed that the rare-earth atoms are located on the 4f and 6h sites and the lithium atom on the 4f site. It was found that the rare-earth silicates, $RE_{10}Si_6O_{27}$, obtained by substituting RE for all of M in $M_XRE_{10\text{-}X}(SiO_4)_6O_{3\text{-}X}$, show the relatively high conductivities, despite that the composition of apatite structure is no longer maintained. These can be regarded as oxygen ionic conductors.

In this chapter, the author has investigated the conductivities of rare-earth silicates in order to develop a new ionic conductor.

4-2. Experimental

4-2-1. Samples

Discs of rare-earth silicates, $RE_{10}Si_6O_{27}$ (RE=La,Nd,Sm,Gd,Dy,Y,Ho,Er,Yb), $Nd_XSi_6O_{12+1.5X}$ (X=6-12) and $M(II)_XNd_{10\text{-}X}Si_6O_{27\text{-}0.5X}$ (M(II)=Sr,Ba ; X=2-5), were according to the procedure described in section 2-2-1. The samples were sintered for 2h at the temperature given in Table 4-1.

4-2-2. Measurements

The crystal structures were determined at room temperature by powder X-ray diffraction (Rigaku, Rint-2500V). Other measurements were carried out by the methods described in section 2-2-2.

Table 4-1 Crystal parameters, phase and sintering temperature

	lattice constant			β /		sintering
	a/nm	b/nm	c/nm	degree	phase*	temp. / °C
$La_{10}Si_6O_{27}$	0.9762		0.7204		H	1550
$Nd_{10}Si_6O_{27}$	0.9610		0.7044		H	1550
$Sm_{10}Si_6O_{27}$	0.9541		0.6954		H	1550
$Gd_{10}Si_6O_{27}$	0.9494		0.6888		H	1550
$Dy_{10}Si_6O_{27}$	0.9415		0.6795		H	1575
$Y_{10}Si_6O_{27}$	1.2571	0.6750	1.0451	102.59	M	1600
$Ho_{10}Si_6O_{27}$	1.2267	0.6750	1.0463	101.81	M	1600
$Er_{10}Si_6O_{27}$	1.2519	0.6728	1.0401	102.52	M	1600
$Yb_{10}Si_6O_{27}$	1.2445	0.6686	1.0321	102.61	M	1600
$Nd_4Si_6O_{18}$	0.6762		2.4609		T	1375
$Nd_5Si_6O_{19.5}$	0.6756		2.4596		T	1425
$Nd_6Si_6O_{21}$	0.6764		2.4606		T	1425
$Nd_7Si_6O_{22.5}$	0.9605		0.7047		H	1425
$Nd_8Si_6O_{24}$	0.9613		0.7049		H	1500
$Nd_9Si_6O_{25.5}$	0.9712		0.7048		H	1500
$Nd_{9.33}Si_6O_{26}$	0.9590		0.7039		H	1600
$Nd_{11}Si_6O_{28.5}$	0.9648		0.7039		H+M	1600
	0.9271	0.7237	0.6902	108.27		
$Nd_{12}Si_6O_{30}$	0.9271	0.7237	0.6902	108.26	M	1600
$Sr_2Nd_8Si_6O_{26}$	0.9610		0.7126		H	1600
$Ba_2Nd_8Si_6O_{26}$	0.9703		0.7202		H	1550
$Ba_4Nd_6Si_6O_{25}$	0.9718		0.7201		H	1550
$Ba_5Nd_5Si_6O_{24}$					U	1350

* H : hexagonal, M : monoclinic b axis, T : tetragonal,
U : unknown mixture.

4-3. Results and discussion

4-3-1. Crystal structure

The XRD pattern of $RE_{10}Si_6O_{27}$ (RE=La,Nd,Sm,Gd,Dy) was similar to that of $Gd_{9.33}(SiO_4)_6O_2$ (JCPDS file no.38-283, hexagonal, P63/m(176), a=0.94264nm, c=0.68444nm) and $LiLa_9(SiO_4)_6O_2$ (JCPDS file no.32-567). In the range $20^\circ \leqq 2\theta \leqq 50^\circ$, most of the observed peaks can be assigned as summarized in Table 4-2. The major phase of $RE_{10}Si_6O_{27}$ (RE=La,Nd,Sm,Gd,Dy) is the apatite structure of composition, $RE_{9.33}\square_{0.67}(SiO_4)_6O_2$. Other very weak peaks can be assigned to those of RE_2SiO_5. Based on the structure of Li_2O-RE_2O_3-$2SiO_2$ in Fig.2-5, the crystal structure of the major phase of $RE_{10}Si_6O_{27}$ (RE=La,Nd,Sm,Gd,Dy) can be proposed as shown in Fig.4-1. The oxygen ions of 2a-site are surrounded by six RE ions. It is suggested that the oxygen ion can migrate along these cavities, i.e., the material is an oxygen ionic conductor. On the other hand, the XRD patterns of

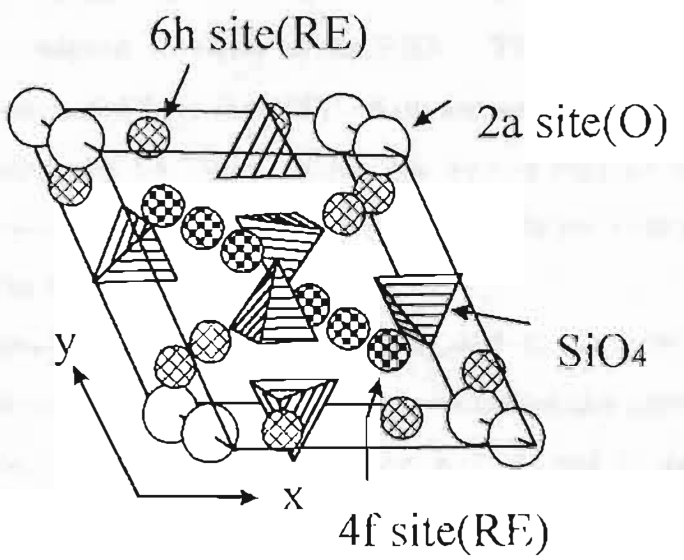

Fig. 4-1 Hexagonal apatite structure proposed to the major phase of $RE_{10}Si_6O_{27}$.

Table 4-2 XRD pattern of $La_{10}Si_6O_{27}$

h k l*	d/nm	I/I_0x100	h k l*	d/nm	I/I_0x100
2 0 0	.4231	26	2 2 1	.2309	5
1 1 1	.4048	22	3 1 1	.2217	7
0 0 2	.3607	16	3 0 2	.2197	3
1 0 2	.3316	38	1 1 3	.2153	10
2 1 0	.3195	39	4 0 0	.2110	5
2 1 1	.2919	100	2 2 2	.2018	25
1 1 2	.2897	51	3 1 2	.1963	14
3 0 0	.2815	28	2 1 3	.1918	29
2 0 2	.2741	4	3 2 1	.1870	13
2 1 2	.2388	2	4 1 0	.1841	21
3 1 0	.2341	7	4 0 2	.1820	22

* JCPDS file no. 38-283, $Gd_{9.33}(SiO_4)_6O_2$, hexagonal, P63/m(176), a=0.94264nm, c=0.68444nm.

$RE_{10}Si_6O_{27}$ (RE=Y,Ho,Er,Yb) are similar to that of Y_2SiO_5 (JCPDS File no.36-1476, monoclinic b axis, I2/a(15), a=1.25013nm, b=0.67282nm, c=0.67282nm, β=102.682°). Other peaks can assigned to those of $RE_2Si_2O_7$. The lattice constants of the $RE_{10}Si_6O_{27}$ series estimated from the JCPDS data are summarized in Table 4-1. In the $RE_{10}Si_6O_{27}$ (RE=La,Nd,Sm,Gd,Dy) series, the a- and c-lattice constants of the hexagonal phase increase monotonically with an increase in the ionic radius of RE, as can be seen from Fig.4-2.

In the $Nd_XSi_6O_{12+1.5X}$ series, a tetragonal phase ($Nd_2Si_2O_7$: JCPDS File no.22-1177, tetragonal, P41(76), a=0.6741nm, c=0.2452nm)was confirmed as a major phase for X=6, a hexagonal phase (the apatite structure) for X=7-11, and a monoclinic phase (Nd_2SiO_5 : JCPDS File no.40-284, monoclinic b axis, I2/a(15), a=0.9228nm, b=0.7282nm, c=0.6874nm, β=108.19°) for X=11 and 12. The hexagonal and monoclinic phase was formed as a by-product for X=11. Although compositions of $Nd_XSi_6O_{12+1.5X}$ agreed with that of a hexagonal apatite structure ($Nd_X(SiO_4)_6O_{1.5X-12}$) when X is in the range of 8 to 9.33, very weak peaks assignable to Nd_2SiO_5 were observed in their XRD patterns, indicating that these samples are not also a single phase. In the hexagonal samples of X=7-11, the lattice constants were little changed by an increase in the X values.

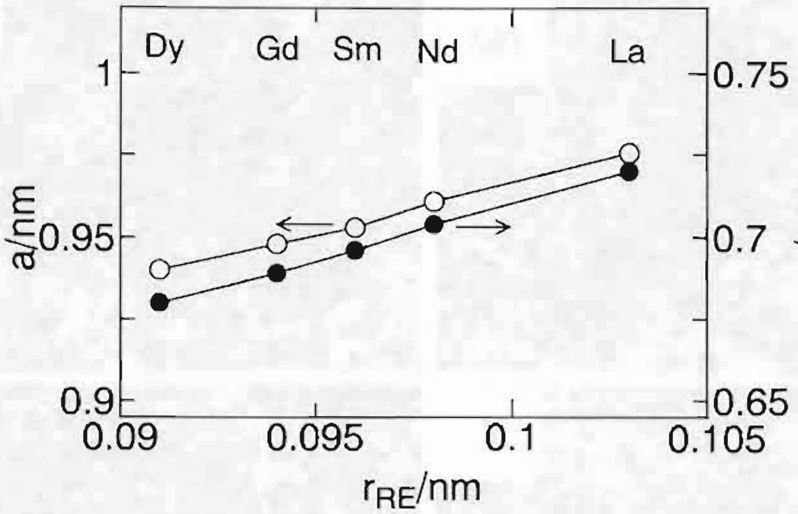

Fig. 4-2 Relationship between the ionic radius of rare-earth and the lattice parameters in hexagonal $RE_{10}Si_6O_{27}$.

Samples of the general formula, $M(II)_xNd_{10-x}Si_6O_{27-0.5x}$ (M(II)=Sr,Ba ; X=2-5), were prepared by partial substitution of Nd^{3+} in $Nd_{10}Si_6O_{27}$ with large divalent alkali-metal ions, to obtain larger lattice constants. Since the XRD patterns of these samples (excepting $Ba_5Nd_5Si_6O_{24.5}$) were similar to that of $Sr_2Nd_8(SiO_4)_6O_2$ (JCPDS file no.28-1237, hexagonal, $P6_3/m(176)$, a=0.9579nm, c=0.7111nm), the crystal structures of the major phase is a hexagonal apatite structure. Other very weak peaks can be assigned to those of Nd_2SiO_5. In the Sr substituted sample, the a-lattice constant of the major phase were not increased to the same extent by the M(II)-doping. (The lattice constants, c, of the Sr substituted samples became 0.0082nm larger.) In the Ba substituted samples, the lattice constants, a, became approximate 0.0100nm larger but were shorter than that of $La_{10}Si_6O_{27}$. (The lattice constants, c, became 0.0160nm larger and were almost equal to that of $La_{10}Si_6O_{27}$.)

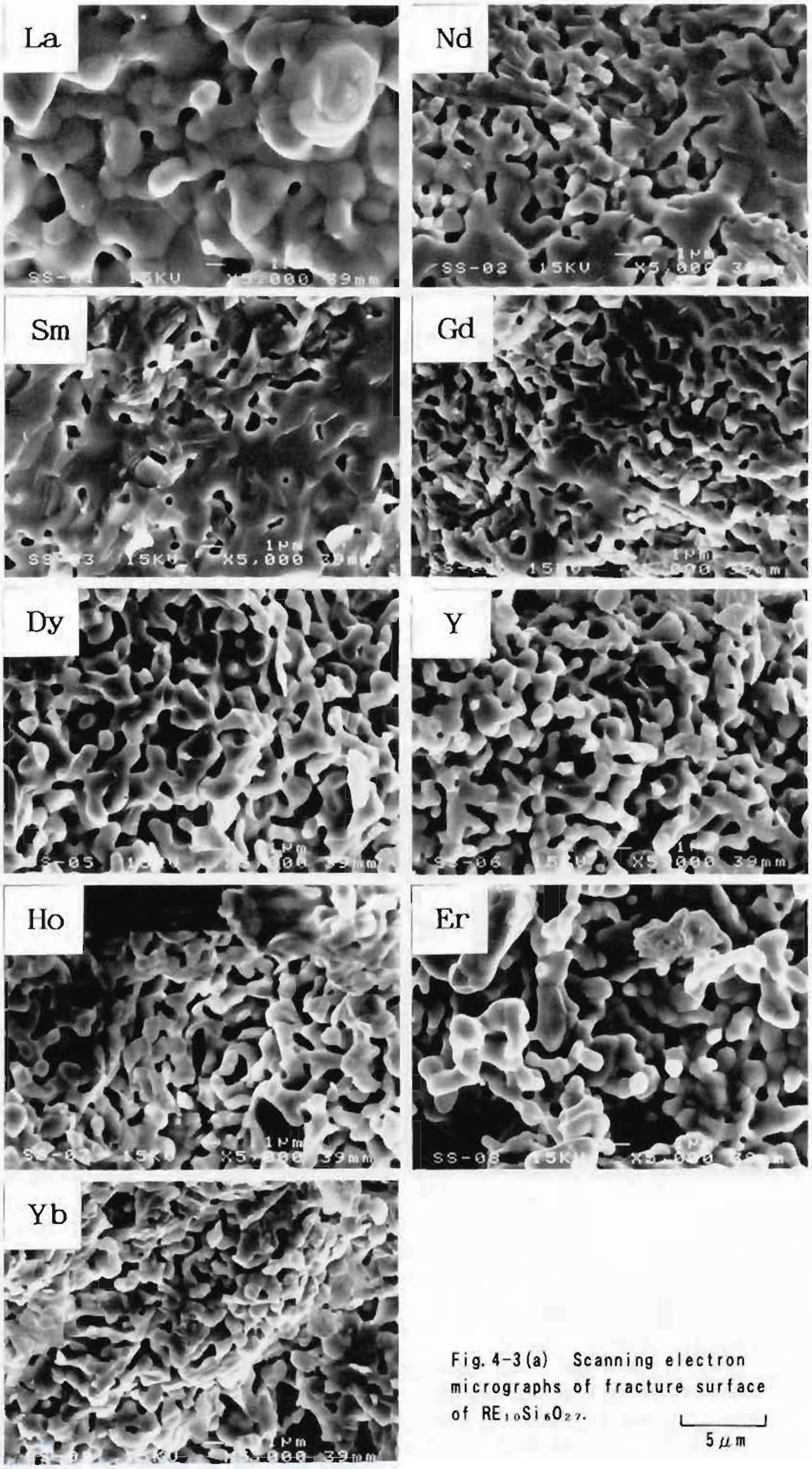

Fig. 4-3(a) Scanning electron micrographs of fracture surface of $RE_{10}Si_6O_{27}$.

5 μm

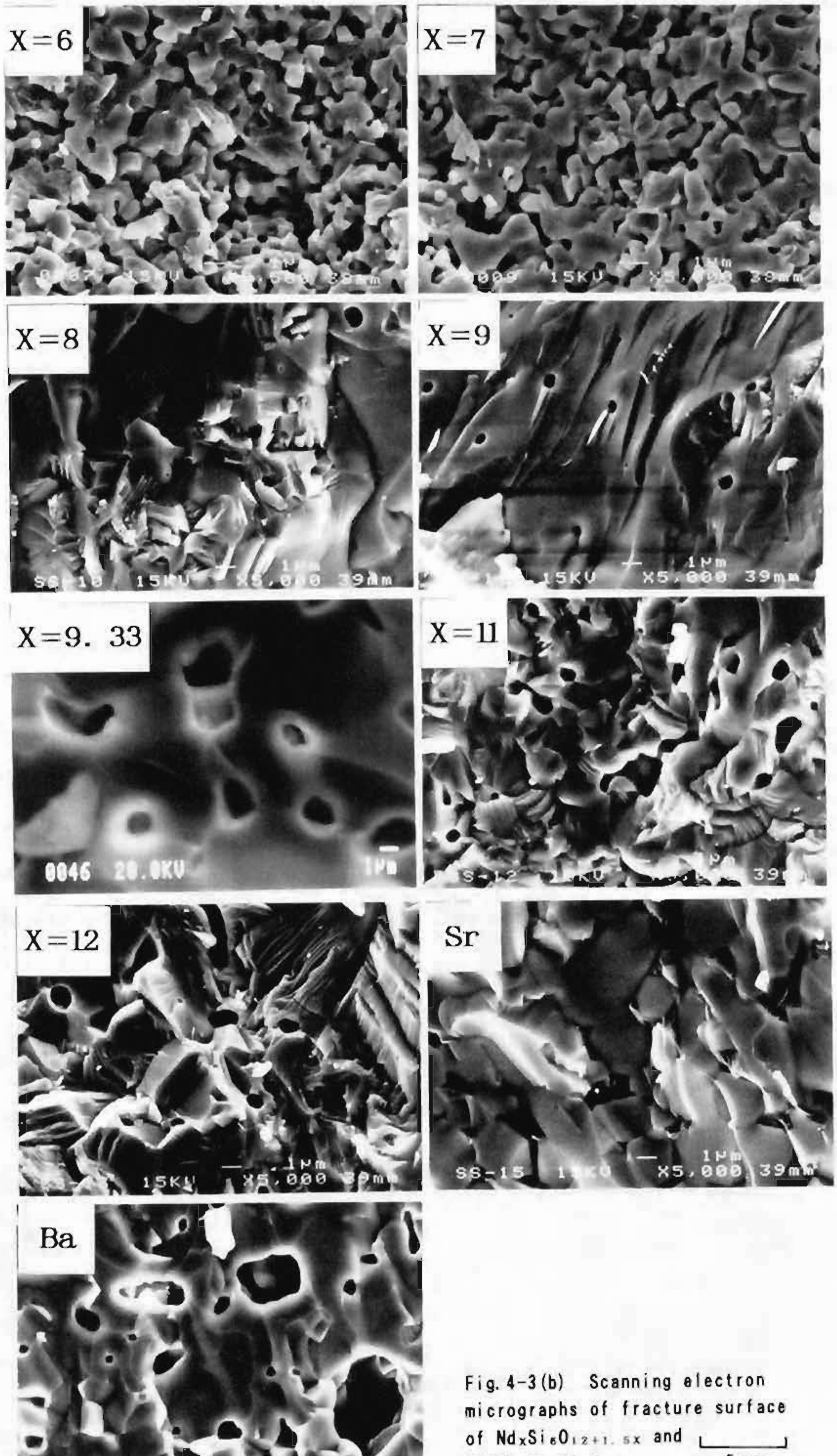

Fig. 4-3(b) Scanning electron micrographs of fracture surface of $Nd_xSi_6O_{12+1.5x}$ and $M(II)_2Nd_8Si_6O_{26}$.

5 μm

4-3-2. Microstructure

Figure 4-3 shows the fracture surface microstructures of the sintered rare-earth silicates. In the $RE_{10}Si_6O_{27}$ (RE=La,Nd,Sm,Gd,Dy,Y,Ho,Er,Yb) series, the densification increases with increasing ionic radius of rare-earth. In particular, the sintering is well progressed for the La and Sm samples. The particle size of the La and Sm samples is larger than those of the other samples. In the $Nd_XSi_6O_{12+1.5X}$ (X=6-12) series, the highest densification is observed for samples of X=8, 9 and 9.33. However, many cracks are observed for only sample of X=9.33. In the $M(II)_2Nd_8Si_6O_{26}$ (M(II)=Sr,Ba) series, the densification is well progressed though the large pores are observed.

4-3-3. Electrical properties

Complex-plane impedance analysis was performed according to section 2-2-3. The complex impedance plots give two semicircles as shown in Fig.4-4 : one in the higher frequency region corresponds probably to the bulk component, whereas another in the lower frequency region corresponds to the grain bundary component. When the temperature increased, the size of the semicircle in the lower frequency decreased compared with that in the higher frequency. The total conductivity data (the sum of

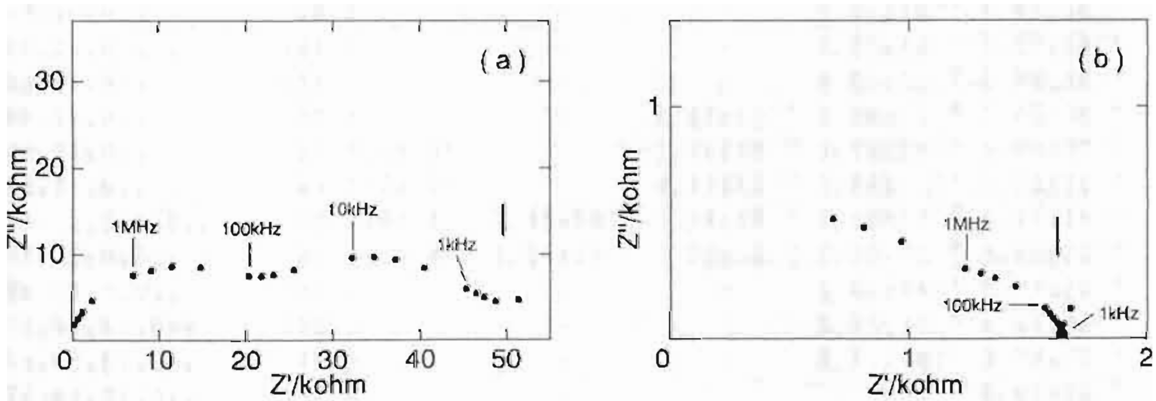

Fig. 4-4 Complex impedance plots of $Nd_{10}Si_6O_{27}$:
(a) at 300°C, (b) at 500°C.

the bulk and grain boundary) determined by the extrapolation of complex impedance plots to zero reactance were parameterized by the Arrthenius equation (2-12).

$$G \cdot T = G_0 \exp(-E/kT) \qquad (2\text{-}12)$$

Arrhenius plots are shown in Fig.4-5. Table 4-3 summarizes the electrical parameters. The relatively high conductivities and low activation energies of hexagonal $RE_{10}Si_6O_{27}$, especially $La_{10}Si_6O_{27}$ and $Nd_{10}Si_6O_{27}$, stimulated the present author to investigate their electrical properties. The electrical properties of hexagonal $RE_{10}Si_6O_{27}$ may be mainly dependent on the bulk component as in the case of the hexagonal M_2O-RE_2O_3-$2SiO_2$ explained in section 2-3-4.

Table 4-3 Electrical parameters

	activation energy /kJ·mol^{-1}	conductivity/S·cm^{-1} 300°C	500°C	700°C	900°C
$La_{10}Si_6O_{27}$	69.0	5.54×10^{-6}	1.75×10^{-4}	1.41×10^{-3}	2.85×10^{-3}
$Nd_{10}Si_6O_{27}$	71.5 (64.8)	5.02×10^{-6}	1.49×10^{-4}	8.42×10^{-4}	1.47×10^{-3}
$Sm_{10}Si_6O_{27}$	79.5 (64.5)	3.23×10^{-7}	1.43×10^{-5}	8.74×10^{-5}	1.61×10^{-4}
$Gd_{10}Si_6O_{27}$	84.0	–	7.05×10^{-7}	8.09×10^{-6}	1.84×10^{-5}
$Dy_{10}Si_6O_{27}$	107.5	–	–	1.17×10^{-6}	1.12×10^{-5}
$Y_{10}Si_6O_{27}$	120.3	–	–	6.79×10^{-8}	7.48×10^{-7}
$Ho_{10}Si_6O_{27}$	123.5	–	–	3.18×10^{-7}	4.17×10^{-6}
$Er_{10}Si_6O_{27}$	124.9	–	–	1.06×10^{-7}	1.31×10^{-6}
$Yb_{10}Si_6O_{27}$	131.6	–	–	1.44×10^{-3}	1.38×10^{-6}
$Nd_4Si_6O_{18}$	108.2	–	–	2.17×10^{-7}	1.97×10^{-6}
$Nd_5Si_6O_{19.5}$	116.7	–	–	1.27×10^{-7}	1.32×10^{-6}
$Nd_6Si_6O_{21}$	117.1	–	–	2.00×10^{-7}	2.23×10^{-6}
$Nd_7Si_6O_{22.5}$	90.7	–	1.47×10^{-7}	1.58×10^{-6}	1.45×10^{-5}
$Nd_8Si_6O_{24}$	90.7 (79.0)	–	1.10×10^{-6}	1.13×10^{-5}	5.80×10^{-5}
$Nd_9Si_6O_{25.5}$	83.7 (72.4)	–	4.33×10^{-6}	3.44×10^{-5}	1.50×10^{-4}
$Nd_{9.33}Si_6O_{26}$	73.3 (64.6)	2.96×10^{-7}	1.34×10^{-5}	1.02×10^{-4}	4.27×10^{-4}
$Nd_{11}Si_6O_{28.5}$	67.7 (58.4)	7.94×10^{-7}	2.02×10^{-5}	1.08×10^{-4}	3.00×10^{-4}
$Nd_{12}Si_6O_{30}$	124.3	–	–	2.66×10^{-7}	3.32×10^{-6}
$Sr_2Nd_8Si_6O_{26}$	110.3	–	–	9.75×10^{-8}	8.54×10^{-7}
$Ba_2Nd_8Si_6O_{26}$	75.9	–	–	8.17×10^{-7}	3.74×10^{-6}
$Ba_4Nd_6Si_6O_{25}$	167.8	–	–	–	1.61×10^{-6}
$Ba_5Nd_5Si_6O_{24}$	78.1	–	–	1.14×10^{-6}	4.84×10^{-6}

Parentheses denote the activation energy estimated in a higher temperature region.

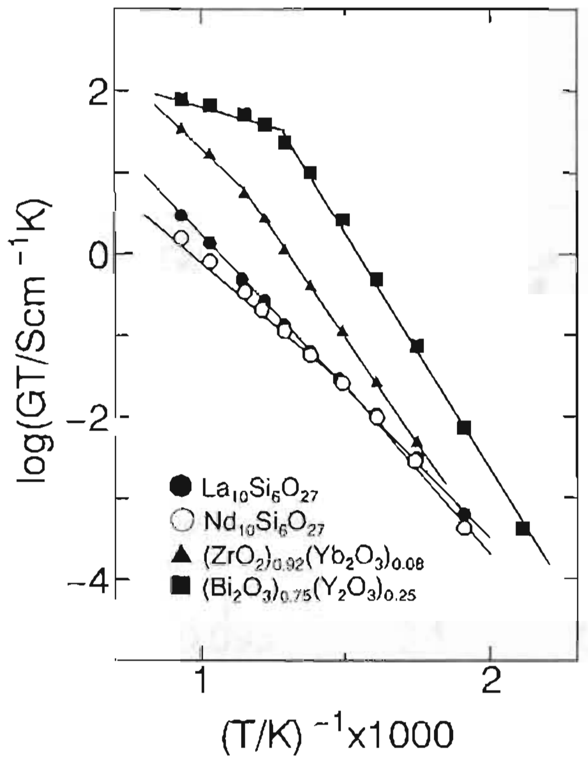

Fig. 4-5 Arrhenius plots.

Figure 4-6 shows the relationship between the ionic radius of RE^{3+} and the electrical properties of $RE_{10}Si_6O_{27}$ (RE=La,Nd,Sm,Gd,Dy). The activation energy decreases and the conductivity at 700℃ increases with an increase in the ionic radius of RE^{3+} for $RE_{10}Si_6O_{27}$. Based on Anderson and Stuart's model described in section 2-3-5, it is qualitatively understood that the lowering of activation energy with increasing size of rare-earth ion is caused by a lowering of the total elastic energy expressed by equation (2-14) [91,92]. The highest conductivity ($5.54 \times 10^{-5} S \cdot cm^{-1}$ at 300℃) was observed for $La_{10}Si_6O_{27}$ and this is almost equal to the conductivity of yitterbia stabilized zircona, $(ZrO_2)_{0.92}(Yb_2O_3)_{0.08}$. The conductivities of the monoclinic samples (RE=Y,Ho,Er and Yb) were considerably lower than those of the hexagonal samples (RE=La,Nd,Sm,Gd and Dy). For the $RE_{10}Si_6O_{27}$ series, the pre-exponential factor is independent on the ionic radius of RE^{3+} as shown in Fig.4-7. Therefore, the conductivity may be controlled by the activation energy which is influenced by the ionic size of RE^{3+}.

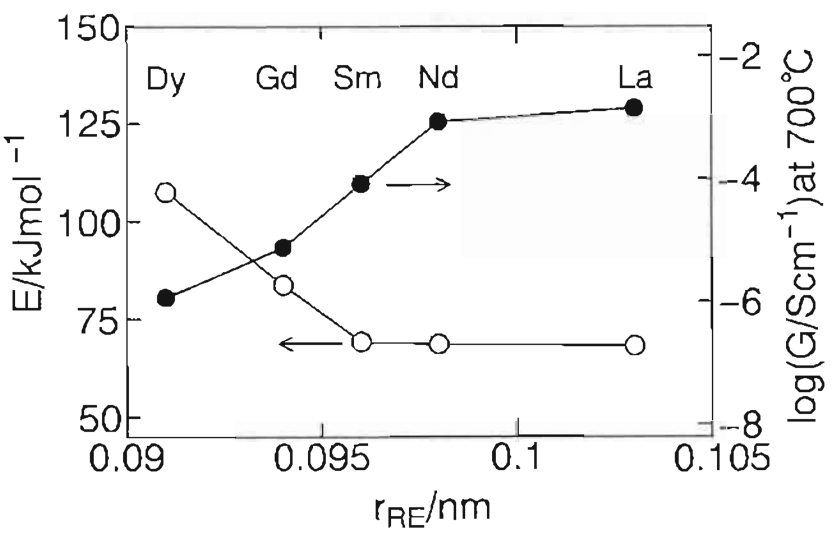

Fig. 4-6 Relationship between the ionic radius of rare-earth and the electrical parameters in hexagonal $RE_{10}Si_6O_{27}$.

In the $Nd_XSi_6O_{12+1.5X}$ (X=6-12) series, the activation energies of the tetragonal sample of X=6 and the monoclinic sample of X=12 are much high (>100kJ·mol^{-1}) and the conductivities of these samples are low, compared with those of the hexagonal samples of X=7-11. The highest conductivity and the lowest activation energy were observed for X=10 and 11, respectively, where these X-values are a little larger than X=8-9.33 for the composition of apatite structure, $Nd_X(SiO_4)_6O_{1.5X-12}$.

In the $M(II)_XNd_{10-X}Si_6O_{27-0.5X}$ (M(II)=Sr,Ba X=2,4) series, the conductivities were decreased by approximately three orders of magnitude compared with that of $Nd_{10}Si_6O_{27}$. The activation energies were higher than that of $Nd_{10}Si_6O_{27}$.

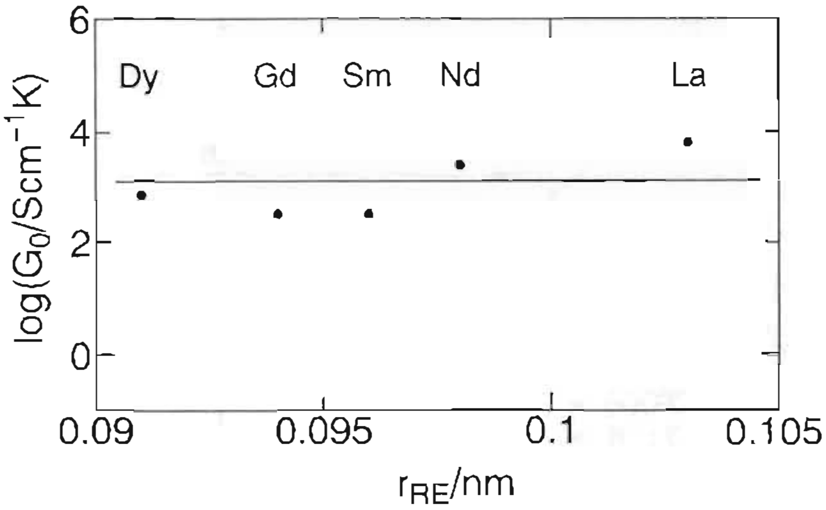

Fig. 4-7 Relationship between the ionic radius of rare-earth and the pre-exponential factor in hexagonal $RE_{10}Si_6O_{27}$.

4-3-4. Ionic transport number

The following O_2 gas concentration cell was prepared in order to determine the ionic transport number of the solid electrolyte.

O_2+Ar,Pt | solid electrolye | Pt,Air(21%O_2)

The EMF (electromotive force) between the two electrodes obeys the Nernst equation

$$\mathrm{EMF} = (RT/nF)\ln(P_{O2}/P_{O2}') \qquad (4\text{-}1)$$

where R, T, n, F, P_{O2} and P_{O2}' are the gas constant, absolute temperature, electron transfer number, Faraday constant, O_2 partial pressure at the measuring electrode, and O_2 partial pressure at the reference electrode (P_{O2}'=0.21), respectively. The 90% response time (EMF) was about 1 minute after changing the O_2 gas concentration on measuring electrode side. This response characteristics were similar to those of the O_2 gas concentration cell using the oxide ionic conductor, $(ZrO_2)_{0.92}(Yb_2O_3)_{0.08}$. Figure 4-8 shows the dependence of EMF on the logarithm of O_2 partial pressure,

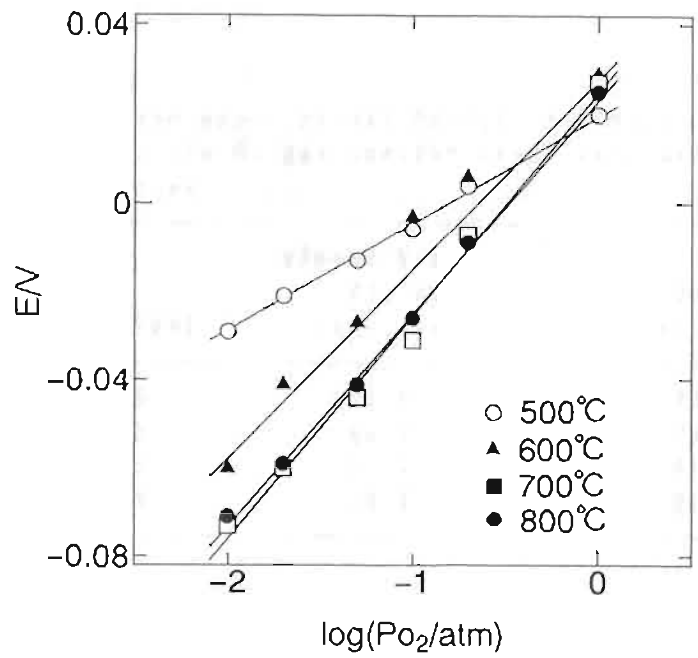

Fig. 4-8 Dependence of EMF on O_2 partial pressure : O_2+Ar, Pt | $Nd_{10}Si_6O_{27}$ | Pt, Air (21%O_2).

$\log P_{O_2}$, in the case of $Nd_{10}Si_6O_{27}$ and Table 4-4 summarizes the theoretical and experimental Nernstain slopes and electron transfer number (n) for the O_2 gas concentration cell at each temperature. The EMF's experimentally obtained are in good agreement with theoretical values. The n values are close to 4.0 above 600℃ for $Nd_{10}Si_6O_{27}$ and above 800℃ for $Sm_{10}Si_6O_{27}$. Therefore, this response must be caused by the four electron reaction of O_2 molecules at the electrodes. The current responses for a potential change from +1 to -1V of Pt | $Nd_{10}Si_6O_{27}$ | Pt were examined. The measurement was carried out at 500℃ in a N_2 atmosphere. A current flowed momentarily after the polar change and then approached zero. The conductivity of $RE_{10}Si_6O_{27}$ (RE=Nd,Sm) was measured by both ac and dc methods. The conductivity determined by the dc method was considerably lower than that determined by the ac method. Conversely, the conductivity in a moist atmosphere was the same as that in a dry atmosphere. These results suggest that $RE_{10}Si_6O_{27}$ is not a proton conductor.

Table 4-4 Theoretical and experimental Nernstian slopes and electron transfer numbers, n, for the O_2 gas concentration cell using rare-earth silicate solid electrolytes

temp. /°C	slope/mV·decade^{-1}				
		$Nd_{10}Si_6O_{27}$		$Sm_{10}Si_6O_{27}$	
	theoretical	observed	n	observed	n
500	37.5	24.0	6.3	22.4	6.7
600	42.3	42.3	4.0	29.4	5.8
700	47.2	50.4	3.8	40.4	4.7
800	52.1	48.7	4.2	50.5	4.1

From the above considerations, it is confirmed that the major charge carrier of the present solid electrolyte is not electrons, holes or protons but the O^{2-} ions.

4-4. Summary

New solid electrolytes comprising the rare-earth silicates, $RE_{10}Si_6O_{27}$ (RE=La,Nd,Sm,Gd,Dy,Y,Ho,Er,Yb) and $Nd_XSi_6O_{12+1.5X}$ (X=6-12), were prepared and their crystal structures, microstructures, electrical properties and ionic transport numbers were examined. The results are summarized as follows :

(1) In the $RE_{10}Si_6O_{27}$ series, the major crystal phases of RE=La, Nd, Sm, Gd and Dy as well as M_2O-RE_2O_3-$2SiO_2$ (M=Li,K,Rb,Cs RE=La,Nd,Sm,Gd,Dy) were hexagonal, those of RE=Y, Ho, Er and Yb were monoclinic. The hexagonal rare-earth silicates ($RE_{10}Si_6O_{27}$ (RE=La,Nd,Sm,Gd,Dy)) prepared were found to be a mixture of an apatite phase ($RE_{9.33}\square_{0.67}(SiO_4)_6O_2$) as the major phase and some crystal phases (RE_2SiO_5 etc.) as the minor phases. In the $Nd_XSi_6O_{12+1.5X}$ series, the major phases of samples X=6, X=7-11 and X=11 or 12 were tetragonal, hexagonal and monoclinic, respectively. For the hexagonal apatite structure group, the oxygen ions of 2a-site surrounded by six RE

ions exist and it is suggested that O^{2-} ions can migrate along the cavities of 2a-site in the c axial direction.

(2) $RE_{10}Si_6O_{27}$ (RE=La,Nd,Sm,Gd,Dy) showed relatively high conductivities and their activation energies were low. The activation energy decreased with increasing ionic radius of rare-earth . The lowest activation energy and the highest conductivity at 300℃ was $69.0 kJ \cdot mol^{-1}$ and $5.54x10^{-6} S \cdot cm^{-1}$, respectively. This conductivity is comparable to that of $(ZrO_2)_{0.92}(Yb_2O_3)_{0.08}$.

(3) The experimental electromotive force in the O_2 gas concentration cell comprising $Nd_{10}Si_6O_{27}$ agreed very well with the theoretical electromotive force calculated from the Nernst equation. Furthermore, the electron transfer number was very close to 4 above 600℃, suggesting that the response is due to the four electron reaction of O_2 molecules at the electrodes.

Chapter 5
Application to the concentration cell type CO_2 gas sensor of the alkali-metal rare-earth silicate solid electrolyte

5-1. Introduction

Recently, the combination of certain ionic conductive films and solid electrodes has made it possible to develop the gas sensors. The application of the solid electrolytes in this area have been extensively studied. For instance, there have been a number of CO_2 and NO_2 gas sensors, where β-alumina or Nasicon is used as the solid electrolyte and Na_2CO_3 or $NaNO_3$ as the solid electrode [93-97]. However, this type of gas sensors has not been to practical use to date. Consequently, the development of CO_2 gas sensors with high sensitivity, good selectivity, rapid response time, good long-term stability and high accuracy is required.

In this chapter, some solid state cells prepared from the high dense and conductive alkali-metal rare-earth silicates (potassium or lithium ionic conductor), and their response characteristics as the potentiometric CO_2 gas sensors have been investigated.

5-2. Thermodynamic analysis of electromotive force characteristics of the concentration cell type gas sensors [98]

According to the thermodynamics of cell reactions, the equilibrium potential difference of an electrochemical cell can be expressed as $\Delta G = -F \cdot E$, where E is EMF and ΔG is the Gibbs free energy. When the electric charge transfered is $|n|F$, the relationship is expressed as follows.

$$\Delta G = -|n| F \cdot E \qquad (5\text{-}1)$$

In the case of a general electrode reaction, aA + bB = cC + dD, the change in the Gibbs free energy is given by the activity coefficent of the reacting species.

$$\Delta G = \Delta G^{\circ} + RT\ln((a_C{}^c a_D{}^d)/(a_A{}^a a_B{}^b)) \quad (5\text{-}2)$$

The electromotive force is given by $E^{\circ} = -\Delta G^{\circ} / |n| F$ when the activities of the products and reacting species are 1. E° is called the standard electromotive force. The relationship between E° and the equilibrium constant of the electrode reaction is given by the following equation.

$$|n| FE^{\circ} = -\Delta G^{\circ} = RT\ln K \quad (5\text{-}3)$$

When equation (5-2) is divided by $-|n|F$, the following relationship is obtained.

$$E = E^{\circ} - (RT)/(|n|F)\ln((a_C{}^c a_D{}^d)/(a_A{}^a a_B{}^b)) \quad (5\text{-}4)$$

Equation (5-3) is the Nernst equation. (The partial pressure or concentration can be adopted instead of the activity.)

5-3. CO_2 gas sensor using the potassium ionic conductor, $K_2O\text{-}Sm_2O_3\text{-}6SiO_2$

Although some concentration cell type sensors using Na^+ and Li^+ ionic conductors have been reported, sensors using the K^+ ionic conductor is little known.

Thus, in this section the CO_2 gas sensors, in which the dense K^+ ionic conductors exhibiting high conductivity are used as the solid electrolyte, were prepared and investigated. From the following results, $K_2O\text{-}Sm_2O_3\text{-}6SiO_2$ was used as the solid electrolyte of the CO_2 gas sensor. As described in chapter 3, sample, n=2, shows the highest conductivity among the potassium ionic conductors, $K_2O\text{-}Sm_2O_3\text{-}nSiO_2$. However, there are the problems with the water-stability and long-term stability. The water-stability and densification increased with increasing SiO_2 content, but the conductivity decreased. Conversely, the conductivity of the n=6 sample was relatively high. Furthermore, its water-stability and densification were satisfactory.

5-3-1. Experimental

The sensor is composed of the following solid state cell.

(-) air, Pt | K^+ ionic conductor | Au, K_2CO_3, CO_2, O_2 (+)

The sensor structure is illustrated in Fig.5-1(a). The disc of ionic conductor (K_2O-Sm_2O_3-$6SiO_2$) used as the solid electrolyte was prepared according to the method

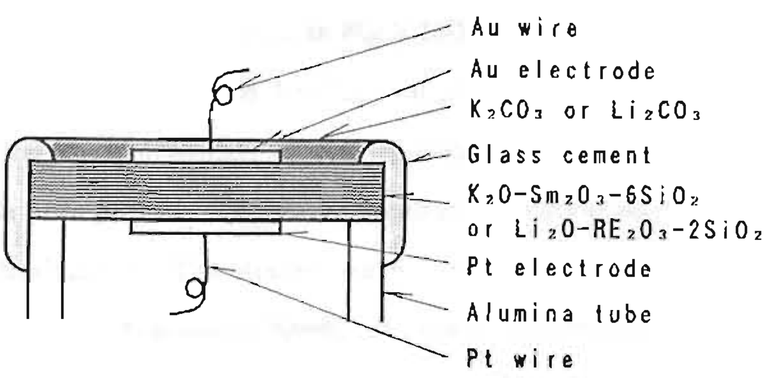

Fig. 5-1 (a) Schematic view of the CO_2 gas sensor.

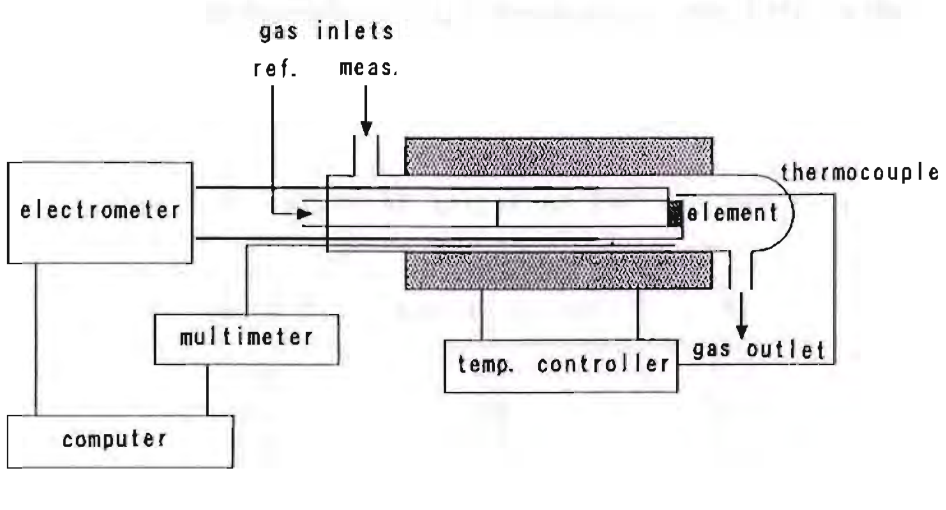

Fig. 5-1 (b) Schematic view of the CO_2 gas sensor response measurement equipment.

described in the section 3-2-1. After coating each side of the disc with a Pt and Au paste, the disc was baked at 800℃. Then, Pt wires were connected. An aqueous K_2CO_3 solution was applied to the Au detection electrode and dried, to prepare the solid electrode. The sensor was fixed on one-end of an alumina pipe with a glass cement. (The Pt counter electrode was inside.) The response characteristics were measured with the equipment shown in Fig.5-1(b). The standard CO_2 gases (<2ppm-, 10ppm-, 100ppm-, 1000ppm- and 1%-CO_2) prepared by diluting various amounts of CO_2 with synthetic air (<2ppmCO_2) were purchased from Sumitomo-Seika. These standard gases were passed through the detection electrode side of the sensors at the flow rate of 50cm^3·min^{-1}. The electromotive force, EMF, of the sensor was measured using a electrometer (Advantest, TR8652) at each temperature.

5-3-2. Results and discussion

As shown in Fig.3-3 (Arrhenius plots), the temperature (reciprocal) dependence of the conductivity for K_2O-Sm_2O_3-$6SiO_2$ in air was linear. This solid electrolyte is not a proton conductor, the conductivities in moist air are very close to those in dry air.

Figure 5-2 shows the dependence of the electromotive force, EMF, on the

Table 5-1 Values of slopes of EMF vs. log P_{CO_2} and electron number, n

temp. /°C	slope/mV·decade^{-1}	n
270	43	2.5
300	53	2.1
350	60	2.1
400	65	2.1
450	70	2.1
500	73	2.1
550	73	2.2
600	75	2.3

logarithm of CO_2 partial pressure, $\log P_{CO_2}$. The EMF decreases with increasing $\log P_{CO_2}$ at each temperature, and the dependence of EMF on $\log P_{CO_2}$ obeys the Nernst equation. In the present apparatus, almost constant potentials are obtained at a given temperature as the counter electrode is shielded from the detected gas. This indicates that the electron transfer number at the detection electrode can be estimated from the slope of the straight lines shown in Fig.5-2 as the EMF change is due to the potential change at the detection electrode. From Table 5-1, which summarizes the experimentally estimated slopes and electron transfer number, n, the n values can be approximated to 2.5 at 270℃ and to 2 above 300℃.

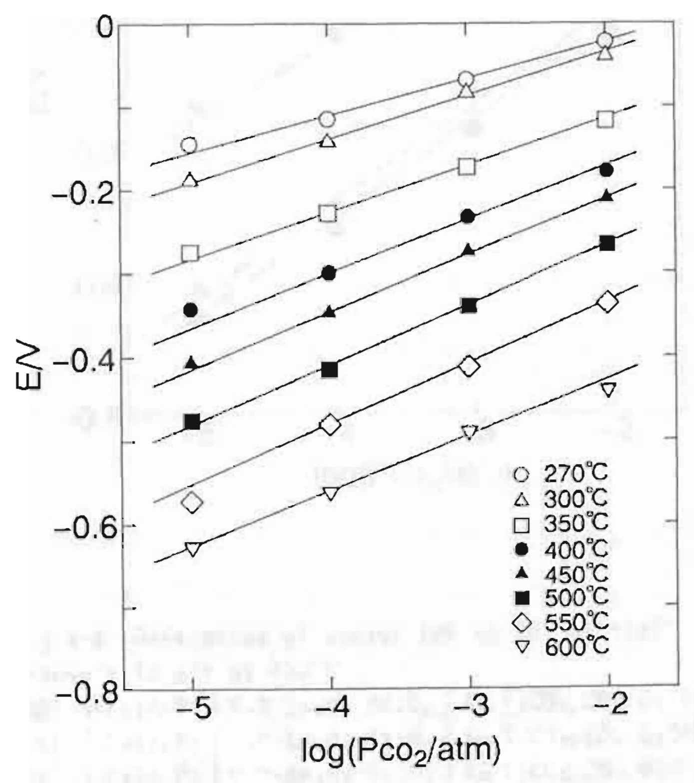

Fig. 5-2 Dependence of sensor EMF on CO_2 partial pressure in air :
(-) air, Pt | K_2O-Sm_2O_3-$6SiO_2$ | Au, K_2CO_3, CO_2, O_2 (+).

The dependences of EMF on logP_{CO_2} at 450℃ were also measured for the CO_2 gas sensors prepared from K_2O-Sm_2O_3-$2SiO_2$ and K_2O-Sm_2O_3-$4SiO_2$. The results are shown in Fig.5-3. The EMF shows a tendency to decrease with increasing SiO_2 content. This may be due to the lowering of K_2O activity in the solid electrolyte.

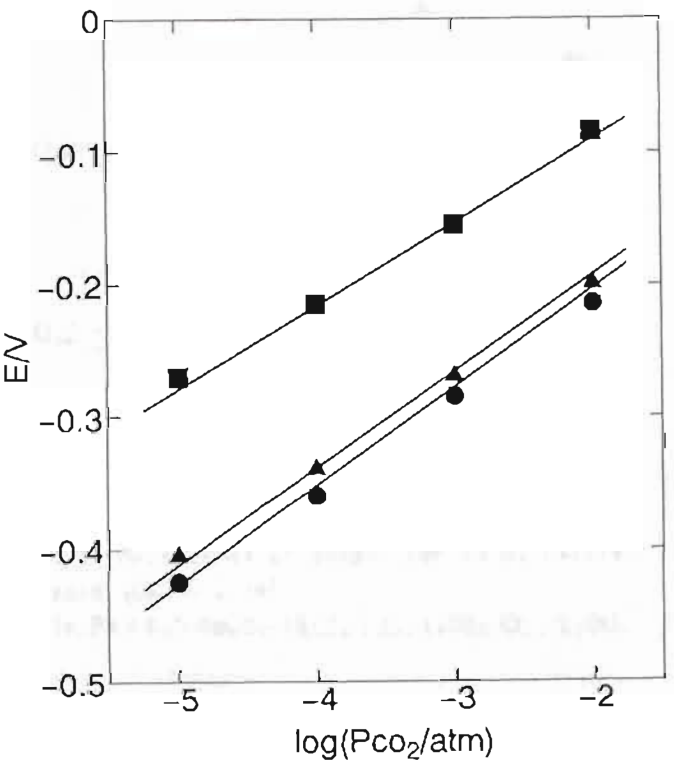

Fig. 5-3 Dependence of sensor EMF on CO_2 partial pressure in air at 450°C :
(●) (-)air, Pt | K_2O-Sm_2O_3-$6SiO_2$ | Au, K_2CO_3, CO_2, O_2 (+),
(▲) (-)air, Pt | K_2O-Sm_2O_3-$4SiO_2$ | Au, K_2CO_3, CO_2, O_2 (+),
(■) (-)air, Pt | K_2O-Sm_2O_3-$2SiO_2$ | Au, K_2CO_3, CO_2, O_2 (+).

The dependences of EMF on the logarithm of O_2 partial pressure, logP_{O_2}, under the CO_2 partial pressure of 0.3atm are shown in Fig.5-4. The EMF values shown in Fig.5-4 are somewhat different from those determined by the extrapolation of the plots in Fig.5-2 because the absolute EMF values showed a significant scatter among

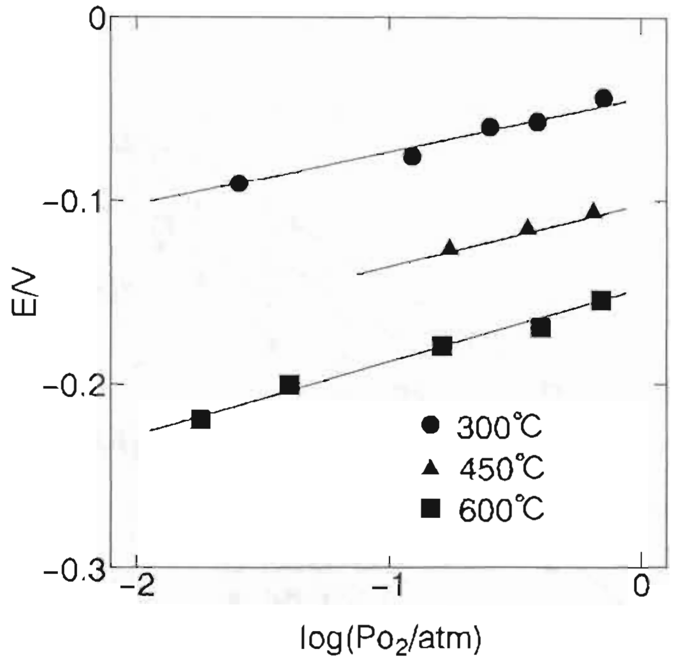

Fig. 5-4 Dependence of sensor EMF on O_2 partial pressure (CO_2=0. 3atm) :
(-) air, Pt | K_2O-Sm_2O_3-$6SiO_2$ | Au, K_2CO_3, CO_2, O_2 (+).

sensors. The EMF at each temperature increased linearly with increasing $\log P_{O_2}$ and the dependence of EMF on $\log P_{O_2}$ obeyed the Nernst equation (as in the case of CO_2). The experimental slopes at 300, 450 and 600℃ was 29, 34 and 41mV/decade, respectively. The electron transfer number for one molecule of O_2 is estimated as 3.9. 4.2 and 4.2, respectively. These results indicate that the two electron reaction of CO_2 and four electron reaction of O_2 is the method of detection above 300℃.

Figure 5-5 shows the temperature dependence of the EMF at a given CO_2 concentration. The EMF values decrease linearly with increasing temperature, though deviation from the straight line is observed below 300℃. The temperature dependence of the potential at the detection electrode is linear above 300℃ and hence the temperature dependence of the potential at the counter electrode is also expected to be linear, indicating that the same electrode reaction occurs at the detection electrode above 300℃.

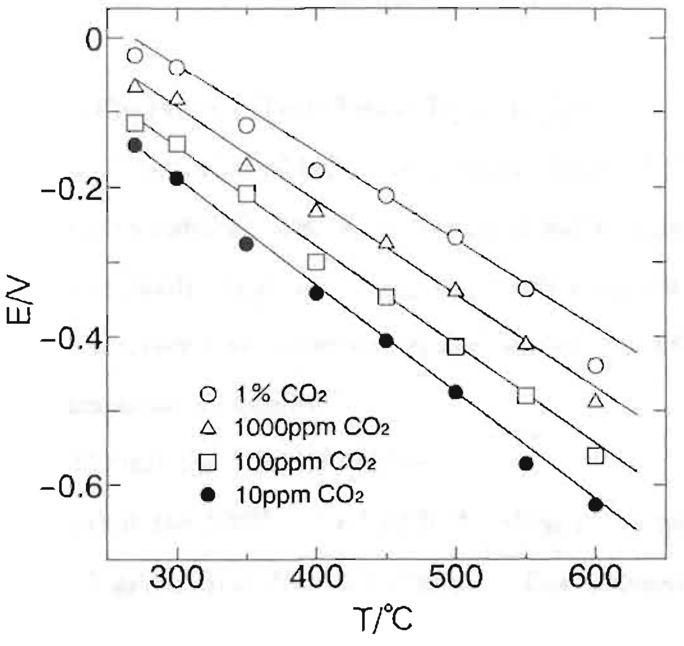

Fig. 5-5 Temperature dependence of sensor EMF in air :
(-) air, Pt | K_2O-Sm_2O_3-$6SiO_2$ | Au, K_2CO_3, CO_2, O_2 (+).

From the above results, the response mechanism of the present CO_2 gas sensor can be explained as follows. Because the counter electrode is exposed to atmosphere (the oxygen partial pressure is always 0.21atm), the electrode reaction can be expressed by the following equation.

$$2K^+ + 1/2O_2^{I} + 2e^- = K_2O \qquad (5\text{-}5)$$

On the other hand, the following reaction is thought to occur at the detection electrode.

$$2K^+ + CO_2 + 1/2O_2^{II} + 2e^- = K_2CO_3 \qquad (5\text{-}6)$$

When the Nernst equation is applied to equations (5-5) and (5-6), the potential of the counter electrode, Ec, and that of the detection electrode, Es, are expressed by the following equations :

$$Ec = Ec' - (RT/2F)\ln(a_{K_2O}/a_{K^+}^{2} \cdot (P_{O_2}^{I})^{1/2}) \tag{5-7}$$

$$Es = Es' - (RT/2F)\ln(a_{K_2CO_3}/a_{K^+}^{2} \cdot (P_{O_2}^{II})^{1/2} \cdot P_{CO_2}) \tag{5-8}$$

where Ec' and Es' are the constants. Therefore, the electromotive force, E, is expressed as follows :

$$\begin{aligned} E &= Es - Ec \\ &= E' - (RT/2F)\ln(a_{K_2CO_3} \cdot (P_{O_2}^{I})^{1/2}/a_{K_2O} \cdot P_{CO_2} \cdot (P_{O_2}^{II})^{1/2}) \end{aligned} \tag{5-9}$$

where E' is a constant. The value of $\ln P_{O_2}^{I}$ is constant because $P_{O_2}^{I}$ is the oxygen partial pressure in the atmosphere. The K^+ activities of K_2CO_3 and solid electrolyte are considered to be essentially constant during the electrode reactions. Therefore, assuming that the K^+ activities are constant regardless of the CO_2 concentration, equation (5-9) can be simplified as follows.

$$E = E' + (RT/2F)\ln P_{CO_2} + (RT/4F)\ln P_{O_2}^{II} \tag{5-10}$$

Equation (5-10) means that the EMF agreed with the slope corresponding to the two electrons reaction for $\log P_{CO_2}$ and four for $\log P_{O_2}$. The present results can be explained by this equation.

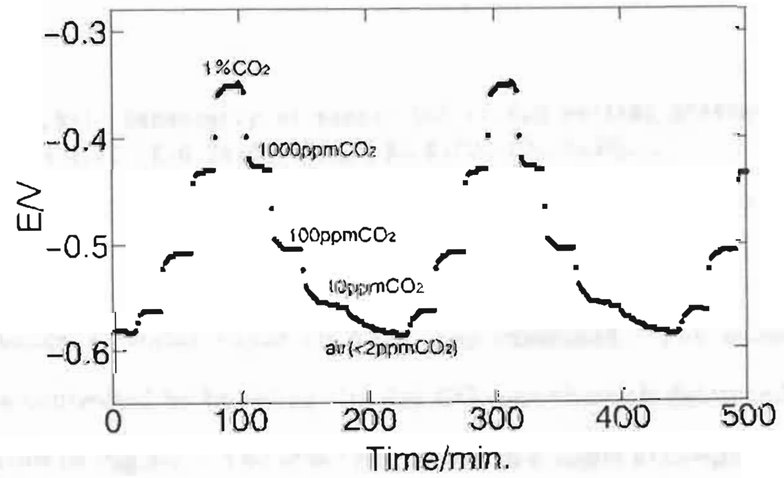

Fig. 5-6 Response curve, sensor EMF in air at 550°C : (-) air, Pt | $K_2O-Sm_2O_3-6SiO_2$ | Au, K_2CO_3, CO_2, O_2 (+).

Figure 5-6 shows the EMF response curve for changing CO_2 concentration at 550℃. The EMF response was relatively rapid. When the CO_2 concentration increases, the 90% response time is approximately 4 minutes and the reproducibility is good.

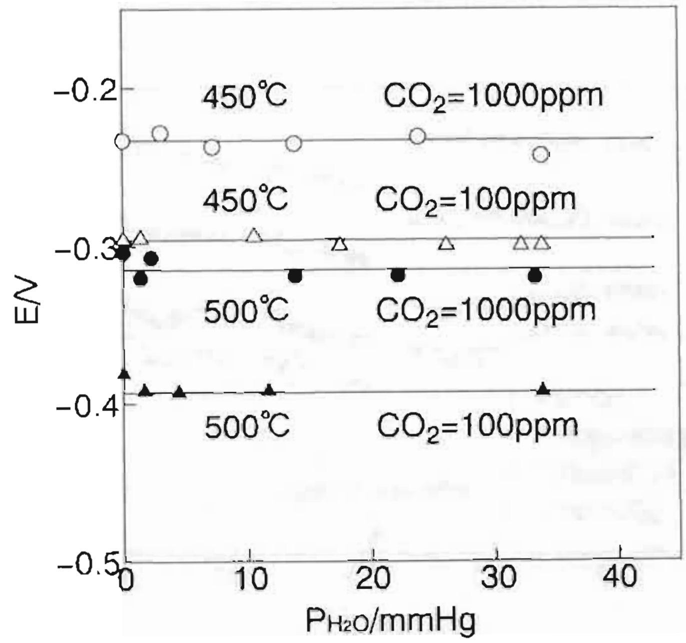

Fig. 5-7 Dependence of sensor EMF on H_2O partial pressure : (−) air, Pt | K_2O-Sm_2O_3-$6SiO_2$ | Au, K_2CO_3, CO_2, O_2 (+).

The influence of water vapor on EMF was examined. The moist atmosphere condition was controlled by bubbling the dry CO_2 gas through deionized water. The results are given in Fig.5-7. The observing EMF, in a moist atmosphere at 500℃, are about 10mV lower than that in a dry atmosphere. However, the EMF's at 450℃ are not influenced by the introduction of water vapor.

The stability of the EMF was examined in a laboratory air for 87 days. The EMF was measured after maintaining the device at the operating temperature, 500℃, for several hours in all cases. After the measurement, the apparatus was cooled to room temperature and kept in a ambient air. The results are given in Fig.5-8. The EMF tended to decrease during the first 10 days. After that, it remained essentially constant (especially, in 1000ppm- and 1%-CO_2), except the shift of +30mV by the break of a lead wire after storage of 40 days. It is unclear that the shift after the break of a lead wire may be attributed to the reproduction of a lead wire and the solid electrode.

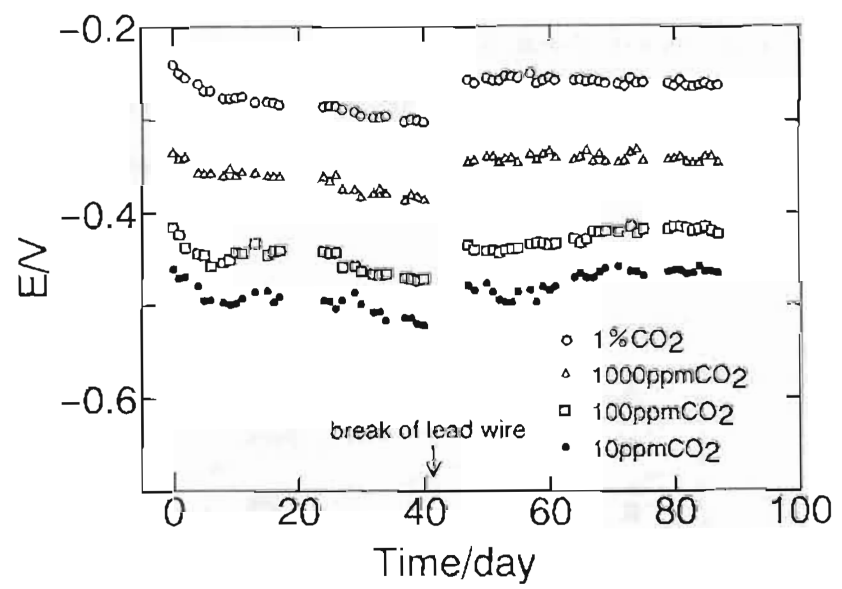

Fig. 5-8 Long-term stability in a laboratory air:
(-) air, Pt | K_2O-Sm_2O_3-$6SiO_2$ | Au, K_2CO_3, CO_2, O_2 (+).

5-4. CO_2 gas sensor using the lithium ionic conductor.

Li_2O-RE_2O_3-$2SiO_2$ (RE=La,Nd,Sm)

CO_2 gas sensors prepared from the Li^+ ionic conductors have been investigated. The Li^+ ionic conductors are dense and show high conductivity similar to the K^+ ionic conductors discussed in section 5-3.

5-4-1. Experimental

The sensors are composed of the following solid state cell.

(-) air, Pt | Li^+ ionic conductor | Au, Li_2CO_3, CO_2, O_2 (+)

The sensor structure is the same as that shown in Fig.5-1(a) of section 5-3-1. Discs of the ionic conductor, Li_2O-RE_2O_3-$2SiO_2$ (RE=La,Nd,Sm), which were used as the solid electrolyte, were prepared according to the method described in section 2-2-1. Au or Pt electrode were prepared on each side of the discs by sputtering. Au lead wires were used. In order to prepare the solid electrode, the aqueous Li_2CO_3 solution was applied to the Au detection electrode and dried. All other procedures were as those detailed in section 5-3-1.

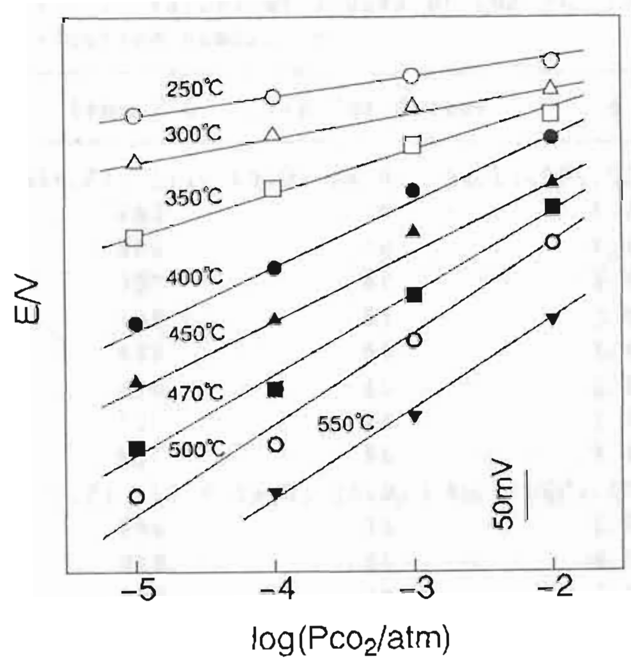

Fig. 5-9 Dependence of sensor EMF on CO_2 partial pressure in air :
(-) air, Pt | Li_2O-La_2O_3-$2SiO_2$ | Au, Li_2CO_3, CO_2, O_2 (+).

5-4-2. Results and discussion

Figure 5-9 shows the dependence of EMF on $\log P_{CO_2}$ when Li_2O-La_2O_3-$2SiO_2$ is used as the solid electrolyte. The relative EMF values are plotted on the y-axis, since the absolute EMF values showed a significant scatter among sensors. Although the EMF decreased with an increase in the $\log P_{CO_2}$ at each temperature, the slope below 350℃ was small compared with that above 400℃. The dependence of EMF on $\log P_{CO_2}$ is considered to obey the Nernst equation above 400℃. Similar results were obtained for the other solid electrolytes such as Li_2O-Nd_2O_3-$2SiO_2$ and Li_2O-Sm_2O_3-$2SiO_2$. Furthermore, the potential is expected to be constant at a given temperature as the Pt counter electrode is not

Table 5-2 Values of slopes of EMF vs. $\log P_{CO_2}$ and electron number, n

temp. /°C	slope/$mV \cdot decade^{-1}$	n
air, Pt | Li_2O-La_2O_3-$2SiO_2$ | Au, Li_2CO_3, CO_2, O_2		
250	18	5.8
300	28	4.1
350	40	3.1
400	51	2.6
450	59	2.4
470	65	2.3
500	74	2.1
550	68	2.4
air, Pt | Li_2O-Sm_2O_3-$2SiO_2$ | Au, Li_2CO_3, CO_2, O_2		
250	15	6.9
300	25	4.5
350	48	2.6
400	56	2.4
450	67	2.1
470	65	2.3
air, Pt | Li_2O-Nd_2O_3-$2SiO_2$ | Au, Li_2CO_3, CO_2, O_2		
250	29	3.6
300	40	2.8
350	47	2.6
400	63	2.1
450	62	2.3

exposed to the detection gas. Therefore, the electron transfer number at the Au detection electrode can be estimated from the slope of the straight lines shown in Fig.5-9, as the EMF change is due to the potential change at the detection electrode. Table 5-2 summarizes the experimental slopes and electron transfer numbers. These results indicate that the two electron reaction of CO_2 is the method of detection above 400℃ for all of the solid electrolytes .

The dependence of EMF on $\log P_{O_2}$ was examined under a constant CO_2 partial pressure of 0.2atm, to elucidate the detection electrode reactions. Results obtained for Li_2O-La_2O_3-$2SiO_2$ are shown in Fig.5-10. The EMF increases linearly with an increase of the $\log P_{O_2}$ (in the range studied) at each temperature. This relationship obeys the Nernst equation as in the case of CO_2. The experimental slopes at 400 and 450℃ was 31 and 37mV/decade, respectively. The electron transfer number for one molecule of O_2 is estimated as 4.3 and 3.9, respectively. These results indicate that the two electron reaction of CO_2 and four electron reaction of O_2 is the method of detection above 400℃.

From the above results, the response mechanism for the CO_2 gas sensor of Li_2O-RE_2O_3-$2SiO_2$ can be explained as described for K_2O-Sm_2O_3-$6SiO_2$ in section 5-3-2, except for the reacting ion species.

The EMF response for changing CO_2 concentration at 470℃ was relatively rapid. The 90% response time was about 4 minutes and the reproducibility was good.

From the results in section 5-3-2 and this section, the working temperature of K_2O-Sm_2O_3-$6SiO_2$ sensor was found to be 100℃ lower than that of Li_2O-RE_2O_3-$2SiO_2$ (RE=La,Nd,Sm) sensor : the EMF of the former sensor obeyed the Nernst equation above 300℃ when the CO_2 concentration is changed, whereas the EMF of the latter sensor obeyed above 400℃. It is unclear that the difference in electrolyte and/or solid electrode may be responsible for the difference in working temperature.

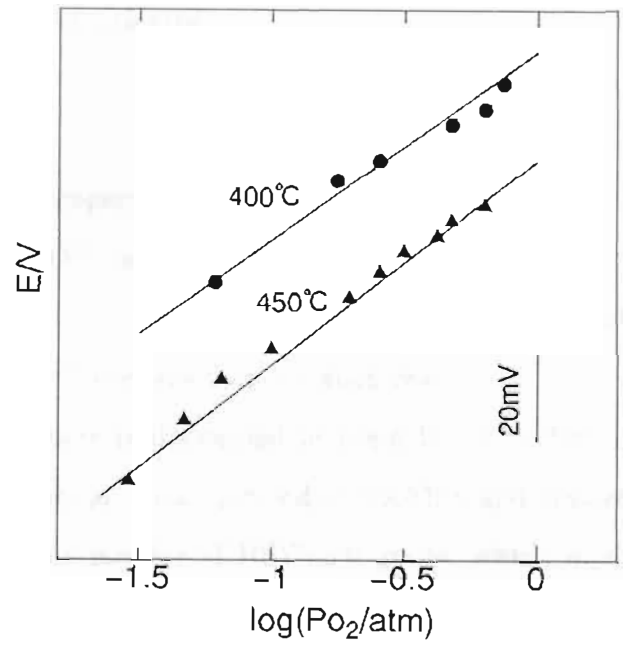

Fig. 5-10 Dependence of sensor EMF on O_2 partial pressure (CO_2=0.3atm) :
(-) air, Pt | Li_2O-La_2O_3-$2SiO_2$ | Au, Li_2CO_3, CO_2, O_2 (+).

5-5. CO_2 gas sensor using the layer type ionic conductor, Li_2O-Sm_2O_3-$2SiO_2$+$(ZrO_2)_{0.92}(Yb_2O_3)_{0.08}$

In the CO_2 gas sensors examined in sections 5-3 and 5-4, the electromotive force was modified by changing of O_2 concentration because the four electron reaction of O_2 occurs at the detection electrode as well as the two electron reaction of CO_2. In an attempt to improve the selectivity for O_2, one-end seal type sensors have been reported, where the O^{2-} ionic conductor is put on the counter electrode side of the alkali-metal ionic conductor.

A CO_2 gas sensor was prepared from the layer type ionic conductor obtained by sticking the O^{2-} ionic conductor on the counter electrode of Li^+ ionic conductor, and its properties have been investigated.

5-5-1. Experimental

The sensors are composed of the following solid state cell.

(-)CO_2, O_2, Pt | O^{2-} ionic conductor

+ Li^+ ionic conductor | Au, Li_2CO_3, CO_2, O_2(+)

<<layer type ionic conductor>>

The sensor structure is illustrated in Fig.5-11. The disc of yitterbia stabilized zirconia, $(ZrO_2)_{0.92}(Yb_2O_3)_{0.08}$, was pressed at 100MPa and sintered at 1600℃ for 2 h. The $(ZrO_2)_{0.92}(Yb_2O_3)_{0.08}$ powder of HSYb-8.0 grade, which was prepared by the co-precipitation method, was purchased from Daiichi Kigenso Kagaku Kogyo Co., Ltd. The layer type ionic conductor was prepared by sticking the greenbody of Li_2O-Sm_2O_3-$2SiO_2$ on the yitterbia stabilized zirconia and then by melting at 1200℃ for 2 h. Au and Pt electrodes were prepared by sputtering on the Li_2O-Sm_2O_3-$2SiO_2$ and $(ZrO_2)_{0.92}(Yb_2O_3)_{0.08}$ sides, respectively. Au lead wires were used. The Au detection electrode and the Pt counter electrode were exposed to the same CO_2 gas atmosphere. The other procedures were the same as those described in sections 5-3-1 and 5-4-1.

5-5-2. Results and discussion

In general, the preparation of the layer type ionic conductors used in this work is very difficult because of the difference in thermal expansion coefficient and reaction between the alkali-metal ionic conductor and the stabilized zirconia. Among the alkali-metal ionic conductors developed in chapters 2 and 3, only a combination of Li_2O-RE_2O_3-$2SiO_2$ (RE=La,Nd,Sm,Gd,Dy) and $(ZrO_2)_{0.92}(Yb_2O_3)_{0.08}$ was successful. It is well known that these stabilized zirconias is highly dense and possess the high strength and are superior as the solid electrolyte of the gas sensor. Therefore, layer type ionic conductor prepared from stabilized zirconia is expected to be good solid electrolyte.

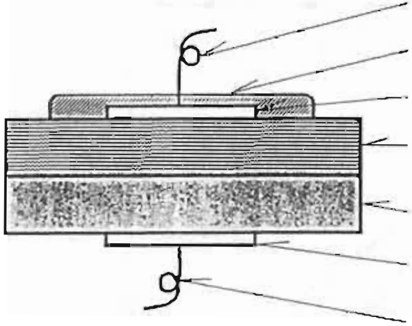

Fig. 5-11 Schematic view of the CO_2 gas sensor using the layer type solid electrolyte.

Figure 5-12 shows the dependences of EMF on $\log P_{CO_2}$ and $\log P_{O_2}$ for the sensor prepared using Li_2O-Sm_2O_3-$2SiO_2$ + $(ZrO_2)_{0.92}(Yb_2O_3)_{0.08}$ as the solid electrolyte. The EMF decreases with an increase in the $\log P_{CO_2}$ at 450 and 500℃ and the relationship obeys the Nernst equation. The electron transfer number estimated from the experimental slope is approximately 2. This indicates that the two electron reaction of CO_2 occurs at the detection electrode. On the other hand, the EMF was little affected by the change of the O_2 partial pressure when the CO_2 partial pressure is kept constant at 450 or 500℃.

Such independence of EMF on the O_2 partial pressure can be explained, based on the response mechanism. It is plausible that the following reaction associated with the two electron transfer for CO_2 and the four electron transfer for O_2 occurs at the detection electrode.

$$2Li^+ + CO_2 + 1/2O_2 + 2e^- = Li_2CO_3 \qquad (5\text{-}11)$$

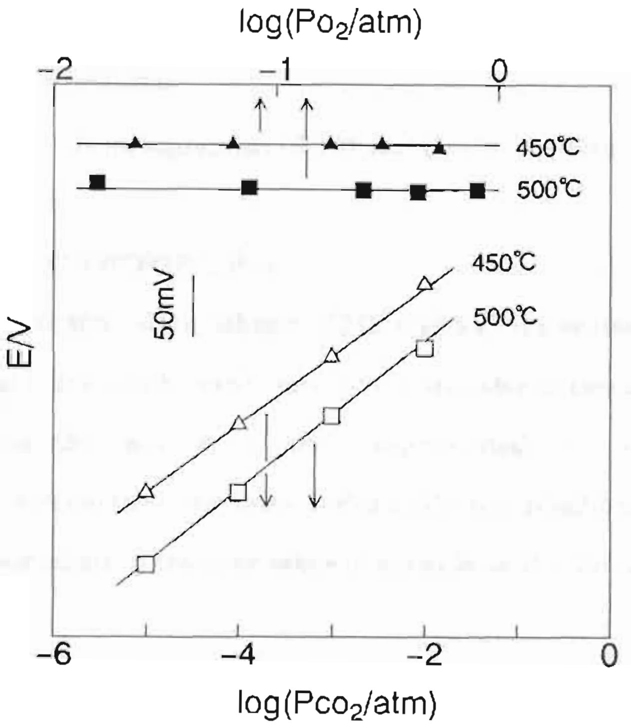

Fig. 5-12 Dependence of sensor EMF on CO_2 partial pressure in air and O_2 partial pressure (CO_2=0.3atm) :
(-) CO_2, O_2, Pt | $(ZrO_2)_{0.92}(Yb_2O_3)_{0.08}$+$Li_2O$-$Sm_2O_3$-$2SiO_2$ | Au, Li_2CO_3, CO_2, O_2 (+).

Therefore, the detection electrode potential, Es, can be expressed by the following equation :

$$Es = Es' - (RT/2F)\ln(a_{Li2CO3}/(a_{Li^+}^{2}\cdot P_{CO2}\cdot P_{O2}^{1/2})) \qquad (5\text{-}12)$$

where Es' is a constant. Here, it is reasonably supposed that the activity of Li^+ in Li_2CO_3 and in the solid electrolyte does not change during the electrode reactions shown in equation (5-11). This means that the activity of Li^+ is constant regardless of CO_2 concentration, and hence equation (5-12) can be simplified as follows.

$$Es = Es' + (RT/2F)\ln P_{CO2} + (RT/4F)\ln P_{O2} \qquad (5\text{-}13)$$

On the other hand, the following reaction associated with the four electron transfer should be considered at the counter electrode.

$$O_2 + 4e^- = 2O^{2-} \qquad (5\text{-}14)$$

This indicates that the potential of the counter electrode can be expressed by the following equation :

$$Ec = Ec' + (RT/4F)\ln P_{O_2} \tag{5-15}$$

where Ec' is a constant. From equations (5-13) and (5-15), the total potential, E, can be expressed as follows.

$$E = Es - Ec = E' + (RT/2F)\ln P_{CO_2} \tag{5-16}$$

This equation shows that the relationship of EMF and $\log P_{CO_2}$ is linear and also that the slope of the straight line can be explained by the transfer of two electrons. Thus, the experimental results are very well represented by equation (5-16). Equation (5-16) does not contain the term $\ln P_{O_2}$ since the reaction of O_2 molecules associated with the four electron transfer takes place at both the detection and counter electrodes.

The EMF response was more rapid for an increase in the CO_2 concentration, compared with that for a decrease in the CO_2 concentration. This observation is similar to that for the sensor described in section 5-4-2. The 90% response times for an increase and a decrease in the CO_2 concentration were about 2 and 4 minutes, respectively. The reproducibility was good.

5-6. Summary

Three types of potentiometric CO_2 gas sensors have been investigated, using K_2O-Sm_2O_3-$6SiO_2$, Li_2O-RE_2O_3-$2SiO_2$ (RE=La,Nd,Sm) or Li_2O-Sm_2O_3-$2SiO_2$ +$(ZrO_2)_{0.92}(Yb_2O_3)_{0.08}$ (the layer type ionic conductor) as the solid electrolyte. Results obtained are summarized as follows :

(1) In changing CO_2 concentration, the electromotive force of the sensor prepared from the potassium ionic conductor obeyed the Nernst equation above 300℃. The sensor prepared from the lithium ionic conductor obeyed the Nernst equation above 400℃.

(2) The electromotive force response in a changing CO_2 concentration was relatively

rapid. The 90% response time was about 4 minutes and the reproducibility was good.

(3) The two electron transfer reaction associated with the CO_2 molecule and the four electron transfer reaction associated with the O_2 molecule were found to occur at the detection electrode.

(4) Since the four electron transfer reaction associated with the O_2 molecules occur at both the detection and counter electrode in the layer type ionic conductor, the potential changes of both electrodes were compensated, hence the selectivity for O_2 was excellent.

Chapter 6
Concluding remarks

Recently, there has been considerable interest in dense ionic conductors (as the solid electrolyte material) with high conductivity, in the application areas of solid state batteries and chemical sensors. This is especially tried for materials containing oxo groups, such as SiO_4, PO_4, GeO_4 and ZrO_2 which can act as alkali-metal ionic conductors having high conductivity. Ionic conductors containing rare-earths (RE) which show high conductivity have also been examined. In this study, a series of solid electrolytes consisting of the rare-earth silicate have been prepared and their properties examined. Moreover, application of concentration cell type CO_2 gas sensors of these solid electrolytes have been attempted. Results obtained are summarized as follows :

In chapter 2, the preparation of alkali-metal rare-earth silicates, M_2O-RE_2O_3-$2SiO_2$ (M=Li,Na,K,Rb,Cs RE=La,Nd,Sm,Gd,Dy,Y,Ho,Er,Yb), as the new solid electrolytes, and their crystal structures, microstructures and electrical properties were reported. For M_2O-RE_2O_3-$2SiO_2$ (M=Li,K RE=La,Nd,Sm,Gd,Dy and M=Rb,Cs RE=La,Nd,Sm), the same hexagonal structure was confirmed. The major phase in these hexagonal samples is an apatite structure of composition, $M_XRE_{10-X}(SiO_4)_6O_{3-X}$ (X=1-3). Glass phases and small amount of unidentified crystalline phases were also found as minor components. In each alkali-metal series, the a- and c-lattice constants of M_2O-RE_2O_3-$2SiO_2$ bearing hexagonal apatite structure increased monotonically with an increase in the ionic radius of RE. The highest values of lattice constant, a and c, were observed for K_2O-RE_2O_3-$2SiO_2$. The hexagonal apatite structure samples, especially K_2O-RE_2O_3-$2SiO_2$ (RE=La,Nd,Sm,Gd,Dy), show relatively high conductivities and low activation energies. In the K_2O-RE_2O_3-$2SiO_2$, the activation energy was found to decrease from Dy to Sm and increase from Sm to La with increasing ionic radius of rare-earth. The lowest activation energy and the highest conductivity at 300 ℃ was observed for $K_2O\text{-}Sm_2O_3\text{-}2SiO_2$ (32.8kJ · mol^{-1}) and for $K_2O\text{-}Nd_2O_3\text{-}2SiO_2$ (1.31×10^{-2}S · cm^{-1}), respectively. This conductivity was compared to that of $K_2O \cdot 5.2Fe_2O_3 \cdot 0.8ZnO$.

In chapter 3, new solid electrolytes, $K_2O\text{-}RE_2O_3\text{-}nSiO_2$ (RE=La,Nd,Sm,Gd,Dy n=1-14) were prepared and their water-resistance examined. The major phase of all samples (excepting n=1) were hexagonal before and after water-treatment. The lattice constants, a and c, of the samples remained constantly before and after water-treatment. The halo of the XRD pattern due to the glass phase tends to grow with increasing SiO_2 content, while the intensities of the XRD peaks decrease. The amount of potassium eluted by water decreased with increasing SiO_2 content and was approximately constant in n≧6. On the other hand, the amount of potassium eluted decreased with decreasing ionic radius of rare-earth in the $K_2O\text{-}RE_2O_3\text{-}6SiO_2$ (RE=La,Nd,Sm,Gd,Dy) series. For the high SiO_2 containing samples of n>4, crystalline grains were not recognized. A dense glass ceramics composite, where crystal grains were surrounded by the glass phase, was found to form. The microstructure of the sample after water-treatment became smoother and the grain boundary of the samples of n>2 was difficult to recognize. The conductivity decreased with increasing SiO_2 content except for the sample n=1. The samples n=2 and 4 exhibited a dramatic decrease in conductivity and their activation energy increased after water-treatment. However, the electrical properties of the samples of n>4 were not influenced by water-treatment.

In chapter 4, new solid electrolytes, the rare-earth silicates, $RE_{10}Si_6O_{27}$ (RE=La,Nd,Sm,Gd,Dy,Y,Ho,Er,Yb) and $Nd_XSi_6O_{12+1.5X}$ (X=6-12)) were prepared, and their crystal structures, microstructures, electrical properties and ionic transport numbers were investigated. In the $RE_{10}Si_6O_{27}$ series, the major crystal phases of RE=La, Nd, Sm, Gd and Dy as well as $M_2O\text{-}RE_2O_3\text{-}2SiO_2$ (M=Li,K,Rb,Cs RE=La,Nd,Sm,Gd,Dy) were hexagonal, whereas those of RE=Y, Ho, Er and Yb were monoclinic. The hexagonal rare-earth silicates, $RE_{10}Si_6O_{27}$ (RE=La,Nd,Sm,Gd,Dy), prepared were found to be a mixture of an apatite phase ($RE_{9.33}\square_{0.67}(SiO_4)_6O_2$) as the major phase and some crystal phases (RE_2SiO_5 etc.) as a minor phase. In the

$Nd_xSi_6O_{12+1.5X}$ series, the major phases of the samples X=6, X=7-11 and X=11.12 were tetragonal, hexagonal and monoclinic, respectively. In the hexagonal apatite structure group, sites surrounded by six RE ions exist and it is supposed that oxide ions can migrate along the cavities of 2a-site in the c axial direction. The low activation energy and the high conductivity were estimated for the $RE_{10}Si_6O_{27}$ (RE=La,Nd,Sm,Gd,Dy). The activation energy decreased with increasing ionic radius of rare-earth. The lowest activation energy and the highest conductivity at 300℃ was 69.0kJ · mol^{-1} and 5.54x10^{-6}S · cm^{-1}, respectively. This conductivity value is comparable to that of $(ZrO_2)_{0.92}(Yb_2O_3)_{0.08}$. The electromotive force of the O_2 gas concentration cell comprising $Nd_{10}Si_6O_{27}$ was in agreement with the electromotive force calculated from the Nernst equation. The electron transfer number was close to 4 above 600℃, suggesting that the response is caused by the four electron reaction of O_2 at the electrodes.

In chapter 5, a potentiometric CO_2 gas sensor was prepared using K_2O-Sm_2O_3-$6SiO_2$, Li_2O-RE_2O_3-$2SiO_2$ (RE=La,Nd,Sm) or Li_2O-Sm_2O_3-$2SiO_2$+$(ZrO_2)_{0.92}(Yb_2O_3)_{0.08}$ (the layer type ionic conductor) as the solid electrolyte and their response characteristics examined. When the potassium ionic conductor and the lithium ionic conductor were applied to the CO_2 concentration cells, the electromotive forces induced by the change of CO_2 concentration were found to obey the Nernst equation above 300℃ and 400℃, respectively. The 90% response time of electromotive force for the fluctuation of the CO_2 concentration was relatively rapid (about 4 minutes) and the reproducibility was good. At the detection electrode, four electron transfer and two electron transfer were found to occur for O_2 and CO_2, respectively. In the layer type ionic conductor, the four electron transfer reaction associated with O_2 molecules were found to occur detection and counter electrode, indicating that this ionic conductor has excellent selectivity for O_2.

References

1) L.W.Strock, Z.Phys.Chem., B25, 441(1934).

2) D.O.Raleigh, J.Appl.Phus., 41, 1876(1970).

3) B.Reuter and K.Hardel, Z.Anorg.Allegem.Chem., 340, 168(1965).

4) G.W.Mellor and D.V.Louzos, J.Electrochem.Soc., 118, 846(1971).

5) G.W.Mellor, D.V.Louzos and J.A.van Lier, J.Electrochem.Soc., 118, 846(1971).

6) J.Kuwano and M.Kato, Denki Kagaku, 46, 353(1978).

7) M.S.Whittinghan and R.A.Huggins, J.Electrochem.Soc., 118, 1(1971).

8) S.Geller, J.R.Akridge and S.A.Wilber, Phys.Rev., 1319, 5396(1979).

9) C.C.Liang, J.Electrochem.Soc., 120, 1289(1973).

10) U.V.Alpen, J.Solid State Chem., 29, 379(1979).

11) H.Schuz and K.H.Tiemann, Aata Cryst., A35, 309(1979).

12) R.Mercier, J-P.Malugani, B.Fahys and G.Robert, Solid State Ionics, 5, 663(1989).

13) H.Wada, M.Menetrier, A.Levasseur and P.Hagenmuller, Mater.Res.Bull., 18, 469(1983).

14) R.Kanno, Y.Takeda, K.Takeda and O.Yamamoto, J.Electrochem.Soc., 131, 469(1984).

15) H.Y-P.Hong., Mater.Res.Bull., 13, 117(1978).

16) K-W.Hu, I.D.Raistrick and R.A.Huggins, J.Electrochem.Soc., 124, 1240(1977).

17) H.Aono, E.Sugimoto, Y.Sadaoka, N.Imanaka and G.Adachi, J.Electrochem.Soc., 137, 1023(1990).

18) H.Aono, E.Sugimoto, Y.Sadaoka, N.Imanaka and G.Adachi, Solid State Ionics, 47, 257(1991).

19) M.Itoh, Y.Inaguma, W.H.Jung, L.Chen and T.Nakamura, Solid State Ionics, 70/71, 203(1994).

20) C.A.Beevers and M.A.Ross, Z.Kristallogr., 97, 29(1937).

21) R.Collongues, J.Thery and J.P.Boilot, "Solid Electrolytes
(ed. P.Hagenmuller)", p.253, Academic Press(1978).

22) A.Imai and M.Harata, Jpn.J.Appl.Phy., 11, 180(1972).

23) J.B.Goodenough, H.Y-P.Hong and J.A.Kofalas, Mater.Res.Bull.,
11, 203(1976).

24) S.Yde-Andersen, J.S.Lundsgaad, L.M ϕ ller and J.Engell,
Solid State Ionics, 14, 73(1984).

25) E.M.Vogel, R.J.Cava and E.Retman, Solid State Ionics, 14, 1(1984).

26) R.D.Shannon, B.E.Taylor, T.E.Gier, H-Y.Chen and T.Berzins,
Inorg. Chem., 17, 958(1978).

27) T.Takahashi and K.Kuwahara, Nihon Kagaku kai-shi, 1974, 1883.

28) G.D.Dudley and B.H.C.Steele, J.Solid State Chem., 21, 1(1977).

29) T.Takahashi, K.Kuwahara and Y.Kase, Nihon Kagaku Kai-shi, 1975, 1305.

30) H.Y-P.Hong, "Solid State Chemistry of Energy Conversion and Storage
(ed. J.B.Goodenough)", p.179, Am.Chem.Soc.(1977).

31) C.Delmas, C.Fouassier, J.M.Reau and P.Hagenmuller, Mater.Res.Bull.,
11, 1981(1976).

32) M.S.Whittingham and R.A.Huggins, "National Bureau of Standard(NAS)
Spec.Publ.", 364, 139(1972).

33) O.Nakamura, T.Kodama, I.Ogino and Y.Miyake, Chem.Lett., 1979, 17.

34) A.T.Howe and M.G.Shilton, J.Solid Chem., 28, 345(1979).

35) G.C.Farrington and J.L.Briant, Science, 204, 1371(1979).

36) H.Iwahara, T.Esaka, H.Uchida and N.Maeda, Solid State Ionics,
3/4, 359(1981).

37) H.Iwahara, H.Uchida and S.Tanaka, Solid State Ionics, 9, 1021(1983).

38) H.Iwahara, T.Esaka, H.Uchida and T.Yamauchi, Solid State Ionics,
18, 1003(1986).

39) T.Yajima, I.Iwahara, N.Fukatsu, T.Ohashi and K.Koide, Keikinzoku,
42, 263(1992).

40) S.Kuwata, N.Miura, N.Yamazoe and T.Seiyama, Chem.Lett., 1984. 1295.

41) N.Yamazoe, J.Hisamoto, N.Miura and S.Kuwata, Sensors and Actuators. 12, 415(1987).

42) A.V.Joshi and C.C.Liang, J.Electrochem.Soc., 124. 1253(1977).

43) J.M.Reau, C.Lucat, G.Campet, J.Claverie and J.Portier, Electrochim. Acta, 22, 761(1977).

44) S.Vilminot, G.Perez, W.Granier and L.Cot, Solid State Ionics, 2, 87(1981).

45) Y.Niizeki, O.Takagi and S.Toshima, Denki Kagaku, 54, 961(1986).

46) C.Wagner, Naturwiss., 31, 365(1943).

47) D.W.Stickler and W.G.Carlson, J.Am.Ceram.Soc., 47, 122(1964).

48) K.Takami, New Ceramics, 1992(1), 69.

49) K.Nagata and K.Goto, Shinkinzoku-kougyou, 1980, 107.

50) T.Kudo and H.Obayashi, J.Electrochem.Soc., 122, 142(1972).

51) B.C.H.Steele and C.B.Alcock, Trans.Metall.Soc. AIME, 233, 1359(1965).

52) T.Takahashi and H.Iwahara, Mater.Res.Bull., 13. 1447(1978).

53) F.Vanbaelinghem, A.Pelloux and C.Deportes, J.Appl.Electrochem., 6, 67(1976).

54) T.V.Dijk, K.J.D.Vries and A.J.Burggraaf, Phys.Stat.Sol., 58, 115(1980).

55) T.Ishihara, H.Matsuda and Y.Takita, J.Am.Chem.Soc., 116, 3801(1994).

56) R.L.Cook, J.J.Osborn, J.H.White, R.C.Macduff and A.F.Sammells, J.Electrochem.Soc., 139, 19(1992).

57) M.Gauther and A.Chamberland, J.Electrochem.Soc., 124, 1579(1977).

58) Y.Sadaoka, Y.Sakai and T.Manabe, J.Mater.Chem., 2, 945(1992).

59) Y.Sadaoka, M.Matsuguchi, Y.Sakai and T.Manabe, J.Mater.Sci., 28, 2035(1993).

60) Y.Sadaoka, Y.Sakai, M.Matsumoto and T.Manabe, J.Mater.Sci., 28, 5783(1993).

61) S.Yao, Y.Shimizu, N.Miura and N.Yamazoe, Chem.Lett., 1990, 2033.

62) N.Imanaka, T.Kawasato and G.Adachi, Chem.Lett., **1991**, 13.

63) N.Imanaka, T.Kawasato and G.Adachi, Chem.Lett., **1990**, 497.

64) S.Ikeda, S.Kato, K.Nomura, K.Ito, H.Einaga, S.Saito and Y.Fujita, Solid State Ionics, **70/71**, 569(1994).

65) N.Miura, S.Yao, M.Sato, Y.Shimizu, S.Kuwata and N.Yamazoe, Chem.Lett., **1993**, 1973.

66) T.Maruyama, S.Sasaki and Y.Saito, Solid State Ionics, **23**, 107(1987)

67) N.Imanaka, T.Murata and G.Adachi, Denki Kagaku, **61**, 909(1993).

68) S.Nakayama and Y.Sadaoka, J.Mater.Chem., **4**, 663(1994).

69) H.Supriyatno, A.Dubbe, M.Matsuguchi, Y.Sadaoka, Y.Sakai and S.Nakayama, Denki Kagaku, **63**, 325(1995).

70) P.Quintana and A.R.West, Solid State Ionics, **23**, 179(1987).

71) G.Roth and H.Bohn, Solid State Ionics, **18/19**, 553(1986).

72) K.Jackowaka and A.R.West, J.Mater.Sci., **18**, 2380(1983).

73) J.Liu and W.Weppner, Eur.J.Solid State Inorg.Chem., **28**, 1151(1991).

74) N.Miura, S.Yao, Y.Shimizu and N.Yamazoe, Sensors and Actuators B, **9**, 165(1992).

75) E.Banks and C.H.Kim, J.Electrochem Soc., **132**, 2617(1985).

76) C.H.Kim, B.Qui and E.Banks, J.Electrochem Soc., **132**, 1340(1985).

77) M.G.Alexander, Solid State Ionics, **22**, 257(1987).

78) U.V.Alpen, E.Schonherr, H.Schulz and G.H.Talat, Electrochimica Acta, **22**, 805(1977).

79) U.V.Alpen, H.Schulz, G.H.Talat and H.Bohn, Solid State Commun, **23**, 911(1977).

80) W.Nagel and H.Bohn, Solid State Commun, **42**, 625(1982).

81) H.Perthuis and Ph.Colomban, J.Mater.Sci.Lett., **4**, 344(1985).

82) S.Nakayama, H.Kuroshima, Y.Sadaoka and Y.Sakai, J.Ceram.Soc.Jpn., **100**, 968(1992).

83) M.G.Alexander and B.Riley, Solid State Ionics, **18/19**, 478(1986).

84) O.Nakamura, Y.Saito, T.Asai, K.Ado, H.Kageyama, I.Ogino and
Y.Moriya, "Government Industrial Research Institute", 380, 9(1990).

85) K.Jackowska and A.R.West, J.Mater.Sci., **18**, 2380(1983).

86) D.P.Almond and A.R.West, Solid State Ionics, **23**, 27(1987).

87) J.Felsche, J.Solid State Chem., **5**, 266(1972).

88) M.Sato, Y.Kono and K..Uematsu, Chem.Lett., **1994**, 1425

89) M.Sato, Y.kono, H.Ueda, K.Uematsu and K.Toda, Solid State Ionics,
83, 249(1996).

90) J.E.Bauerle and J.Hrize, J.Phys.Chem.Solids, 30, 565(1969).

91) O.L.Anderson and D.A.Stuart, J.Am.Ceram.Soc., **37**, 573(1954).

92) R.M.Hakim and D.R.Uhlmann, Phys.Chem.Glass, 12, 1326(1971).

93) T.Ogata, S.Fujitsu, M.Miyayama, K.Koumoto and H.Yanagida,
J.Mater.Sci.Lett., 5. 285(1986).

94) T.Maruyama, X.-Y.Ye and Y.Saito, Solid State Ionics, **23**, 113(1987).

95) N.Miura, S.Yao, Y.Shimizu and N.Yamazoe, J.Electrochem.Soc.,
139, 1384(1992).

96) J.Liu and W.Weppner, Appl.Phys., **A55**, 250(1992).

97) N.Imanaka, T.Murata, T.Kawasato and G.Adachi, Chem.Lett., **1992**, 103.

98) W.J.Moore, "Physical Chemistry 3rd Edition", p632,
Tokyo Kagaku Doujin(1979).

Acknowledgment

The author is gratefully to Professor Dr. Mineo Sato, of Niigata University, who provided valuable guidance and warm encouragement in preparing the manuscript, and is also indebted to Professor Dr. Bunichi Kanamaru, Professor Dr. Yoshio Masuda, Professor Dr. Hiroshi Imaizumi and Associate Professor Dr. Masatoshi Ohta, of Niigata University, for their valuable comments and kind suggestions. Many helpful discussion and encouragement by Professor Dr. Yoshihiko Sadaoka, of Ehime University, and Associate Professor Dr. Shigeki Kuwata, of Niihama National College of Technology, during this work are gratefully acknowledged. Technical supports of Mr. Masahiro Okazaki, Mr. Takashi Hino, Mr. Teruhiko Takada and Mr. Terumitsu Ichimori, of Shinagawa Refractories Co., Ltd., and Mr. Nobuo Hayashi and Mr. Yasuo Mizota, of Okayama Ceramics Center, are deeply appreciated. Thanks are due to ex-Managing Director Takanosuke Yajima, Managing Director Dr. Kenki Ishizawa, Mr. Saburo Togawa, Mr. Tadao Mino and Mr. Hiroyuki Shikama, of Shinagawa Refractories Co., Ltd., for their hearty encouragement. Finally, the author would like to express sincere gratitude to Professor Dr. Masatomi Sakamoto, of Yamagata University, for his continuous guidance and encouragement from the undergraduate student age.

The present paper has been written as a doctoral thesis presented at Niigata University.

March 1997

Susumu Nakayama